

Lukas Hofstädter BSc

Study on State of Health Estimation Methods for Lithium-ion Cells

MASTER'S THESIS

to achieve the university degree of
Diplom-Ingenieur

Master's degree programme:
Technical Physics

submitted to

Graz University of Technology

Supervisor

Univ.-Prof Dipl.-Phys. Dr.rer.nat. Wolfgang von der Linden

Institut für Theoretische Physik – Computational Physics

In cooperation with
Virtual Vehicle Research GmbH

Graz, October 2020

AFFIDAVIT

I declare that I have authored this thesis independently, that I have not used other than the declared sources/resources, and that I have explicitly indicated all material which has been quoted either literally or by content from the sources used. The text document uploaded to TUGRAZonline is identical to the present master's thesis.

Date, Signature

Abstract

Today Lithium-ion battery technology represents one of the most promising technologies for electric energy storage and has become increasingly important in the automotive sector. Therefore, the monitoring of battery State of Health is essential for the safe and efficient operation of electric and hybrid electric vehicles. A quantity, which particularly reliably describes a cell's State of Health is its total capacity. However, cell capacity cannot be directly measured and therefore has to be properly estimated.

This work deals with the investigation of different methods for State of Health estimation of Lithium-ion cells for the on-board use. After a brief introduction to Lithium-ion cells and their ageing mechanisms, two methods based on the analysis of charging characteristics are applied to measurement data gathered from extensive ageing tests taken on Panasonic NCR18650B cells. In this comparative study *Incremental Capacity Analysis* and *Analysis of the Constant Voltage charging process* are used to describe the degradation in State of Health for a variety of ageing conditions. Subsequently, *Approximate Weighted Total Least Squares*, an optimization method for on-board capacity estimation, is examined in combination with different methods for State of Charge estimation. To validate the technique's applicability regarding on-board use, it is applied to measurement data gathered from drive cycle ageing tests.

For the majority of ageing conditions within our testing, *Incremental Capacity Analysis* is able to describe the cells State of Health within a maximum absolute 2-sigma error of less than $\pm 3.7\%$. However, for radical ageing the maximum absolute error is about $\pm 6\%$. *Analysis of the Constant Voltage charging process* shows an overall weaker performance with a maximum absolute error up to $\pm 9.0\%$.

According to the obtained results, *Approximate Weighted Total Least Squares*, especially in combination with Extended Kalman Filter for State of Charge estimation, is able to estimate total cell capacity within three-sigma error bounds of $\pm 1.6\%$ and is able to track the cell's capacity fade.

The performance of both, *Incremental Capacity Analysis* and *Analysis of the Constant Voltage charging process*, is highly dependent on the cells operation conditions. Therefore, they are only applicable for scenarios where the operation conditions are well known beforehand and repetitive over the cell's whole lifespan. From this perspective they are not suitable for on-board use in vehicles. *Approximate Weighted Total Least Squares* seems to be a suitable candidate for on-board State of Health

0 Abstract

estimation validated by high accuracy and a recursive computation manner, which makes it lean in computational requirements. Future research could deal with the hardware implementation of this method.

Keywords: Lithium-Ion, State of Health estimation, Capacity estimation, Incremental Capacity Analysis, Constant Voltage, Weighted Total Least Squares

Kurzfassung

Die Lithium-Ionen Batterietechnologie zählt heute zu den vielversprechendsten Technologien zur Speicherung elektrischer Energie und hat seit geraumer Zeit im Automobilsektor enorm an Wichtigkeit gewonnen. Die Überwachung des State of Health der verwendeten Zellen stellt dabei eine wichtige Rolle für den sicheren und zuverlässigen Betrieb von Batterie-Systemen in elektrischen und hybrid-elektrischen Fahrzeugen dar. Die Gesamtkapazität einer Lithium-Ionen Zelle gilt als zuverlässiger Indikator zur Beschreibung des State of Health. Leider kann diese Größe nicht direkt gemessen werden, weshalb eine adäquate Methode zur Abschätzung der Gesamtkapazität benötigt wird.

In dieser Arbeit geht es um die Untersuchung unterschiedlicher Methoden zur Abschätzung des State of Health von Lithium-Ionen Zellen. Nach einer kurzen Einführung zu Lithium-Ionen Zellen und deren Alterungsmechanismen werden zunächst zwei Methoden, welche die Charakteristika des Ladevorganges analysieren, untersucht. Die zugehörigen Messdaten stammen von Alterungsversuchen an kommerziell erhältlichen Panasonic NCR18650B Zellen. In dieser vergleichenden Untersuchung werden die Methoden *Incremental Capacity Analysis* und *Analysis of the Constant Voltage charging process* verwendet, um den durch Alterung hervorgerufenen Verfall des State of Health für unterschiedliche Betriebsbedingungen während jener zu beschreiben. Anschließend wird *Approximate Weighted Total Least Squares*, ein Optimierungsalgorithmus, als Methode zur on-board Kapazitätsabschätzung untersucht. Dabei wird dieser mit zwei unterschiedlichen Verfahren zur Abschätzung des Ladezustandes kombiniert. Um die Eignung dieser Methode für reale Anwendungen zu überprüfen wird sie an Messdaten angewandt, welche von einem realitätsnahen Alterungstest durch Fahrzyklen stammen. Die Resultate zeigen, dass *Incremental Capacity Analysis* für den Großteil der während unserer Alterungstests auftretenden Betriebsbedingungen in der Lage ist den State of Charge mit einer 2-sigma Unsicherheit von $\pm 3.7\%$ anzugeben. Für sehr starke Alterung durch beispielsweise hohe Temperatur weist die Methode eine Unsicherheit von $\pm 6\%$ auf. *Analysis of the Constant Voltage charging process* zeichnet sich durch eine allgemein etwas schwächere Performance aus. So sind mit dieser Methode für die gewählten Datensätze Abschätzungen des State of Health mit einer maximalen Unsicherheit von $\pm 9.0\%$ möglich.

Die erhaltenen Ergebnisse zeigen, dass *Approximate Weighted Total Least Squares* in

0 Kurzfassung

Kombination mit dem Extended Kalman Filter eine Abschätzung der Gesamtkapazität mit einer 3-sigma Unsicherheit von $\pm 1.5\%$ erreicht und dem Verlauf der Kapazität während der Alterung folgt.

Die Güte der von *Incremental Capacity Analysis* und *Analysis of the Constant Voltage charging process* erhaltenen Ergebnisse ist stark abhängig von den Betriebsbedingungen während der Alterung der Zellen. Aufgrund dessen sind diese Methoden nur dann geeignet, wenn genaue Kenntnis über die Betriebsbedingungen im vorherein besteht und diese konstant über den Lebenszeitraum der Zelle auftreten. Folglich erscheinen diese zur on-board Überwachung des State of Health als ungeeignet. Im Gegensatz dazu erscheint der *Approximate Weighted Total Least Squares* Algorithmus dafür geeignet. Er liefert Ergebnisse mit hoher Genauigkeit und berechnet den Schätzer für den State of Health auf rekursive Weise, wodurch Rechenaufwand und Speicheranforderungen minimiert werden. Zukünftige Forschungsarbeit ergibt sich durch die mögliche Implementation auf Hardware und Testung des Algorithmus an realen Zellen in Echtzeit.

Schlagwörter: Lithium-Ionen, State of Health, Kapazitätsabschätzung, Incremental Capacity Analysis, Constant Voltage, Weighted Total Least Squares

Acknowledgement



This thesis was written at Virtual Vehicle Research GmbH in Graz, Austria. The author would like to acknowledge the financial support within the COMET K2 Competence Centers for Excellent Technologies from the Austrian Federal Ministry for Climate Action (BMK), the Austrian Federal Ministry for Digital and Economic Affairs (BMDW), the Province of Styria (Dept. 12) and the Styrian Business Promotion Agency (SFG). The Austrian Research Promotion Agency (FFG) has been authorised for the programme management. They would furthermore like to express their thanks to their supporting industrial partners as well as their scientific project partner, namely the Graz University of Technology.



I would like to thank my supervisor Univ.-Prof. Dipl.-Phys. Dr.rer.nat. Wolfgang von der Linden and my mentor Dipl.-Ing. Dino Hrvanovic for supporting me during the whole process of creation.

Graz, November 2, 2020

Lukas Hofstädter

Contents

Statutory Declaration	i
Abstract	iii
Kurzfassung	v
Acknowledgement	vii
1 Introduction	1
1.1 Related Nomenclature and Quantities	2
1.2 Problem Statement and Motivation	4
2 Fundamentals	7
2.1 The Electrochemical Cell	7
2.1.1 The Lithium-Ion Cell	7
2.2 Battery Ageing	9
2.2.1 Ageing Effects on the Negative Electrode	10
2.2.2 Ageing Effects on the Positive Electrode	13
2.2.3 Ageing Effects on Inactive Cell Components	13
2.3 Li-ion Battery State Estimation	15
2.3.1 State of Health (SoH) Estimation	15
2.3.2 State of Charge (SoC) Estimation	17
3 Ageing Data Analysis	21
3.1 Measurement Data	21
3.1.1 Reference-Test-Protocol (RTP)	22
3.1.2 Load-Profile (LP)	24
3.2 Incremental Capacity Analysis of the Constant-Current Charging Phase	26
3.2.1 Data Organization and Selection of Loading curves	26
3.2.2 Calculation of IC-Curves	27
3.2.3 Gaussian Smoothing	29
3.2.4 Localization of Feature Points	31
3.2.5 Linear Regression of SoH versus FP-location	31
3.3 ICA: Implementation and Results	33
3.3.1 Drive Cycle Ageing	33
3.3.2 Calendric Ageing	34
3.3.3 Cycle Ageing	41
3.4 Analysis of the Constant-Voltage Charging Phase	45
3.4.1 Data Extraction	46

Contents

3.4.2	Characterisation via Exponential Decay Function	47
3.4.3	Linear Regression of SoH versus Decay Constant	47
3.5	CV-Analysis: Implementation and Results	48
3.5.1	Drive Cycle Ageing	49
3.5.2	Calendric Ageing	50
3.5.3	Cycle Ageing	56
3.6	Discussion on Ageing Data Analysis	61
4	Total Capacity Estimation via Approximate Total Least Squares	65
4.1	From Weighted Least Squares to Weighted Total Least Squares	68
4.1.1	Weighted Least Squares	68
4.1.2	Derivation of Weighted Total Least Squares	71
4.2	Confidence Intervals	72
4.3	Goodness of Model Fit	73
4.4	Derivation of Recursive Approximate Weighted Total Least Squares . .	74
4.5	Algorithm Testing and Results	78
4.5.1	Input Data Generation	78
4.5.2	Results and Discussion	80
5	Conclusion	89
	List of Abbreviations	93
	List of Figures	95
	References	101

1

Introduction

Due to global population growth and rapidly improving technology our planet is facing big environmental challenges. With the permanently growing demand of available electrical energy, innovative solutions for providing and storing said energy are needed. Therefore, electrochemical Energy Storage Systems (ESSs) will become increasingly important in the future, whether for mobile energy supply of more sophisticated and smaller mobile phones or computers, power tools and electric cars, or even in a larger dimension for the stationary storage of renewable energies (Korthauer, 2013).

There exists a wide variety in electrochemical ESSs. Nevertheless, the prominence of lithium-ion Batteries (LIBs) as ESS has grown permanently since the first commercialization in 1990 by Sony Corp (Yoshio et al., 2009). Today, lithium-ion (Li-ion) technology is the most auspicious battery technology. This can be led back to LIBs superior technical properties like high volumetric and gravimetric energy storage capability, high efficiency and good cycle life (Berecibar et al., 2016; Agubra & Fergus, 2013). Figure 1.1 by Beggi et al. (2018) shows the high volumetric and gravimetric energy storage capability of Li-ion cells compared to other electrochemical ESSs.

Initially, Li-ion technology was used in portable/consumer electronic devices like notebooks or cellphones, where it achieved great success. During the last decade the technology has spread to the automotive market where LIBs are used as ESS in hybrid electric vehicles (HEVs) and electric vehicles (EVs) (Li et al., 2018). In order to avert the endangerment of nature through global warming, the reduction of greenhouse gas (GHG) emission will further push the market for the use of LIBs in vehicles. Despite the advantages of Li-ion technology, the safe application of LIBs also implies several difficulties. If a LIB is operated under wrong conditions it has the ability to self-destruct. For example too high currents or overcharging of the battery

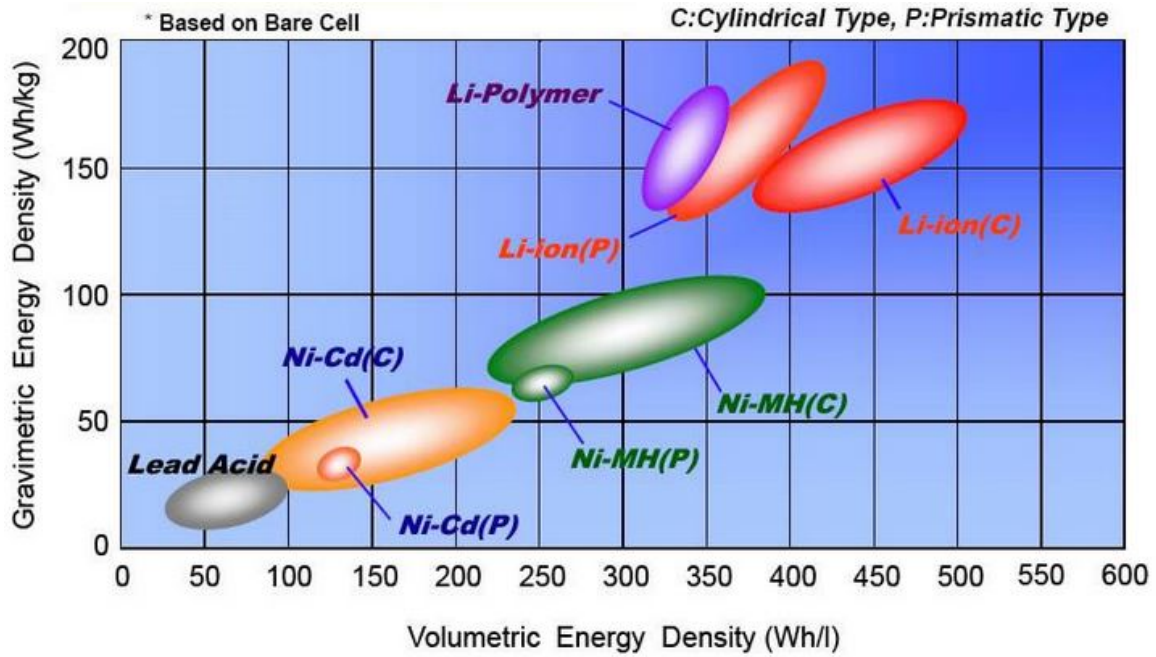


Figure 1.1: volumetric energy density (Wh/l) and gravimetric energy density(Wh/kg) for the major small-sealed recharge- able battery technologies (Beggi et al., 2018)

can result in a thermal runaway, which refers to an uncontrolled exothermic feedback reaction. Thus, the protection of user and battery-powered system is one of the main topics in applying this technology. In order to guarantee the optimal and safe use of a battery, a monitoring and controlling Battery Management System (BMS) is needed. Tasks of the BMS are the execution of real-time measurements of physical quantities like current, voltage and temperature to evaluate the actual operating conditions and respond to them in the most suitable way. In order to do so it is crucial to have precise information regarding the present ageing status of the individual cells. This challenge will lead us to the objectives of this work.

1.1 Related Nomenclature and Quantities

In this section a general overview of the nomenclature related to battery cells is given. Herein, important terms and quantities are described which will be used subsequently in this work. To recall abbreviations used within this thesis easily, they are listed at the end of this work.

Cell: In reference to battery technology a cell is the smallest electrochemical unit consisting of negative and positive electrodes, electrolyte and a separator. In this work only secondary cells are considered. In contrast to primary cells, these are rechargeable.

Battery: relates to an electrically connected group of two or more cells.

Terminal voltage: refers to the electric potential difference measured between the cell terminals. The terminal voltage varies with the operating conditions of the cell. Its unit is Volt (V).

Open-Circuit-Voltage (OCV): is the difference in electric potential between the terminals of a cell when the battery is fully rested, i.e. the battery has been subjected to an open circuit for a substantial period of time. The Open-Circuit-Voltage (OCV) generally depends on the cell's State of Charge (SoC) and temperature. The unit of the OCV is Volt (V).

Internal Resistance: refers to an overall resistance within a battery cell and in general depends on the cell's operating conditions. Internal resistance also varies with the cell's SoC. With increasing internal resistance, the cell's efficiency decreases and thermal stability is reduced because more of the charging energy is converted into heat. The internal resistance is given in Ohm (Ω).

Capacity Q : In this work the capacity Q describes an amount of charge and has the unit ampere hours(Ah). It must not be confused with the electric capacitance which describes a capacitor's ability to hold charge.

C-rate: refers to the rate of charge- or discharge-current in normalized form. Therefore, a C-rate of 0.5 C would relate to a current draw at which a completely charged cell would be entirely discharged within 2 hours. The C-rate's unit is h^{-1} .

State of Charge (SoC): The SoC is a quantity to describe a cell's present quantity of charge it is able to deliver to or receive from a load circuit. It is the ratio of present remaining capacity to the cell's present total capacity. SoC can be seen as the electric equivalent to a value given by a fuel gauge for combustion engines.

Total Capacity Q_{tot} : means the quantity of charge a cell is able to deliver to or receive from a load circuit as it is brought from a fully charged state to a fully discharged state or vice versa. In this work the unit chosen for the charge capacity is ampere hours (Ah). The total capacity of a cell is not constant but depends on the type and amount of active materials, on the ambient temperature and many more parameters.

Nominal Capacity Q_{nom} : refers to a representative value of an unaged cell's total capacity. This value is specified by the cell manufacturer and depends on the charging/discharging conditions chosen by the manufacturer. The nominal capacity of the investigated cells was determined at $T = 25^\circ\text{C}$ at a current rate of 0.5 C.

1 Introduction

End of Life (EoL): refers to the moment when a cell does not meet the prescribed performance requirements anymore. Within the context of automotive application a cell's EoL is usually described as the moment at which the total capacity has degraded by 20 % or internal resistance has doubled.

State of Health (SoH): The SoH is a quantity to describe the ageing status of a cell. It gives information about how long the battery will last before it reaches its EoL. Cells usually slowly degrade both in terms of capacity and power. Therefore, the two most common definitions of SoH are described either by capacity fade or rise in internal resistance which is directly related to power fade.

1.2 Problem Statement and Motivation

In general, battery technology will play a major role in the transportation sector in the upcoming future. As a result sustained research on the subject of rechargeable batteries occurred in the last decades.

With the introduction of Li-ion battery systems for automotive applications, there arose various demanding requirements. After all, vehicles should be safe, comfortable, sustainable and reliable. Thus, the whole vehicle including engine, control units for accelerating, braking, steering and more has to be reliably supplied with electricity (Berecibar et al., 2016). In order to assign these claims a battery management system BMS is needed. The BMS is an electronic monitoring and controlling system, which manages the operational mode of the battery system to guarantee safe operation and to ensure a prolonging of lifetime. Protection of cells from overcharge and overdischarge, thermal management, detection of possible failures and analysing the available energy and power of the battery pack are the key functionalities of a BMS (Berecibar et al., 2016; Pistoia & Liaw, 2018). As one part of the diagnostics a BMS needs to perform accurate SoH estimations.

The aim of this thesis is the investigation of SoH estimation methods for the on-board use in the BMS of EVs and HEVs. After a brief introduction to electrochemical cells and their ageing behaviour, several methods which aim to describe the SoH of a battery cell will be treated. The methods of interest in specific are *Approximate Weighted Total Least Squares* as well as *Incremental Capacity Analysis* and *Analysis of the Constant Voltage charging process*. For the purpose of this exploration extensive ageing measurements were taken at the Virtual Vehicle Research GmbH together with industrial partners. Over a timespan of two years specific load tests were performed to multiple Panasonic NCR18650B Li-ion cells to simulate the natural ageing process

1.2 Problem Statement and Motivation

under different conditions. Based on this large pool of measurement data, a meaningful evaluation of the above-mentioned methods regarding hardware-related use should be achieved.

2

Fundamentals

2.1 The Electrochemical Cell

A cell refers to the smallest electrochemical energy storage unit. It usually consists of several fundamental components comprising a negative electrode, a positive electrode, an electrolyte and a separator. For the purpose of easier explanation we consider a cell in discharge operation mode. During discharge electrons are expelled from the negative electrode material and delivered to the load circuit. This process is known as *oxidation* of the negative electrode. Common negative electrode materials are pure metals or alloys. The positive electrode material accepts electrons from the load circuit. This process is known as *reduction*. The electrolyte functions as an ionic conductor. During discharge positive ions move from the negative electrode through the electrolyte to the positive electrode. The separator physically isolates the positive electrode from the negative electrode to prevent internal short circuiting. Nevertheless, it is an ionic conductor and does not hinder the ionic transport (Plett, 2015a).

2.1.1 The Lithium-Ion Cell

Conventional electrochemical cells like Lead-Acid or Nickel-Cadmium cells work differently from Li-ion cells. In these the electrolyte chemically reacts with the electrode materials via *redox reactions*. In the case of Li-ion cells, lithium does not react chemically with the electrode materials. Instead it enters or departs the crystal structure of the electrode materials. This procedure is termed as *intercalation* and *deintercalation* respectively. Cells with this operation principle are called *insertion cells*. To clarify the working principle of those cells Figure 2.1 displays the basic structure of a Li-ion cell. During discharge, lithium atoms inside the negative electrode dispense their weakly

2 Fundamentals

bound valence electrons and become positive charged Li^+ ions. Next, the Li^+ ions de-intercalate from the electrode material and move towards the positive electrode. At the surface of the positive electrode they recombine with the surplus electrons to afterwards intercalate as neutral Li-ions into the positive electrode. The described insertion process is highly reversible and very gentle in contrast to a chemical reaction between the electrolyte and the electrode material. Therefore, an advantage of Li-ion cells is a high cycle life. Due to the back and forth movement of the ions, Li-ion cells are often called *rocking chair*, *swing* or *shuttlecock cells* (Plett, 2015a).

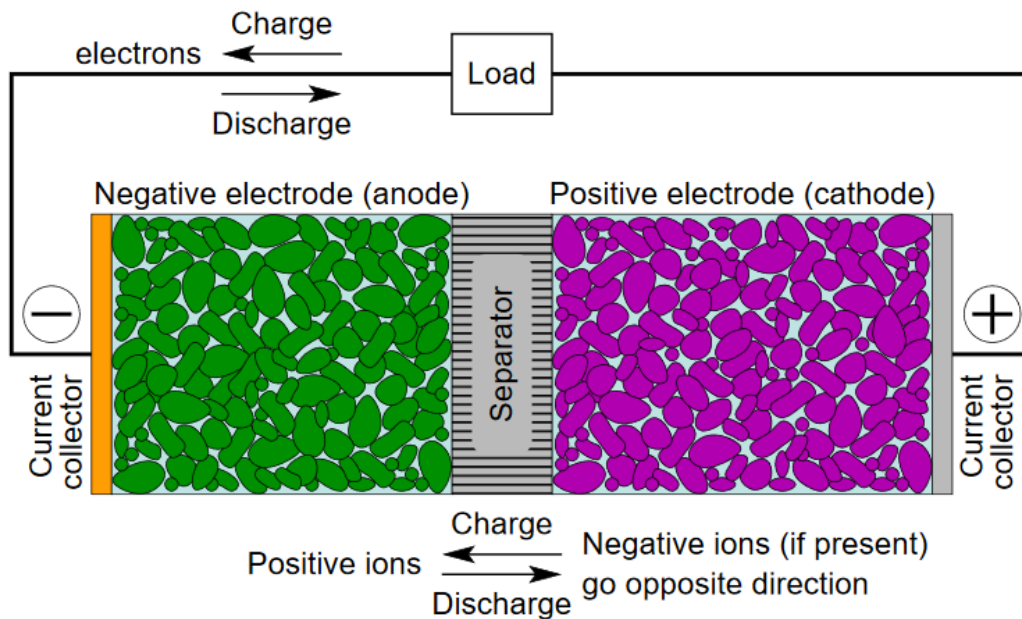


Figure 2.1: Basic working principle of a electrochemical cell (Plett, 2015a)

For a gentle intercalation process, the electrode materials must show suitable properties. They should have *open* crystal structures with many vacancies, which allow the lithium to move easily. At the same time the electrodes must be able to conduct the electrons from the load circuit. During operation the crystal structure of the electrodes is not altered chemically, but minor structural changes nonetheless may occur due to the intercalation and deintercalation process. The intercalation and deintercalation of lithium ions can lead to a volume change of up to 10 %. If the concentration of lithium ions in the structure of an electrode material gets too high, structural phase transitions could occur which may result in non-reversible damaging of the electrode material (Plett, 2015a).

The single cell description leads us to the term *module*, which describes an electrically connected set of an arbitrary number of cells and the corresponding structural parts as well as measurement- and other simple electric-devices. Within a module, the cells can

be connected in parallel or serial. The design of battery modules is mostly defined by legal voltage limits and ease of handling, as voltages above 60 V DC require special precautionary measures for further manipulation and processing (Fischer, 2013).

The combination of one or more battery modules, including additional sensors and control units, constitutes a *battery pack*. To guarantee safe and optimal operation of the battery pack a BMS accompanies it and thus makes it a full *battery system*. The BMS monitors and processes all information gathered from sensors at module or pack level to determine the cells terminal voltages, temperatures and currents at important points during operation. Furthermore, it handles the connection and disconnection of the battery system (Plett, 2015a).

2.2 Battery Ageing

Li-ion batteries were initially used in portable devices like cellphones, camcorders and notebooks. In these kinds of application lifetime of the batteries only played a minor role. With the increasing use of Li-ion technology on the market of EVs and HEVs the demands regarding lifetime has grown. According to literature battery packs are supposed to operate for about 10-15 years or a total number of 20-30 thousand cycles respectively (Barré et al., 2013). As a result there is great interest in understanding ageing phenomena of Li-ion cells.

From the time of initial charging, the cells in a *battery pack* undergo ageing and their performance will degrade. At some time they will reach a point, where they no longer fulfil the requirements of application. In the automotive industry the EoL is referred to as the time when the cell lost 20-30 % of its initial capacity. In applications where the power of the cell is more important, the EoL is often chosen as the time when the battery cell's impedance has doubled (Huang et al., 2017; Farmann et al., 2015).

For an adequately working battery system, it is very important to know the present ageing status of the individual cells. The identification and understanding of ageing and degradation phenomena is one of most challenging goals in battery technology. The ageing processes are very complex as they result from interaction of many factors regarding environment and operation mode. In this section the fundamentals of LIB ageing as well as primary electrochemical and structural ageing mechanisms are explained.

Battery ageing can be divided into two types regarding their origination:

Calendric ageing describes the degradation of battery performance during storage. This highly depends on the storage conditions. The main two variables, which define the intensity of calendric ageing are storage temperature and SoC-level during storage. With higher storage temperatures side reactions like corrosion and reductive electrolyte decomposition are more likely leading to enhanced capacity fade. At too low temperatures other ageing effects emerge. Moreover, a high SoC-level during storage also provokes side reactions and therefore enhances calendric ageing (Pistoia & Liaw, 2018).

Cycle ageing refers to the performance loss caused by charge or discharge processes. It is directly related to the operation conditions of the battery cell. Here, the main influencing variables are charge/discharge current rate, the range in SoC wherein the cell was cycled, average SoC and temperature. Cycle ageing is accelerated as any of these variables is elevated (Pistoia & Liaw, 2018).

2.2.1 Ageing Effects on the Negative Electrode

The predominantly used active material for negative electrodes in Li-ion cells is natural or synthetic graphite (Barré et al., 2013; Plett, 2015b). Graphite has a high cycle stability, high lithium storage capability and is nontoxic and inexpensive. Furthermore, it is characterised by its low electrochemical potential, which is favourable to achieve a maximum cell voltage¹.

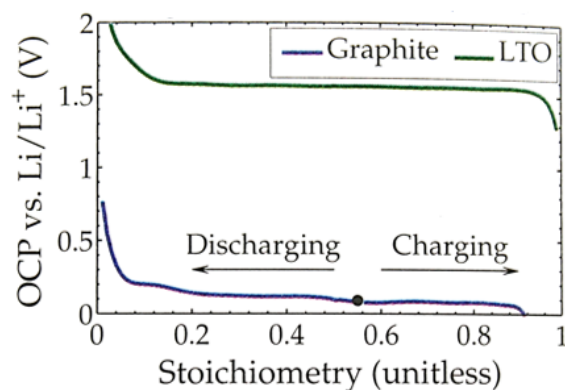


Figure 2.2: Open-Circuit-Potential of Graphite vs. another negative electrode material candidate (LTO) (Plett, 2015b)

On the one hand, the low electrochemical potential of graphite makes it very preferable for high-voltage Li-ion cells. On the other hand, it provokes the major degradation

¹The voltage of an electrochemical cell equals the positive-electrode potential minus the negative-electrode potential.

mechanism on the interface between the negative electrode and the electrolyte. The electric potential of the negative electrode is so low that the organic solvents used in the electrolyte are not stable anymore. In consequence reductive decomposition of the electrolyte occurs at the electrode-electrolyte interface. The formed reaction products form a layer on the electrode surface called Solid Electrolyte Interface (SEI) (Vetter et al., 2005). The formation of SEI occurs mainly in the onset of cycling, particularly during initial charge. Thus the first charge process is often called *formation process*. The created layer acts as a passivating coating between the electrode and the electrolyte which protects the electrolyte from further reduction and the electrode from further corrosion. Lithium is consumed during the SEI forming, which leads to a decreasing amount of lithium available for intercalation and deintercalation. Once the lithium is consumed by SEI formation it never returns in a usable form. This results in a non-reversible loss of cell capacity (Barré et al., 2013; Plett, 2015b). The loss of cycle-able lithium ions also depends on the specific surface area of the graphite particles. An increase in area increases the volume of reaction products and therefore enhances capacity fade (Agubra & Fergus, 2013).

A further consequence of SEI growth constitutes the rise of cell resistance. The built up layer is quasi permeable to Li-ions, but lessens the conductivity of ion transfer which leads to power fade of the cell.

As mentioned above SEI formation occurs predominantly during initial charge. Nevertheless, the growth of this layer continues even though less rapidly. While the SEI is protecting the electrolyte from reaching the electrode, some solvent is still able to transmigrate which leads to further SEI growth. This process may be augmented due to high cell temperatures. High temperatures can lead to SEI breakdown which causes additional exposed graphite sites (Vetter et al., 2005; Plett, 2015b).

Another ageing mechanism on negative electrodes is a process where, besides lithium, solvent molecules co-intercalate into the graphite electrode. As a result SEI formation takes place inside the electrode. As the SEI formation process is accompanied by gas generation this leads to increasing expansive pressure inside the electrode material. This may cause the graphite to break along internal grain boundaries or to exfoliate which exposes more electrode surface to the solvent making even more SEI formation possible. The cracking and splitting of active material can also be triggered by volume changes of the electrodes due to lithiation (Plett, 2015b).

Further ageing mechanisms in the negative electrode are triggered through the presence of hydrofluoric acid. It is produced via side-reactions between trace water in the electrolyte and ionized fluorine in the electrolyte salt. The acid attacks the SEI layer

2 Fundamentals

leading to dissolution. Furthermore, it also is able to dissolve particles of manganese or cobalt from the positive electrode. These electrical low conductive particles are able to transmigrate the separator and deposit in the SEI layer of the negative electrode which leads to higher cell resistance and hence to power fade. Besides that they are able to obstruct available graphite pores which lessens the availability of lithium to intercalate/deintercalate. This ageing mechanism is termed *anode poisoning* (Plett, 2015b).

To complete the catalogue of negative electrode ageing, a last mechanism is presented called *lithium plating*. It is referred to unwanted coating of the negative electrode with metallic lithium particles formed by the combining of Li-ions with electrons from the external circuit. This mainly appears when charging is forced at low temperatures or high current rates (Vetter et al., 2005; Barré et al., 2013). As this reaction consumes lithium and additionally covers the surface of the cell's negative electrode, lithium plating leads to capacity fade and power fade. A general view of the aforementioned ageing mechanisms in the negative electrode can be seen in Figure 2.3.

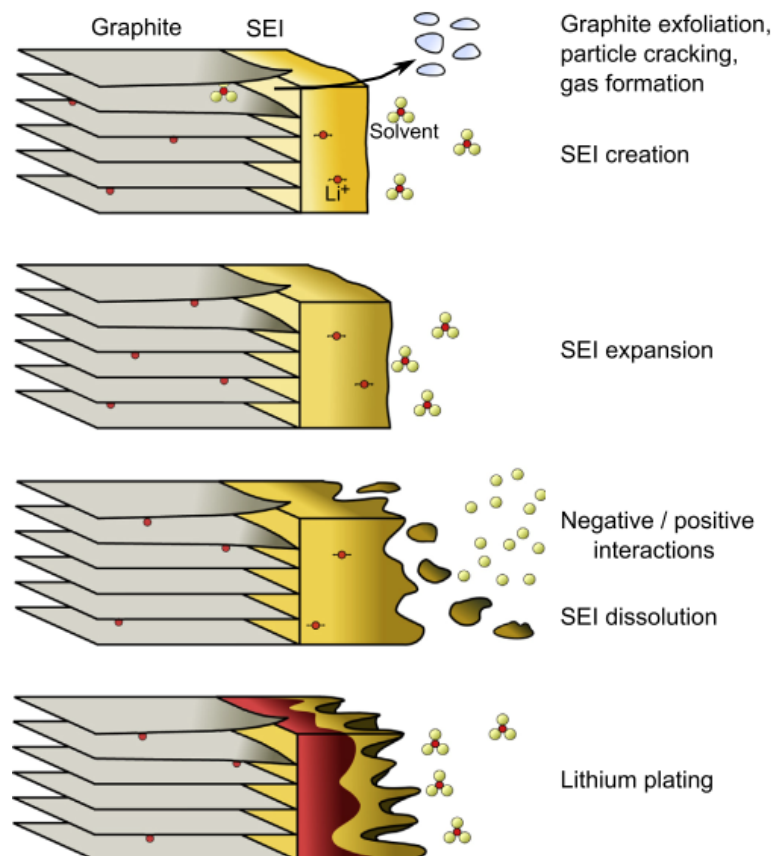


Figure 2.3: Overview of predominant ageing mechanisms in the negative electrode of Li-ion cells (Barré et al., 2013)

2.2.2 Ageing Effects on the Positive Electrode

As on the negative electrode, a surface layer can also grow on the positive electrode, although to a minor extent. The SEI on the positive electrode side also is formed via side-reactions between the solvent in the electrolyte and the positive electrodes active material (Plett, 2015b).

A bigger impact than SEI growth constitutes the dissolution of metals from the electrode. Depending on the electrodes material, structural disordering may occur which eliminates lithiation sites and leads to capacity fade. Furthermore, the re-deposition of dissolved metal particles on the electrodes surface leads to an increased cell resistance. Another consequence of positive electrode dissolution is the aforementioned anode poisoning. The decomposition of positive electrode material is augmented through operation at very low cell voltages, high temperatures and the presence of hydrofluoric acid in the electrolyte (Vetter et al., 2005; Plett, 2015b).

In consequence of the intercalation and deintercalation process, stress can cause structural *phase transitions* and disordering which may provoke the collapse of lithium pathways. This rapid effect is mostly seen when a cell gets overcharged. In this case too many Li-ions are removed resulting in an unstable electrode structure. This effect reduces the total capacity of the cell and increases the cell's internal resistance (Plett, 2015b). An overview of the ongoing ageing effects in the positive electrode is shown in Figure 2.4. Furthermore, it shows the ageing mechanisms related to inactive constituents of a cell. These mechanisms are described in the subsequent section.

2.2.3 Ageing Effects on Inactive Cell Components

So far, we described the ageing mechanisms of Li-ion cells only with respect to the involved active material. In general, the electrodes of Li-ion cells are composites consisting of active materials, conductive additives and binders. Conductive additives, for instance carbon, are added to increase the electrical conductivity within the electrode. Binders like polyvinylidene difluoride PVdF are used to maintain mechanical stability and contact between the single particles (Plett, 2015b). Figure 2.5 shows the principal components of an electrode.

The individual constituents add to the ageing in the following ways: Due to the volume change caused by lithiation the binder may disengage which results in weakening of mechanical and electrical contact throughout the electrode particles and at the

2 Fundamentals

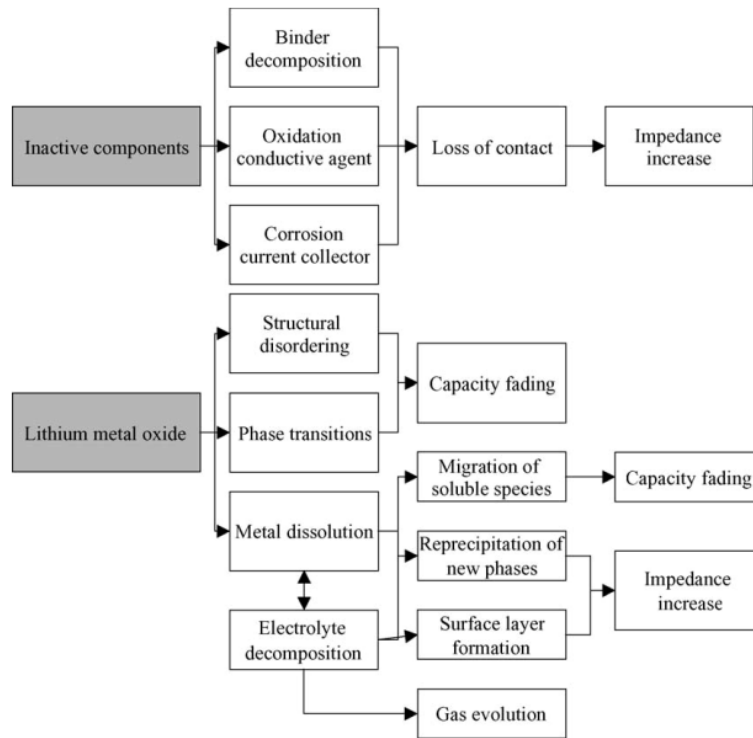


Figure 2.4: Overview of predominant ageing mechanisms in the positive electrode of Li-ion cells and inactive materials (Vetter et al., 2005)

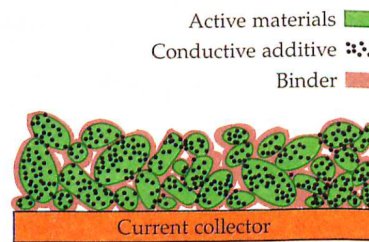


Figure 2.5: layout of composite electrode structure (Plett, 2015b)

interface between electrode particles and the current collector. This leads to increased cell resistance. Sometimes clusters of particles get completely isolated from the bulk material which results in additional capacity loss (Plett, 2015b).

Another ageing mechanism occurs at the current collectors, which can corrode. As a consequence, the conductivity at the electrode/current collector contact decreases, because corrosion products in general have low conductivity. This results in higher cell resistance. These ageing effects occur at the positive and negative side of the cell (Plett, 2015b).

2.3 Li-ion Battery State Estimation

As we already mentioned in chapter 1, the BMS plays a very important role in operating a battery system. As a monitoring and controlling system its purpose is to guarantee for optimal and safe operation over a battery pack's whole lifetime. To achieve this, the present status of the individual cells has to be known precisely. Two important values which describe the present condition of a cell are State of Charge (SoC) and State of Health (SoH). Since these variables are not directly measurable, suitable estimation methods are required. This section gives a more detailed definition of these quantities and a brief overview of the common techniques used for their estimation.

2.3.1 State of Health (SoH) Estimation

The State of Health (SoH) is a variable for expressing the present ageing status of a battery cell. There exists no overall definition of SoH. However, the two most common ones are presented in the following:

Definition 1: In a wide range of studies SoH is defined based on the cell's capacity fade. These consider applications as EVs or Plugin HEVs (PHEVs), where available electrical energy is of outstanding importance (Nuhic et al., 2013; Ecker et al., 2012). Therefore, an accurate method to estimate present total capacity is needed. The methods for SoH estimation which are investigated within this work also consider SoH defined as expressed by

$$SoH(t) = \frac{Q_{tot}(t)}{Q_{nom}} \cdot 100\%, \quad (2.1)$$

where Q_{nom} is the cell's nominal capacity and Q_{tot} refers to the cell's actual total capacity. In this definition SoH can theoretically vary between 0% and 100%. Here $SoH = 100\%$ refers to a cell which is completely unaged. In the automotive application field $SoH = 80\%$ refers to a cell which reached its EoL.

Definition 2: Alternatively, SoH can be defined based on power fade. This refers to a cell's decreasing ability to deliver electrical power to an external circuit which originates from internal resistance growth due to ageing. With increasing internal resistance the available power of a cell decreases due to higher internal voltage drop. In literature, a cell's EoL based on power fade is often described as the date, when internal resistance doubled (Ecker et al., 2012; Pistoia & Liaw, 2018). The SoH based on this criteria is defined by:

$$SoH(t) = 1 - \frac{R(t) - R_{init}}{R_{init}}, \quad R_{init} \leq R(t) \leq 2R_{init}, \quad (2.2)$$

where R_{init} is the cell's initial internal resistance and $R(t)$ the present internal resistance. According to this definition SoH can vary between 0 and 1. Here $SoH = 0$ refers to a cell which reached its EoL by doubling of internal resistance. $SoH = 1$ refers to a cell which is completely unaged.

2.3.1.1 On-board Capacity Estimation

In this thesis SoH is considered as being based on capacity fade and is described via expression 2.1. Therefore, an accurate capacity estimation method is key to adequate SoH estimations. In this section the general approach and challenges of on-board capacity estimation are described followed by a brief overview of different methods.

Fully charged: We refer to a cell being *fully charged* if its OCV reaches an upper threshold voltage $v_h(T)$, which is specified by the manufacturer and temperature dependent. The common procedure to *fully charge* a cell is by applying a constant current until $v_h(T)$ is reached. This is followed by a Constant-Voltage (CV) charging phase. During CV-phase the charge current is adjusted to stabilize the terminal voltage of the cell at $v_{terminal} = v_h$. This phase lasts until the current comes below an arbitrary small threshold. The state *fully charged* relates to $SoC = 100\%$.

Fully discharged: We refer to a cell being *fully discharged* if its OCV reaches a lower threshold voltage $v_l(T)$, which is specified by the manufacturer and temperature dependent. The common procedure to *fully discharge* a cell is by applying a negative constant current until $v_l(T)$ is reached. This is followed by a constant voltage (CV) charging phase which lasts until the current comes below an arbitrary small threshold. The state *fully charged* relates to $SoC = 0\%$.

The most straight forward way to obtain a precise value for Q_{tot} would be to discharge a cell from its *fully charged* state to its *fully discharged* state while summing up the extracted electric charge. To obtain comparable values this would have to be done under constant temperature and with a well defined discharge current (Zhang & Lee, 2011). Such a scenario is executable under laboratory conditions. Under real conditions these criteria are hardly able to be fulfilled. Therefore, other approaches for capacity estimation are required.

Based on the considerations of Farmann et al. (2015), on-board capacity estimation methods generally can be compartmentalized as follows:

1. *Voltage-based estimation methods*: the relationship between electro motive force (EMF) and SoC is used for capacity estimation.
2. *Electrochemical model-based methods*: electrolyte conductivity and electrode's porosity are used as indicators for SoH estimation.
3. *Methods based on the analysis of charging characteristics*: Incremental Capacity Analysis (ICA), Differential Voltage analysis (DVA), Constant-Voltage CV phase analysis.
4. *Aging prediction methods*: ageing models are used to predict capacity fade and power fade based on the present operation conditions and past history.

The techniques being used for the purpose of this work are *voltage-based methods* and *methods based on the analyse of charging characteristics*. A detailed description of those is given in Chapter 3 and Chapter 4.

2.3.2 State of Charge (SoC) Estimation

As for any energy storage system the information of the amount of available energy is of great importance.

Definition: A battery cell's State of Charge (SoC) is the ratio of its remaining capacity to its actual total capacity.

$$SoC(t) = \frac{Q_{remaining}(t)}{Q_{tot}(t)} \cdot 100\% \quad (2.3)$$

In electric vehicles SoC relates to the ability to predict range precisely. Unlike as for classic vehicles where the available energy is determined by the amount of fuel inside the tank, for Li-ion cells the remaining energy cannot be directly measured. Besides that the capacity of a cell varies with ageing status and temperature. As a result the SoC estimation for electric vehicles is complex and has to be robust against a wide range of conditions (Xiong et al., 2017).

As we will see in the next section, proper SoC estimation is closely related to the ability of accurately estimating total capacity and therefore SoH. Further advantages of a reliable SoC estimation are:

- Optimal operation without the risk of overcharge or overdischarge

2 Fundamentals

- Allowing to exhaust the design limits, so battery packs don't need to be oversized. This leads to volumetric and gravimetric savings.
- Economic benefits due to usage of smaller packs and lower warranty-servicing costs due to higher reliability

2.3.2.1 Coulomb Counting

One of the simplest and most common methods to estimate SoC is coulomb counting. This method is based on integrating the charge/discharge current over time, which is equivalent to the electric charge added or removed from the cell. With the information of initial SoC, its present value can be calculated as

$$SoC(t) = SoC(t_0) - \frac{1}{Q_{tot}} \int_{t_0}^t \eta(t') I(t') dt', \quad (2.4)$$

where $SoC(t)$ is the State of Charge at time t , Q_{tot} is the actual total capacity, $I(t)$ is the electric current and $\eta(t)$ is the coulombic efficiency. The coulombic efficiency is a unitless factor which describes the magnitude of lost charge by side reactions occurring during charge or discharge.

Because SoC is defined as the ratio of residual capacity to actual total capacity, coulomb counting is the most direct method for SoC estimation. Nevertheless, the method has several drawbacks. Firstly, a good estimate for the initial SoC has to be known in order to prevent biased estimates. Secondly, the measurement of current is related to unavoidable errors due to limited accuracy of the current sensor. For accurate estimation the total capacity of the cell has to be known and regularly updated as it varies due to environmental conditions and ageing (Xiong et al., 2017). Meng et al. (2017) mentions that the accuracy of the method could be improved through online estimation of the coulombic efficiency which is also a challenge itself. In summary, coulomb counting is not suitable as a standalone SoC estimation. Nevertheless, the shortages of the method can be compensated when combining it with other methods like OCV-SoC lookup tables or Kalman filter methods.

2.3.2.2 Open-Circuit-Voltage SoC Estimation Method

Another method for SoC estimation is the usage of an OCV-SoC look up table. The OCV is the cell's terminal voltage when it is disconnected from the external circuit and has reached internal equilibrium. For most Li-ion cells, there is a direct monotonic relation between OCV and SoC which has to be accurately measured beforehand and

typed to a look up table like one shown in Figure 2.6. Therefore, if we know the present OCV we can use this table to look up the actual value for SoC. To measure the OCV the cell has to rest long enough, which means the charge/discharge current has to decay to a sufficiently small value close to zero (Xiong et al., 2017; Meng et al., 2017).

With this method one can achieve adequate estimation results without needing information about initial conditions or any long term measurements (Pistoia & Liaw, 2018). Nevertheless, it has several disadvantages. The OCV-SoC relationship varies with temperature and ageing. Therefore, extensive experiments at different conditions may be needed. Another disadvantage is the difficulty in measuring present OCV due to long rest time. Thus, for most online applications the classical OCV method is not quite suitable. Nevertheless, its application field can be extended when it is used in combination with OCV estimation methods or to estimate initial value for other SoC estimation methods like coulomb counting or model-based methods.

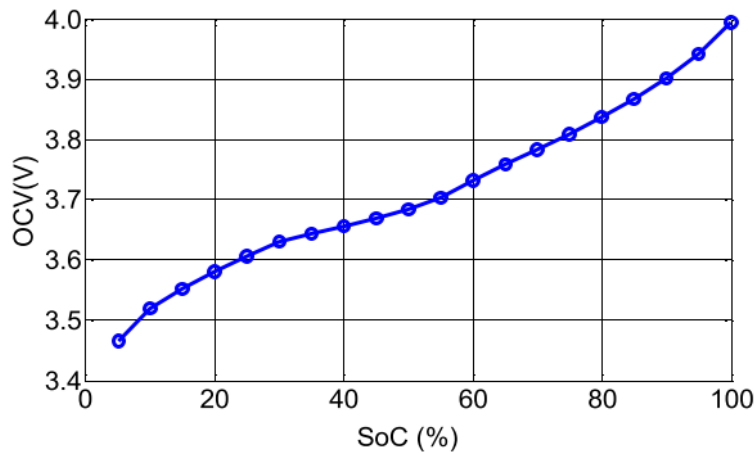


Figure 2.6: Example for OCV curve of a LiPB cell (Xiong et al., 2017)

2.3.2.3 Model-based Methods

We showed that the before mentioned methods are very limited in their applications. Now a more sophisticated group of SoC estimation methods is briefly introduced. In these methods a mathematical cell model is used to estimate the voltage response of a cell to a current input. There have been developed a wide variety of cell models: electrochemical models EM, equivalent circuit models ECM and electrochemical impedance models. A schematic, showcasing the working principle of model-based SoC estimation, is shown in Figure 2.7.

The response of the real cell to an electrical current input is related to its present state.

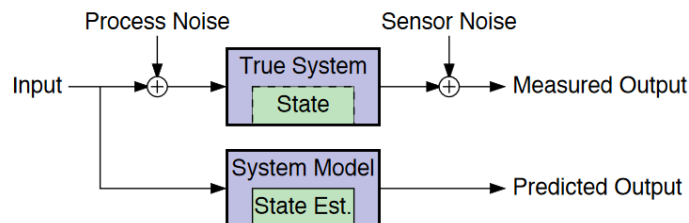


Figure 2.7: Basic structure of model-based SoC estimation methods (Plett, 2015b)

The state of a cell is comprising true SoC, true set of diffusion currents and other quantities which cannot be measured (Plett, 2015b). The cell models predicted output signal is a function of estimators of these state variables we call *state estimate*. If the difference between measured output of the real cell and the model's output is small we have an indicator for adequate cell model and good state estimate. To minimize this difference, nonlinear state estimation algorithms and adaptive filters can be applied. Common algorithms are Kalman filter, Sliding-mode observer, H_∞ -observer etc. (Meng et al., 2017; Zheng et al., 2018).

Model-based SoC estimation is the most common approach for online state estimation of Li-ion cells. Its advantages are robustness against initial SoC offset and measurement noise. Nevertheless, the development of a robust model requires deep understanding of the system and a relative long development time (How et al., 2019).

2.3.2.4 Data-driven Methods

Data-driven estimation methods recently gathered lots of interest. They arose as a result of increasing computational power and availability of big quantity of data. These methods don't require a detailed understanding of the physical and chemical processes taking place inside a cell. In contrast to model-based methods, data-driven SoC estimation is possible with limited prior information which leads to shorter development time. Furthermore, the methods are able to determine their parameters through self-learning. The unpredictability and requirement of large amount of high quality training data are the main drawbacks of these techniques. The most popular data driven SoC estimation approaches are neural network, deep learning, support vector machine and fuzzy logic (How et al., 2019). The methods just mentioned are not dealt with in detail in this work, as this would go beyond the scope of it.

3

Ageing Data Analysis

3.1 Measurement Data

As a first part of this work, measurement data from ageing investigations was organized and analysed. All the measurements for this work were taken at the Virtual Vehicle Research GmbH. For the measurement procedure an Arbin BT-2000 battery testing system and Memmert incubators were used. All measurements were taken with commercial Panasonic NCR18650B cells.

The aim of these measurements is to gain knowledge about the cell's properties, behaviour and how it changes with increasing age. For this purpose, multiple ageing tests under different conditions were performed. Each ageing test procedure was executed over a timespan of about 18 months. As a result, an ageing-dataset is gathered. An entire ageing test procedure consists of an alternating sequence of Reference Test Procedures (RTPs) and Load Profiles (LPs). In more detail it is structured as following:

1. Initial characterisation via execution of multiple RTPs at different temperatures
2. Execution of ≈ 20 ageing repetitions which consist of:
 - LP: lasts roughly 3 weeks followed by
 - RTP at $T = 25^\circ\text{C}$

This corresponds to a test time span of about 18 months.

3. Final characterisation via execution of multiple RTPs at different temperatures

During the ageing repetitions, a cell's capacity and SoH decreases based on the experienced loading conditions. An example for a cell's degradation in SoH during the performance of an ageing-dataset is shown in Figure 3.1. Herein, the scatters refer

3 Ageing Data Analysis

to total cell capacities being measured during the corresponding RTP's at $T = 25^\circ\text{C}$. Between two consecutive scatters a LP was performed.

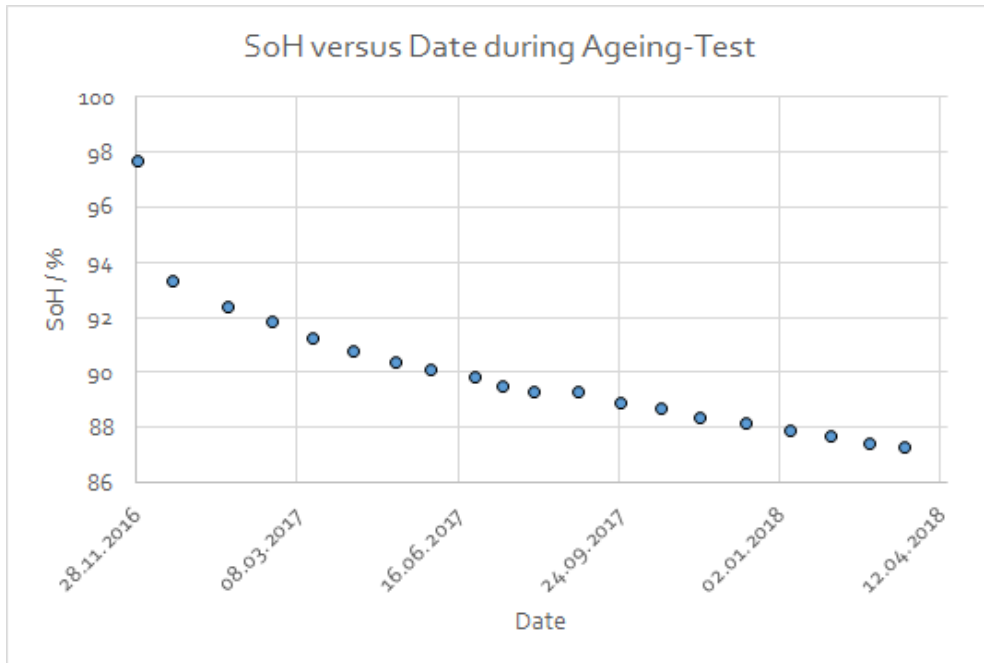


Figure 3.1: Example for a cell's SoH progression during a performance of an ageing test. The scatters refer to total cell capacities being measured during the corresponding RTP's at $T = 25^\circ\text{C}$.

The following sections serve as a detailed description of the terms RTP and LP. After this, an introduction to the methods used for analysis of the gathered ageing-datasets is given followed by the description of the obtained results.

3.1.1 Reference-Test-Protocol (RTP)

At the beginning of an ageing-dataset and between every applied LP a RTP is performed. This procedure is designed in a way to gather most precise information about the cell's present properties. During the execution of a RTP the cell temperature should stay constant at $T = 25^\circ\text{C}$. To achieve this Peltier cooling (model IPP600) combined with forced air cooling was applied. By performing a RTP following information is obtained:

- *Capacity information:* gives insight into the cell's present ageing status as the SoH is defined via capacity fade
- *Dynamic information:* voltage response to input current pulses picture the dynamic behaviour of the cell; This is of major importance for the testing of cell

models which aim to simulate a cell's voltage response to a current input signal as accurately as possible.

The course of action during a RTP is now described in more detail and is displayed schematically in Figure 3.2. Generally it can be split into three test segments:

1. Partial Capacity Determination:

In the first segment of a RTP, the 80%-capacity of the cell is determined. To do so, a charge/discharge operation between 15% and 95% SoC is executed three times, utilizing previously acquired OCV points for the initial SoCs. This happens in the following manner:

1. Constant current charging with $C/3$ until the terminal voltage reaches 4.113 V
2. Constant voltage charging at 4.113 V until the current decays to 160 mA ($\approx C/20$)
3. Constant current discharging with $C/3$ rate until until the terminal voltage reaches 3.498 V
4. Constant voltage discharging at 3.498 V for 40 minutes or until the current decays to 160 mA, respectively

2. Full Capacity Determination:

The 80%-capacity determination is followed by two full capacity cycles according to the data-sheet. Each of these cycles is applied as follows:

1. Constant current charging with $C/2$ until 4.2 V
2. Constant voltage charging at 4.2 V until the current decayed to $C/50$
3. Discharging with $1C$ until 2.5 V

3. Dynamic Behaviour Investigation:

At the beginning of this segment the cell is again charged to $SoC = 95\%$. Afterwards the following sequence is performed at seven specific SoC-levels (80%, 70%, 60%, 50%, 40%, 30% and 20%) to cover the whole operating window of the cell:

1. Discharging to specific SoC-level
2. Application of current input pulses to exhaust the dynamic behaviour of the cell.
3. Discrete stair profile of 0.2 C, 0.35 C, 0.5 C, 0.75 C, 1.25 C for 10 s per level
4. Charging of the cell to $SoC = 95\%$.

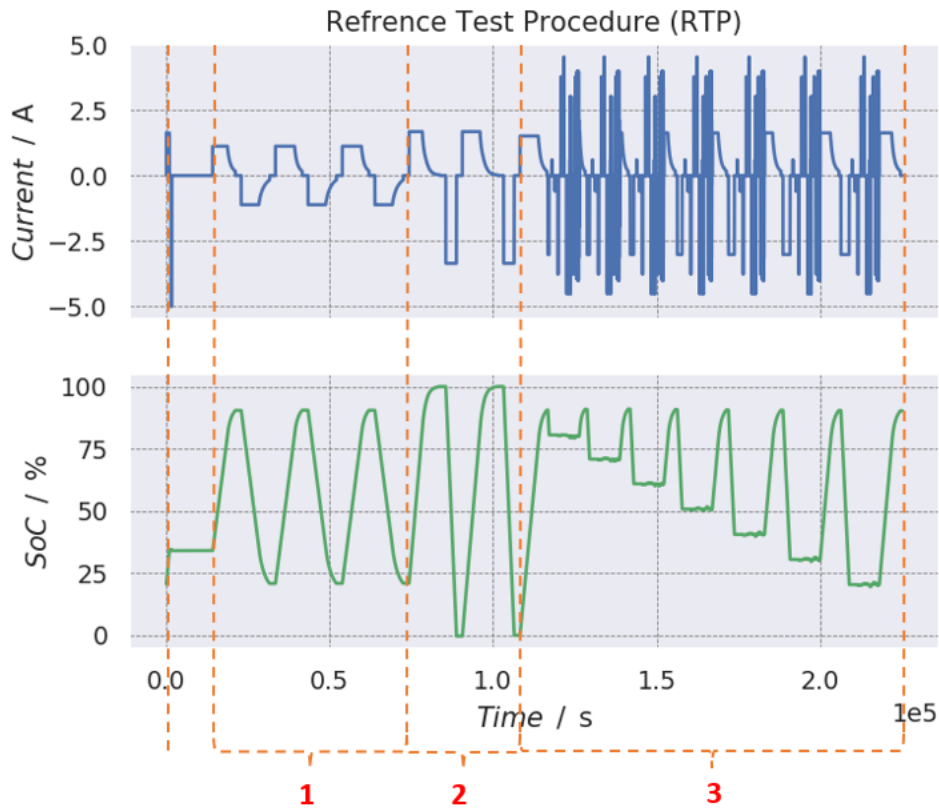


Figure 3.2: RTP example measurement. The upper graph (**blue**) displays measured current (in A) over time. The lower graph (**green**) shows an estimate for the SoC (in %) over time. The dashed lines (**orange**) and the bottom-most labels depict the individual phases of the RTP.

3.1.2 Load-Profile (LP)

A LP is a transient current input which is applied to the cell via the battery testing system. After each RTP a LP is applied to the cell. During these LPs the cell is subjected to its different ageing mechanisms and therefore degrades. As one could imagine, the magnitude in capacity loss and the ageing behaviour in general highly depends on the operating conditions during the performance of a LP. High temperatures and high current rates for example may lead to more intense ageing consequences than moderate cell temperatures and low current rates. To cover a variety of stress scenarios, different sets of LPs were designed for the ageing investigation. These can be grouped into three main categories:

1. Driving Cycles:

These profiles aim to simulate realistic customer usage behaviour. They can either be derived theoretically or originate from real measurements during driving.

2. Calendric LPs:

These are LPs which help to simulate calendric ageing during storage at constant SoC level. Calendric LPs are defined by three parameters:

- $T / ^\circ C$: the target temperature of the cell during storage
- $SoC / \%$: the average State of Charge during storage
- CC / h^{-1} : the average charge current

At this point it has to be clarified why the third parameter is needed to define the calendric LP where the cell should be in rest: During storage the cell slowly discharges, its SoC slightly decreases. Therefore the last parameter CC describes the charge current with which the cell is brought back to the desired SoC before storing.

3. Cyclic LPs:

These LPs serve for the investigation of cycle ageing where the cell gets continuously charged and discharged. A cyclic LP is defined by the following parameters.

- $T / ^\circ C$: the target temperature of the cell
- PDC / h^{-1} : the peak discharge current rate
- ADC / h^{-1} : the average discharge current rate
- $SoC / \%$: the average State of Charge
- $dSoC / \%$: the median value of the SoC-strokes which represents the dominant SoC-deflection
- CC / h^{-1} : the average charge current rate

3.2 Incremental Capacity Analysis of the Constant-Current Charging Phase

The first method applied to the measured ageing-datasets is based on Incremental Capacity Analysis (ICA). ICA techniques have been extensively used in the past to study different degradation mechanisms in Li-ion cells (Dubarry et al., 2011; Berecibar et al., 2016). Recently they were introduced to the field of capacity estimation and SoH estimation respectively.

The general approach of ICA based SoH estimation is to analyse the behaviour of cells during constant-current charging phase. By differentiating the charged capacity relative to the terminal voltage, a corresponding IC-curve is obtained. Then the curve is analysed to extract features which are characteristic for the present SoH. Such features could be peak positions, amplitudes or envelope areas. This procedure is repetitively executed for a wide range of ageing stages. The final goal is to derive an analytical relation between the extracted features and the cell's SoH. So once a feature is detected in real operation mode, the cell's SoH can be estimated via use of the derived relationship.

ICA based methods generally have several advantages as they are computational inexpensive and can often be applied to a wider range of cell chemistries and cell designs (Berecibar et al., 2016). Nevertheless, up to now only a minority of research has been done regarding ICA usage for SoH estimation. For instance, Weng et al. (2013) proposed a method where Support Vector Regression (SVR) is used to identify IC-peak heights as signatures for capacity fade of LiFePO₄ cells. A recent study by Li et al. (2018) proposes a method which derives a quantitative correlation between the IC-peak positions and capacity fade for high energy lithium lithium nickel manganese cobalt oxide (NMC) LIBs. Their estimation method was able to estimate SoH of several cells cycled under different depths of discharge within a maximum error of $\pm 2.5\%$ while requiring moderate computational effort.

3.2.1 Data Organization and Selection of Loading curves

In the context of our investigation ICA is applied to the loading curves obtained during Constant-Current (CC) charging process. As mentioned previously, each ageing-dataset consists of a sequence of RTPs and LPs. For the purpose of the Ageing Data Analysis only the data originating from RTPs performed at a temperature of $T = 25^\circ\text{C}$ was used. Therefore, the required data sets were extracted from a database using an SQL query before they were saved in a data-frame.

3.2 Incremental Capacity Analysis of the Constant-Current Charging Phase

Extraction of Loading curves: During execution of a RTP not only physical quantities are measured. In addition useful meta-data like the *stepindex* gets recorded. This index serves for the identification of different test segments within a RTP. For our purpose the data-points during the second CC charging process within the RTP's *Full Capacity Determination* segment were extracted via this variable. For better understanding, Figure 3.3 displays an example of the scope for the extraction of a loading curve from a RTP.

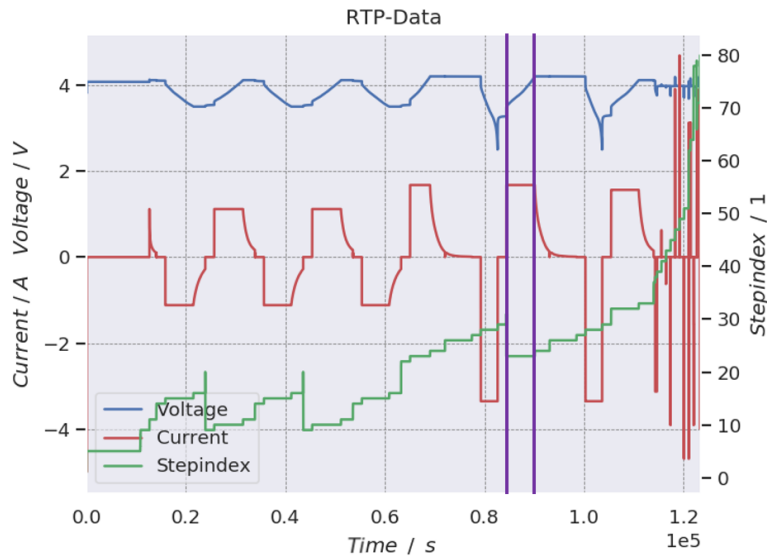


Figure 3.3: Shows partly data collected during execution of a RTP, **blue:** Terminal Voltage V , **red:** Current I , **green:** Stepindex n ; The vertical lines in **violet** mark the scope for the extraction of the data during the CC charging process.

Figure 3.4 shows an example set of loading curves extracted for a cell while being cycle aged. Each loading curve originates from one corresponding RTP. Here, a gradually evolution in colour of the curves from bright to more dark can be seen where the color relates to the cycle-age of the cell. Therefore the brightest curve originates from the completely unaged cell and the darkest curve relates to the last RTP of the ageing test. It can already be seen that the loading curves gradually change during ageing. As a result of higher internal resistance and capacity fade, cells of higher age reach the maximal terminal voltage in less time than unaged cells.

3.2.2 Calculation of IC-Curves

The IC-curve is the backbone of ICA. It graphs the differential capacity $\frac{dQ_c}{dV}$ with respect to the terminal voltage V . The differential capacity is defined as follows and

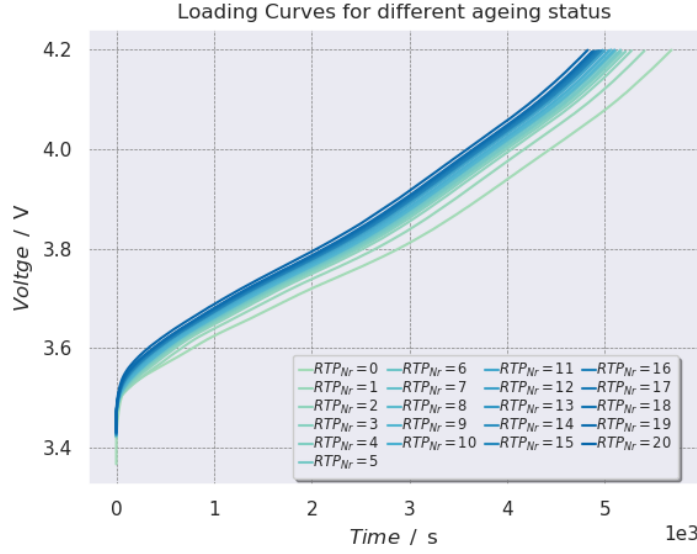


Figure 3.4: Example of a set of loading curves extracted from an ageing-dataset. Brighter curves represent less aged cell status.

can be calculated by numerically differentiating the charged capacity Q_c relative to its terminal voltage V .

$$\frac{dQ_c}{dV} = \frac{I \cdot dt}{dV} \approx \frac{\Delta Q_c}{\Delta V} \quad (3.1)$$

,where ΔQ we call *incremental capacity* and ΔV we call *incremental voltage*. The terminal voltage V and the current I are quantities which are directly measured. These signals are sensed with a certain sample frequency f_s . So the sample index k relates to real time t according to $t = k/f_s$. The most straight forward way to calculate the differential capacity from these measurements would be like:

$$\frac{\Delta Q_c}{\Delta V} = \frac{\bar{I} \cdot (t_{k+1} - t_k)}{V_{k+1} - V_k} \quad (3.2)$$

,where \bar{I} is the average current during the time interval $[t_k, t_{k+1}]$. Usually the directly extracted differential capacity is very noisy due to measurement errors originating from the current sensor. Figure 3.5 shows an example set of noisy IC-curves extracted from an ageing-dataset. A further problem in calculating equation 3.2 is given due to the denominator of the right side of the equation. If V does not change within a timestep, the differential capacity goes to infinity. A small voltage change within a timestep also leads to a highly erroneous value. As we will show, these problems will vanish later as we slightly alter the procedure of smoothing extracted IC-curves.

3.2 Incremental Capacity Analysis of the Constant-Current Charging Phase

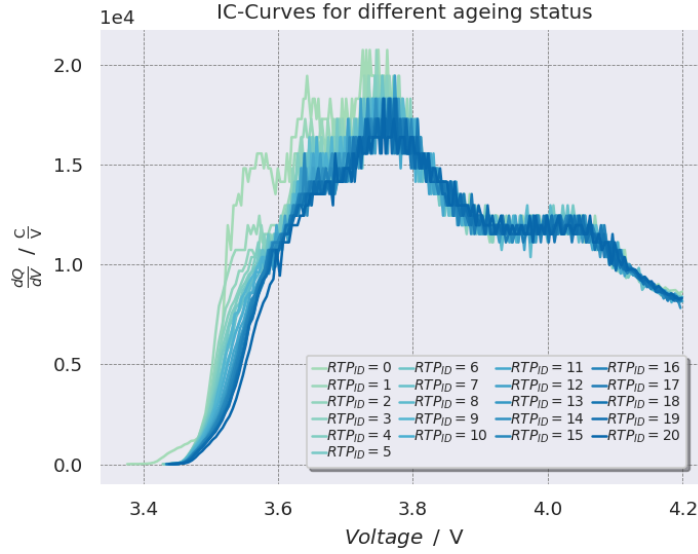


Figure 3.5: Example of a set of noisy IC-curves extracted from an ageing-dataset. Brighter curves represent less aged cell status.

3.2.3 Gaussian Smoothing

Due to the noise issue mentioned in Section 3.2.2, the next important step in ICA is to apply an appropriate smoothing method. According to literature, several different smoothing methods were already used in ICA. Possible methods are moving average filter, Gaussian Smoothing (GS), improved center least squares method (L. Wang et al. (2016)) and Kalman Filter (Tang et al. (2018)). In this thesis GS is used as it sufficiently reduces the noise of the curve while maintaining important information. Besides that, GS is computationally relatively inexpensive. By performing GS each data-point is replaced by a weighted sum of its neighbouring data-points. In a continuous picture the weights of the neighbouring values are given by a Gaussian distribution function

$$G(x) = \frac{1}{\sigma\sqrt{2\pi}} \exp\left(\frac{-(x - \mu)^2}{2\sigma^2}\right), \quad (3.3)$$

where μ is the mean value of the distribution and therefore sets the center position of the distribution function. The standard deviation σ sets the width of the distribution function. When the Gaussian distribution is used for the purpose of smoothing, μ is normally set to zero to put equal emphasis on left and right sided neighbours (Li et al., 2018). For the smoothing operations within this investigation the standard deviation is set to $\sigma = 80$ which removes noise sufficiently while preserving the core information.

Mathematically the smoothing of a function $f(x)$ is described via a convolution of the function with a smoothing function called the kernel $g(x)$.

$$\hat{f}(x) = f * g(x) = \int_{-\infty}^{\infty} f(x - \lambda) \cdot g(\lambda) \, d\lambda = \int_{-\infty}^{\infty} f(x) \cdot g(x - \lambda) \, d\lambda \quad (3.4)$$

When dealing with signal processing mostly discrete convolution is used, which is described by:

$$\hat{f}(n) = (f * g)(n) = \sum_k f(k)g(n - k) = \sum_k f(n - k)g(k) \quad (3.5)$$

For the discrete convolution of two functions the following relationship is valid:

$$\hat{D}f = D(f * g) = (Df) * g = f * (Dg) \quad (3.6)$$

with D being the difference operator.

In our context the differential capacity $\frac{dQ_c}{dV}$ corresponds to Df and the Gaussian distribution function $G(V)$ corresponds to the kernel g . Because we are dealing with discrete convolution in one dimension, the functions f and g are vectors. Under usage of 3.6 we are able to shift the difference operator to the kernel, allowing us to circumvent the aforementioned problem which arises due to calculating 3.2. We obtain a smoothed IC-curve by evaluating

$$\frac{d\hat{Q}_c}{dV}(n) = (Q_c * Dg)(n) = (Q_c * \tilde{g})(n), \quad (3.7)$$

with the vector \tilde{g} being the differentiated Gaussian kernel. The i -th element of the differentiated Gaussian kernel is given by

$$\tilde{g}_i = -\frac{2i - l - 1}{\sigma^3 \sqrt{2\pi}} \exp\left[-\frac{(2i - l - 1)^2}{(8\sigma^2)}\right], \quad i = 1, 2, \dots, l \quad (3.8)$$

with l being the length of \tilde{g} and σ specifying the width of the smoothing function. For our investigations the used kernel is specified by $l = 699$ and $\sigma = 80$. With these parameters noise is reduced sufficiently while preserving the core information. The length of the vector Q_c was about $l_{Q_c} \approx 4600$. An example for a set of smoothed IC-curves is shown in Figure 3.6.

3.2 Incremental Capacity Analysis of the Constant-Current Charging Phase

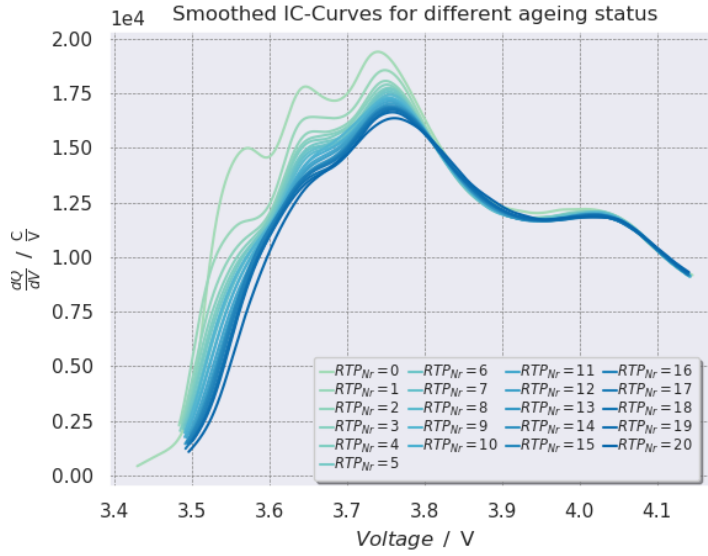


Figure 3.6: Example of a set of smoothed IC-curves extracted from an ageing-dataset. Brighter curves represent less aged cell status.

3.2.4 Localization of Feature Points

The next step in ICA is to find a feature in the IC-curve which relates to the present SoH of the corresponding cell. There are several candidates for features like positions of local maxima or points of inflection, peak amplitudes or envelope areas. Therefore, multiple tests with different feature candidates were carried out. Like in the work of Li et al. (2018), for the investigated cells the position of an IC-peak has shown to be the most suitable candidate as feature. To be more precise, the second maximum from the right side which lies in a voltage range of (3.7 – 3.8) V delivered the best results. Thus, we refer to it as Feature Point FP. Figure 3.7 shows an example set of smoothed IC-curves and the corresponding Feature Points (FPs). It can already be seen that there is a horizontal drift in position of the FPs with increased ageing and capacity fade respectively.

3.2.5 Linear Regression of SoH versus FP-location

Now that the FPs have been extracted, a relationship between them and SoH of the cell should be found. With this, SoH can be easily estimated whenever a FP is detected during a constant current charging process. To derive such a relation the SoH has to be calculated according to Equation 2.1. The present total capacity of the cell was calculated by coulomb counting via current integration over a complete CC-CV charging process:

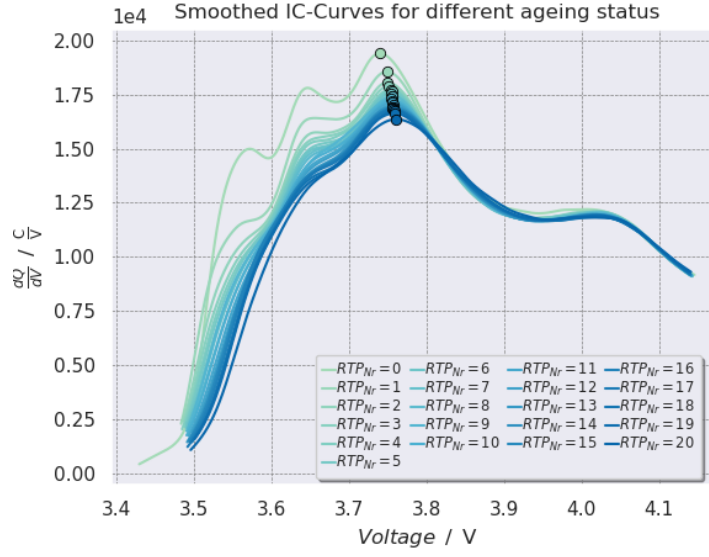


Figure 3.7: Example of a set of smoothed IC-curves with FPs from a ageing-dataset. The extracted FPs correspond to the second local maxima from the right side. Brighter curves represent less aged cell status.

$$Q_{tot} = \int_{t_0}^{t_1} \eta(t') I(t') dt', \quad (3.9)$$

where t_0 corresponds to the starting time of CC charging and t_1 to the end time of CV charging. For the coulombic efficiency, $\eta(t) \approx 1 \forall t$ was assumed. For the evaluation of the integral, trapezoidal numerical integration was used. Figure 3.8 shows a scatter plot of the FP-location with respect to present SoH. For the quantitative description of this relationship, a linear least squares regression was performed using the python function `stats.linregress` from the `scipy` module. Here σ is the Root Mean Square Error (RMSE) of residuals. For n observations y_i and its corresponding estimates \hat{y}_i , σ is calculated by

$$\sigma = \sqrt{\frac{1}{n} \sum_{i=1}^n (y_i - \hat{y}_i)^2}. \quad (3.10)$$

Furthermore R^2 gives the coefficient of determination and is calculated by

$$R^2 = \frac{\sum_{i=1}^n (y_i - \hat{y}_i)^2}{\sum_{i=1}^n (y_i - \bar{y})^2}. \quad (3.11)$$

The defining parameters of the fit function are also shown in the textbox at the bottom left of the figure. The gradient of the regression line is described by k with its unit being $\frac{\%}{V}$. The intercept with SoH-axis is given by the parameter d with its unit being %.

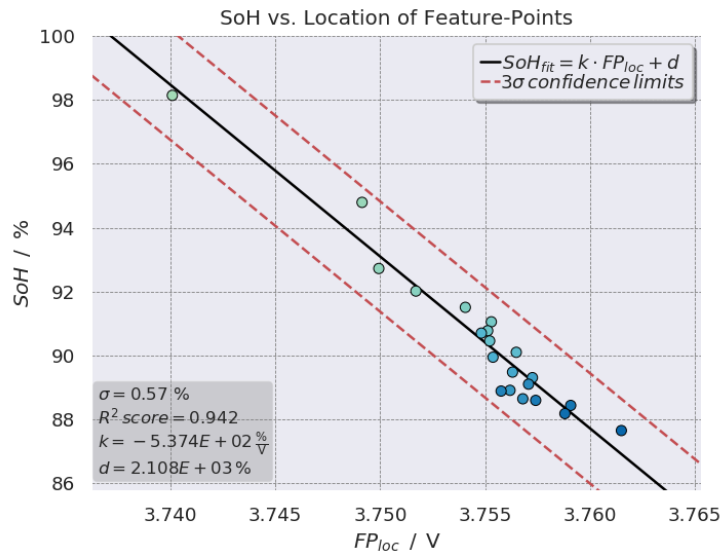


Figure 3.8: Example scatter plot of the FP-location versus SoH for a single cell. Brighter dots refer to less aged cell status.

3.3 ICA: Implementation and Results

To revisit, the aim of ICA is to find a relation between features of the IC-curves and the cell's SoH in order to be able to easily estimate SoH. To test the ICA method (see Section 3.2) and gather information about its range of application, it was applied to a variety of ageing-datasets. These datasets originate from calendric ageing tests, drive cycle ageing tests and cyclic ageing tests. The ageing-datasets were chosen according to their corresponding LPs's defining parameters. The aim of this selection is to cover a wide range of possible ageing scenarios. For each chosen LP, there are three cells which were aged under these conditions to take account of fluctuations. For each LP the method was applied once for all three cells together. The selection of LPs and the corresponding results are described in the following subsections. An overview of the obtained results can be seen in Table 3.3.

3.3.1 Drive Cycle Ageing

The scenario of drive cycle ageing gives insight on how applicable the used ICA-method is for estimating the SoH under real conditions. For the investigation of drive cycle ageing the cells were aged with a LP specified by an automotive partner of the Virtual Vehicle Research GmbH. Its duration is about one week and it aims to describe the

3 Ageing Data Analysis

driving behaviour of a full-time employee with daily car use for job arrival and weekend use for outdoor pursuits. Due to legal reasons, we are not allowed to present any further information regarding this LP. Nevertheless, the gained results of the ICA from the drive cycle ageing tests are shown in Figure 3.9.

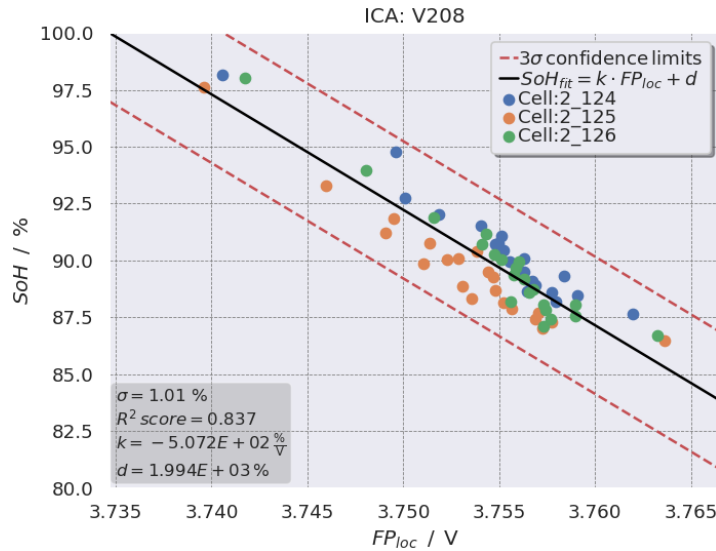


Figure 3.9: Linear fit of the FP-location versus SoH for three cells. Each of the cells was aged with the same drive cycle LP.

It can be clearly seen, that there is a linear relationship between FP-location and SoH. The fit function (black) was obtained by performing a linear regression for all cells together. With it we are able to estimate a cell's SoH based on the peak position in the present Incremental Capacity (IC)-curve. The red lines indicate three-sigma confidence intervals. Within these over 99.7% of the data-points can be found. Between the individual cells there is a noticeable vertical offset in SoH. We assume that this originates from fluctuations within the cell manufacturing process and storage conditions.

3.3.2 Calendric Ageing

For the investigation of calendric ageing, six LPs were chosen to display the effects of:

- Different SoC during storage
- Different temperature during storage

Table 3.1 lists the chosen LPs for the investigation of calendric aged cells as well as

their defining parameters:

Table 3.1: LPs for the investigation of calendric ageing

LP	$T/^\circ\text{C}$	SoC/%	CC/h ⁻¹
L201	0	15	0.25
L202	45	15	0.50
L203	0	55	0.25
L204	30	55	0.50
L205	20	95	0.50
L206	45	95	0.50

Variation of SoC: The figures 3.10a and 3.10b display the effect of different SoC-levels during calendric ageing at a temperature of $T = 45^\circ\text{C}$. In the case of L202 the cells were stored with $SoC = 15\%$, whereas L206 corresponds to a SoC-level of $SoC = 95\%$. As expected, the cells which were stored under a high SoC-level experienced more capacity fade and loss in SoH respectively. The different values for σ show that the applied ICA method yields a more accurate result for the gentle ageing by L202. For both LPs the R^2 score is relatively high which validates the linear regression.

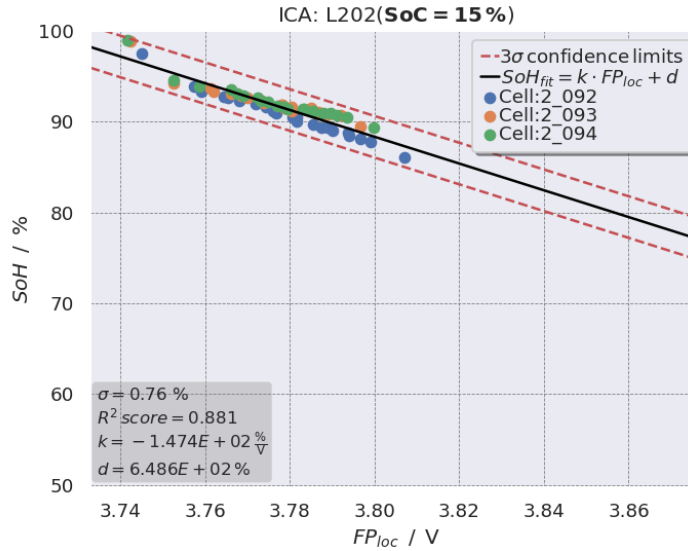


Figure 3.10a: Scatter plot of the FP-location versus SoH for cells being aged calendric by L202: $T = 45^\circ\text{C}$, $SoC = 15\%$

The subsequent figures 3.11a and 3.11b aim to illustrate the effect of different SoC-level during calendric ageing with a storage temperature of $T = 0^\circ\text{C}$. In the case of L201

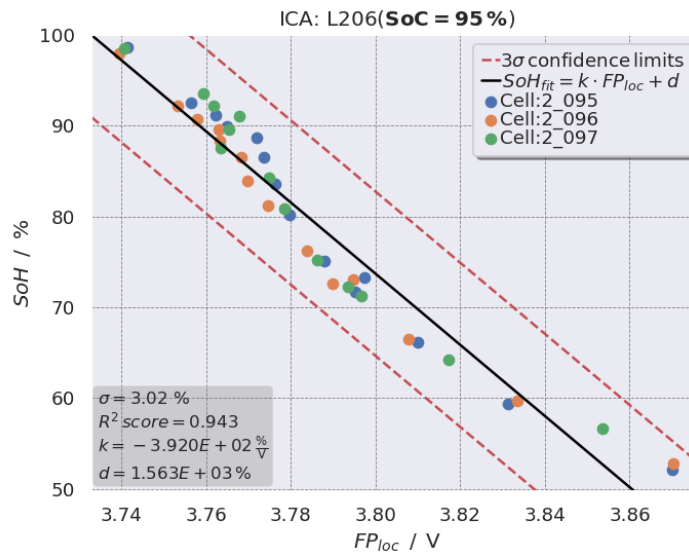


Figure 3.10b: Scatter plot of the FP-location versus SoH for cells being aged calendric by L206: $T = 45 \text{ }^\circ\text{C}$, $SoC = 95 \%$

the cells were stored with $SoC = 15 \%$, whereas L203 corresponds to a SoC-level of $SoC = 55 \%$. In this case a higher SoC-level during calendric ageing did not lead to more capacity fade but to a more spread out mapping of the FP-location versus SoH. This results in a higher σ and a lower R^2 score.

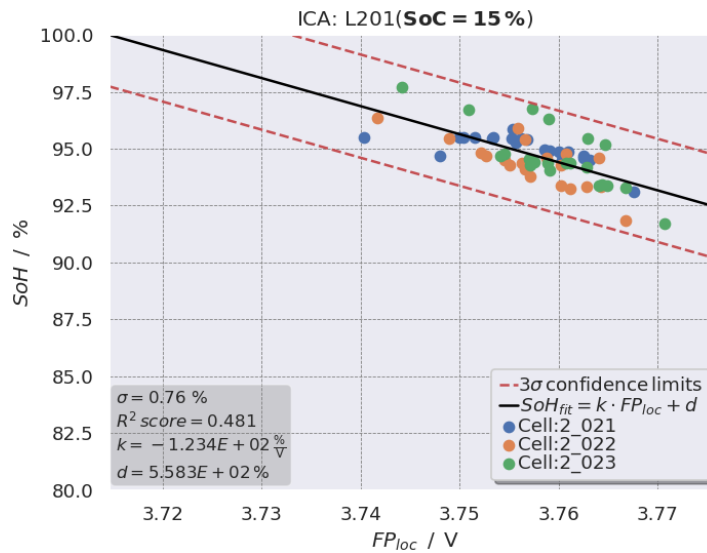


Figure 3.11a: Scatter plot of the FP-location versus SoH for cells being aged calendric by L201: $T = 0 \text{ }^\circ\text{C}$, $SoC = 15 \%$

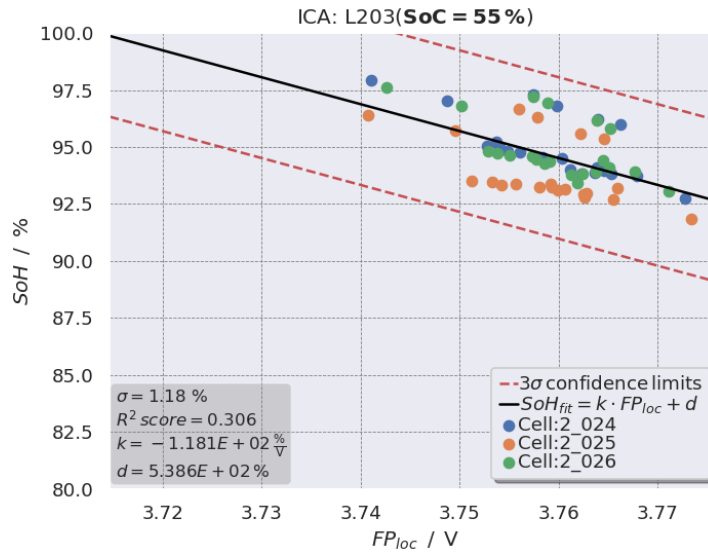


Figure 3.11b: Scatter plot of the FP-location versus SoH for cells being aged calendric by L203: $T = 0^\circ C$, $SoC = 55 \%$

Variation of Temperature: The following figures display the effect of different temperature during calendric ageing on the performance of the applied ICA. The figures 3.12a and 3.12b show the ICA-results of cells being aged by the LPs L201 and L202. Both of these LPs are characterized by $SoC = 15 \%$. In the case of L201 the cells were stored with $T = 0^\circ C$, whereas L202 corresponds to a temperature of $T = 45^\circ C$. The results from L202 (higher T) show increased capacity fade and a slightly steeper

3 Ageing Data Analysis

slope. Nevertheless, the accuracy for both regressions is equal with $\sigma = 0.76\%$.

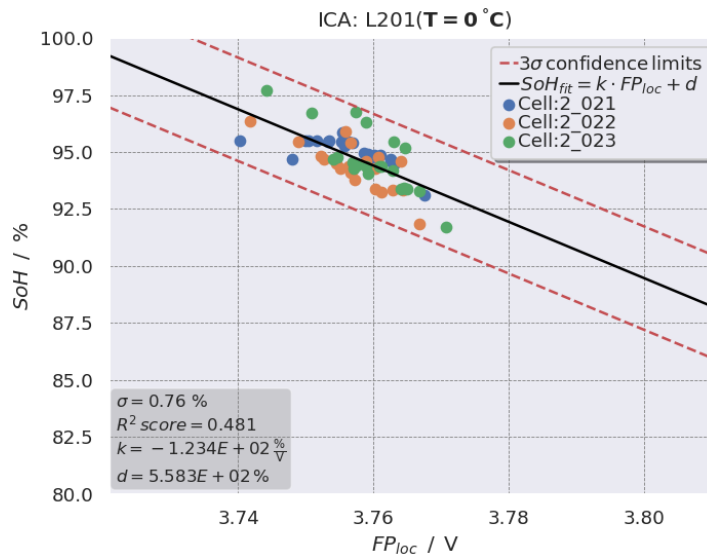


Figure 3.12a: Scatter plot of the FP-location versus SoH for cells being aged calendric by L201: SoC = 15 %, $T = 0\text{ }^{\circ}\text{C}$

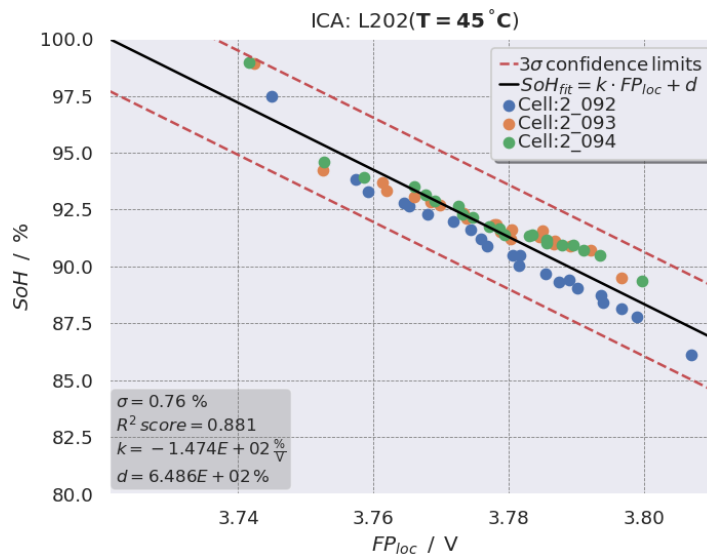


Figure 3.12b: Scatter plot of the FP-location versus SoH for cells being aged calendric by L202: SoC = 15 %, $T = 45\text{ }^{\circ}\text{C}$

The hereafter figures 3.13a and 3.13b display the effect of different temperature during calendric ageing with a constant SoC-level of $SoC = 55\%$. In the case of L203 the cells were stored with $T = 0\text{ }^{\circ}\text{C}$, whereas L204 corresponds to a temperature of $T = 30\text{ }^{\circ}\text{C}$. Like in the previous comparison, the cells stored under higher temperature experienced

3.3 ICA: Implementation and Results

more capacity fade. The accuracy of both linear regressions is very similar but lower than for the ageing at $SoC = 15\%$ (figures 3.12a and 3.12b).

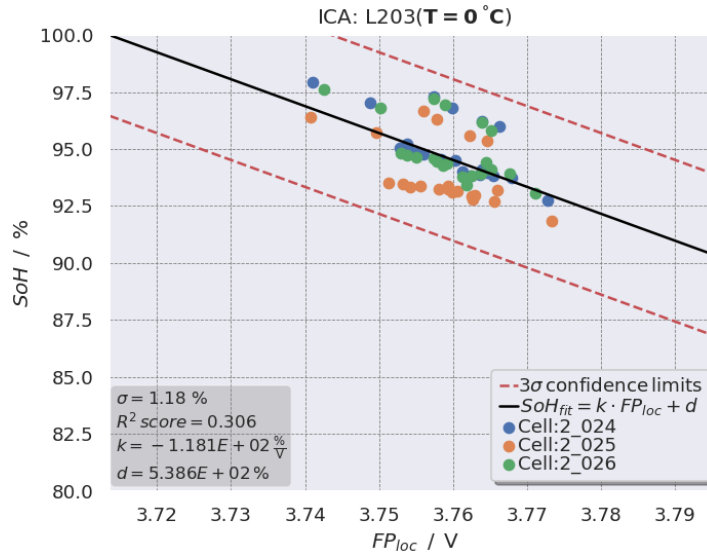


Figure 3.13a: Scatter plot of the FP-location versus SoH for cells being aged calendric by L203: $SoC = 55\%$, $T = 0\text{ °C}$

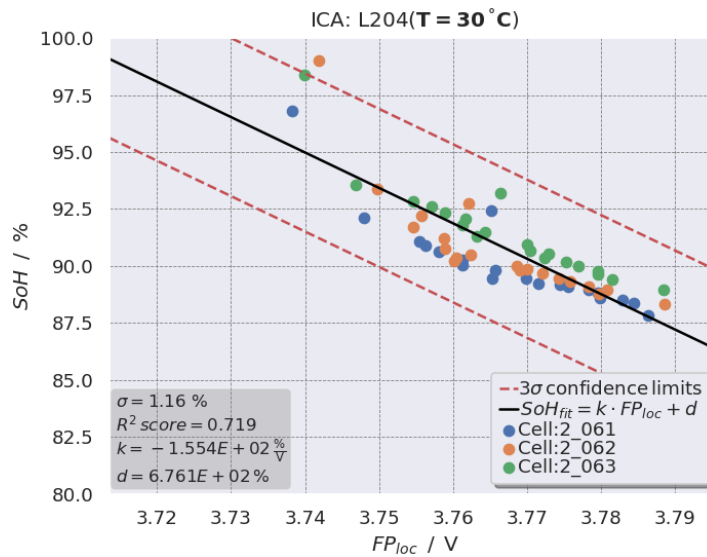


Figure 3.13b: Scatter plot of the FP-location versus SoH for cells being aged calendric by L204: $SoC = 55\%$, $T = 30\text{ °C}$

3 Ageing Data Analysis

Figures 3.14a and 3.14b display the effect of different temperature during calendric ageing with a constant SoC-level of $SoC = 95\%$. In the case of L205 the cells were stored with $T = 20^\circ\text{C}$, whereas L206 corresponds to a temperature of $T = 45^\circ\text{C}$. It can be seen that a difference in storage temperature has a big influence on calendric cell ageing at a high SoC-level. Like in the comparisons before, the linear regression for the cells stored under higher temperature shows higher σ , but a flatter slope (lower $|k|$).

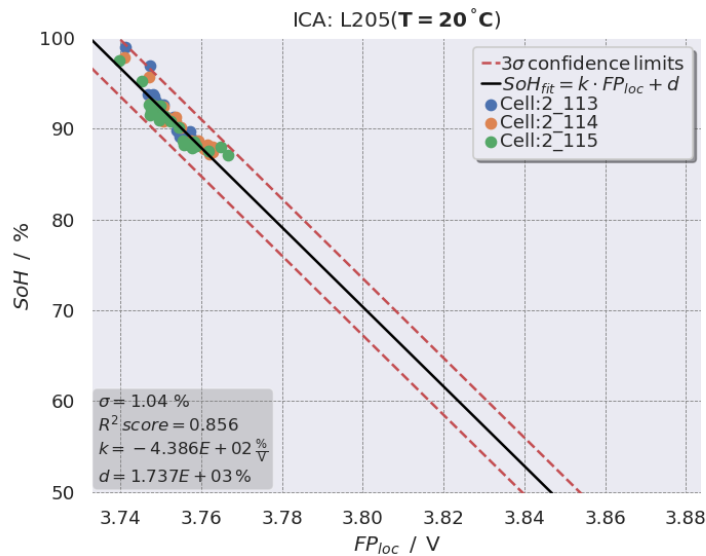


Figure 3.14a: Scatter plot of the FP-location versus SoH for cells being aged calendric by L205: $SoC = 95\%$, $T = 20^\circ\text{C}$

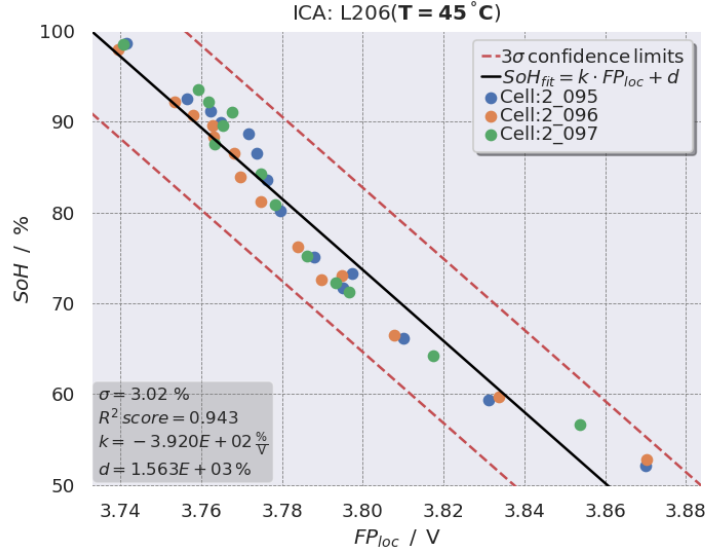


Figure 3.14b: Scatter plot of the FP-location versus SoH for cells being aged calendric by L206: SoC = 95 % , $T = 45\text{ }^{\circ}\text{C}$

3.3.3 Cycle Ageing

For investigating the performance of the applied ICA on cycle aged cells four LPs were chosen to display the effects of:

- Different temperature during cycling
- Different dSoC during cycling

Table 3.2 lists the chosen LPs for cyclic aged cells and their defining parameters:

Table 3.2: LPs for the investigation of cyclic ageing

LP	$T/^{\circ}\text{C}$	PDC/h^{-1}	ADC/h^{-1}	SoC/%	dSoC/%	CC/h^{-1}
L208	0	1.5	1.5	55	2.5	0.05
L209	45	1.5	0.9	55	2.5	0.05
L215	0	1.5	0.3	55	80	0.05
L216	45	1.5	0.3	55	80	0.05

Variation of Temperature: The two figures 3.15a and 3.15b aim to illustrate the effect of different temperature for cyclic ageing with $dSoC = 2.5\%$. In the case of L208 the cells were stored with $T = 0\text{ }^{\circ}\text{C}$, whereas L209 corresponds to a temperature of $T = 45\text{ }^{\circ}\text{C}$. It can be seen that the applied ICA tends to be unstable for low dSoC and low temperature since the R^2 score is close to zero. Nevertheless, for higher temperature

3 Ageing Data Analysis

(shown by 3.15b) the regression derived by the applied ICA has a high R^2 score and low sigma of $\sigma = 0.73\%$.

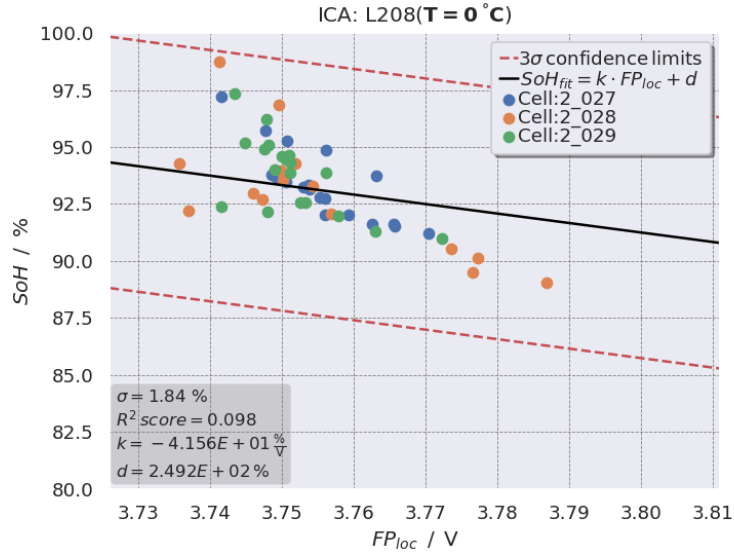


Figure 3.15a: Scatter plot of the FP-location versus SoH for cells being aged cyclicly by L208: $dSoC = 2.5\%$, $T = 0\text{ }^\circ\text{C}$

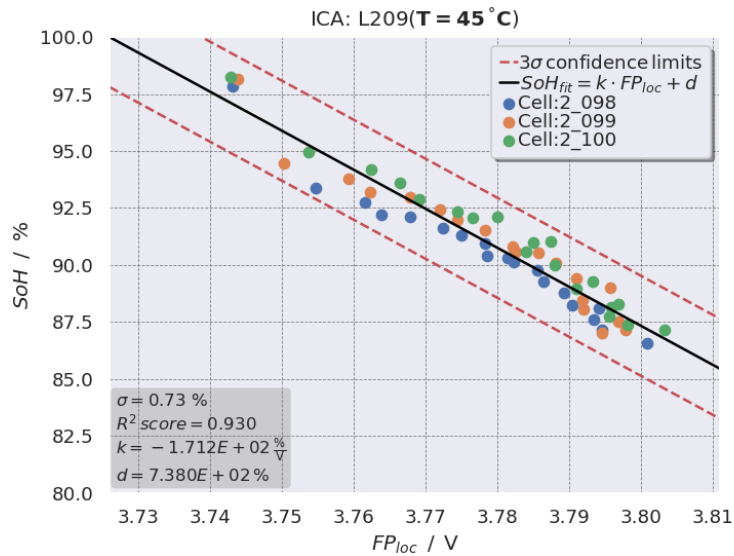


Figure 3.15b: Scatter plot of the FP-location versus SoH for cells being aged cyclicly by L209: $dSoC = 2.5\%$, $T = 45\text{ }^\circ\text{C}$

The subsequent figures 3.16a and 3.16b display the effect of different temperature during cyclic ageing with a high $dSoC = 80\%$. In the case of L215 the cells were stored with $T = 0\text{ }^\circ\text{C}$, whereas L216 corresponds to a temperature of $T = 45\text{ }^\circ\text{C}$. Like

3.3 ICA: Implementation and Results

expected, higher temperature during cycling leads to more capacity fade. Besides this effect, a steeper slope and slightly lower accuracy (higher σ) of the linear regression can be observed for the higher temperature ageing by L216.

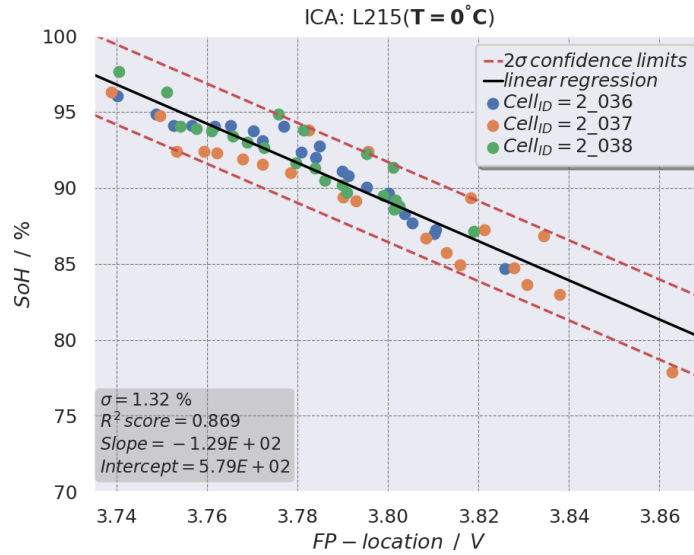


Figure 3.16a: Scatter plot of the FP-location versus SoH for cells being aged cyclic by L215: $dSoC = 80\%$, $T = 0^\circ C$

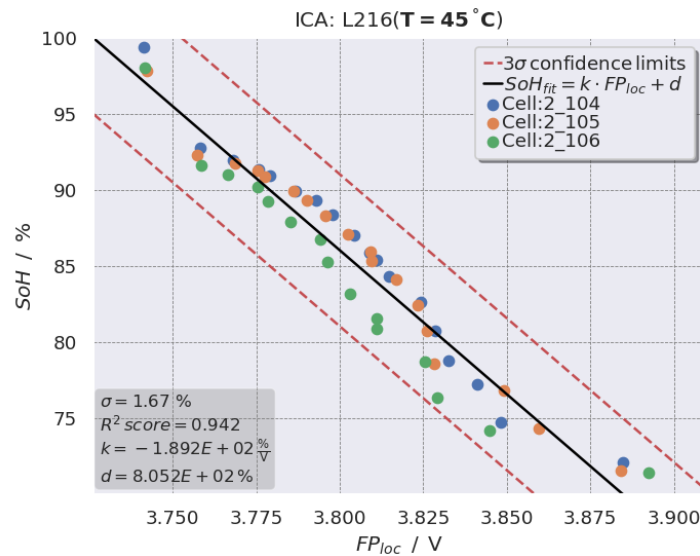


Figure 3.16b: Scatter plot of the FP-location versus SoH for cells being aged cyclic by L216: $dSoC = 80\%$, $T = 45^\circ C$

Variation of dSoC: The figures 3.17a and 3.17b display the effect of different $dSoC$ during cyclic ageing under a temperature of $T = 45^\circ C$. In the case of L209 the cells

3 Ageing Data Analysis

were cycled with $dSoC = 2.5\%$, whereas L216 corresponds to $dSoC = 80\%$. As expected, the cells which were cycled with high $dSoC$ experienced more capacity fade. The narrower three-sigma bounds in 3.17a again show that the linear description of a cell's SoH vs FP-location, obtained through ICA, is more accurate for gentle ageing. For both LPs the R^2 score is relatively high, which validates the linear regression.

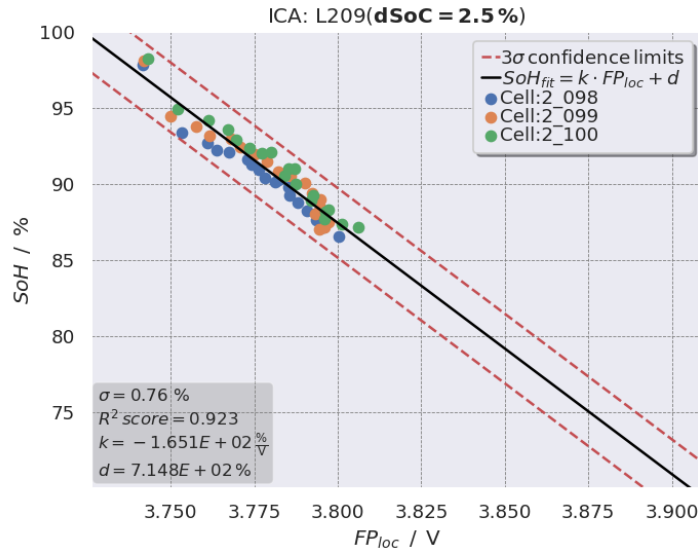


Figure 3.17a: Scatter plot of the FP-location versus SoH for cells being aged cyclic by L209: $T = 45^\circ\text{C}$, $dSoC = 2.5\%$

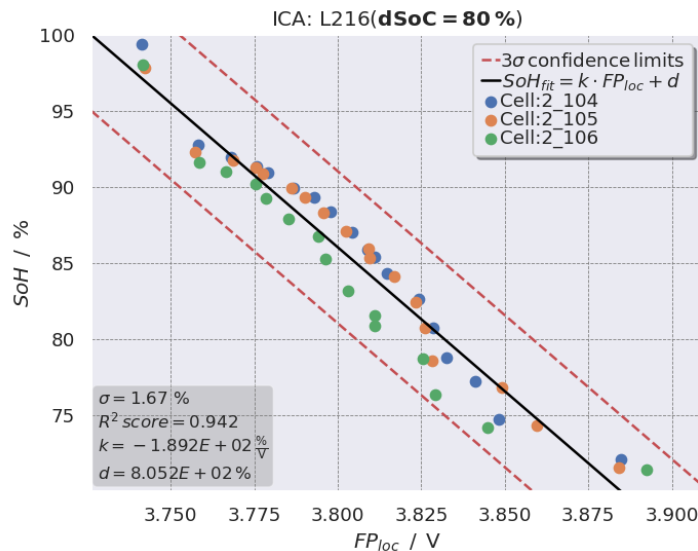


Figure 3.17b: Scatter plot of the FP-location versus SoH for cells being aged cyclic by L216: $T = 45^\circ\text{C}$, $dSoC = 80\%$

A more detailed discussion of the presented results obtained via the ICA method as well as the major outcomes regarding the method's performance for SoH estimation is presented in section 3.6.

3.4 Analysis of the Constant-Voltage Charging Phase

In this section the measurement data recorded during constant voltage (CV) charging is investigated. As for ICA, the aim of this investigation is to derive a relationship between a certain feature of the measurement data and the cell's SoH. Figure 3.18 displays the decay of the current signal during CV charging. In contrast to ICA, we now examine the charging current I with respect to time t instead of differential capacity $\frac{dQ_c}{dV}$ with respect to terminal Voltage V .

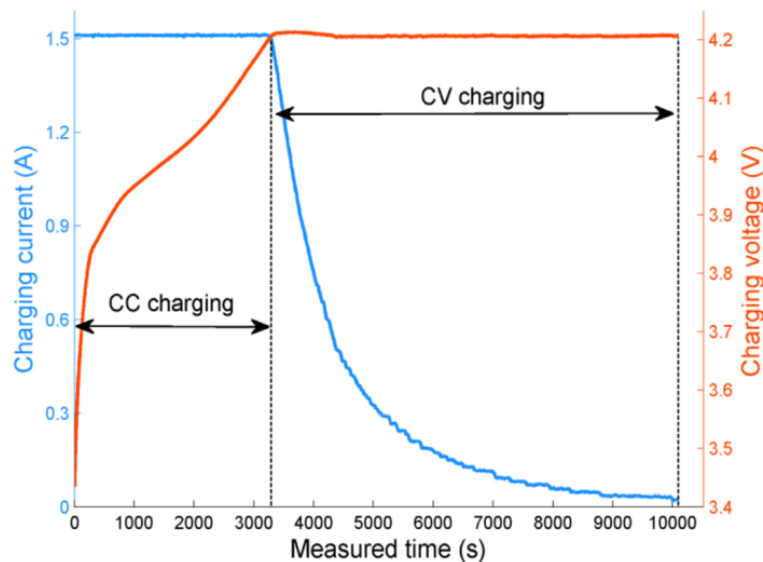


Figure 3.18: Typical CC-CV charging process of a lithium-ion cell (Z. Wang et al., 2019)

Up to now only a few studies on evaluating the characteristics of CV charging process exist. A recent study by Z. Wang et al. (2018) proposes a method which combines quantum computing theory with a classical machine learning technique and applies it to a data repository for Li-ion batteries provided by NASA Ames Prognostic Center of Excellence. In this study the charged capacity during CV charging is expected to be the ageing feature. Z. Wang et al. (2019) also examines the data respiratory from NASA. In this study and in the work of Yang et al. (2018), the dynamic behaviour of CV charging current is investigated and a physical related decay-constant is extracted as a battery health indicator. The work of Eddahech et al. (2014) deals with the investigation of calendric ageing of four battery technologies (NCA, NMC, LiFeMg and

LiFePO₄). That study also considers the time dependence of the CV charging current to be characteristic for ageing and capacity loss respectively.

3.4.1 Data Extraction

As mentioned in Section 3.2.1, only the data originating from RTPs performed at a temperature of $T = 25^\circ\text{C}$ was used. For the analysis of the CV charging process the data-points during the second CV charging process within each RTPs *Full Capacity Determination* segment were extracted. For better understanding Figure 3.19 displays an example of the scope for the extraction of the current decay during CV charging process from a RTP.

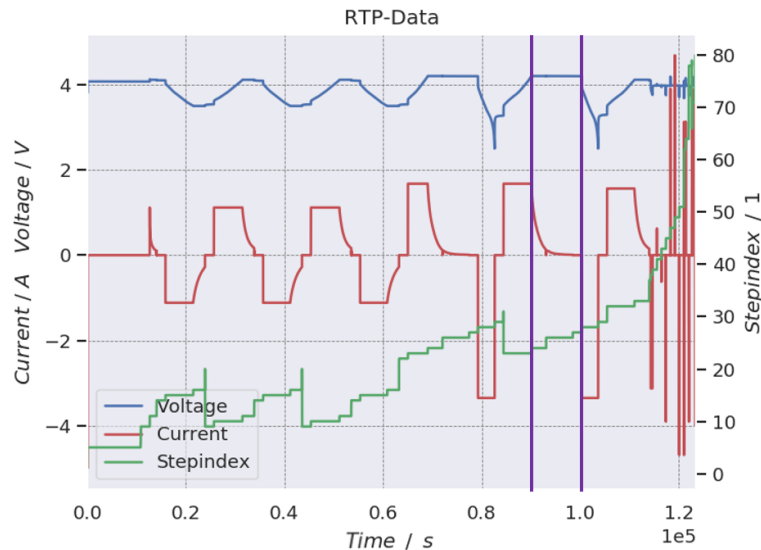


Figure 3.19: Shows partly data collected during execution of a RTP, **blue:** Terminal Voltage V , **red:** Current I , **green:** Stepindex n ; The vertical lines in **violet** mark the scope for the extraction of the data during the CV charging process.

Figure 3.20 shows an example set of current time series ($I - t$) extracted for a cell while being cycle aged. Each current time series ($I - t$) originates from a corresponding RTP. Again each colour corresponds to the degree of ageing and capacity fade respectively. Herein, brighter curves relate to less aged cell status. Therefore, the brightest curve originates from the completely unaged cell (first RTP) while the darkest curve relates to the last RTP of the ageing test and highest ageing respectively. It can be already seen that the shape of the charge current time series clearly varies with battery ageing.

3.4 Analysis of the Constant-Voltage Charging Phase

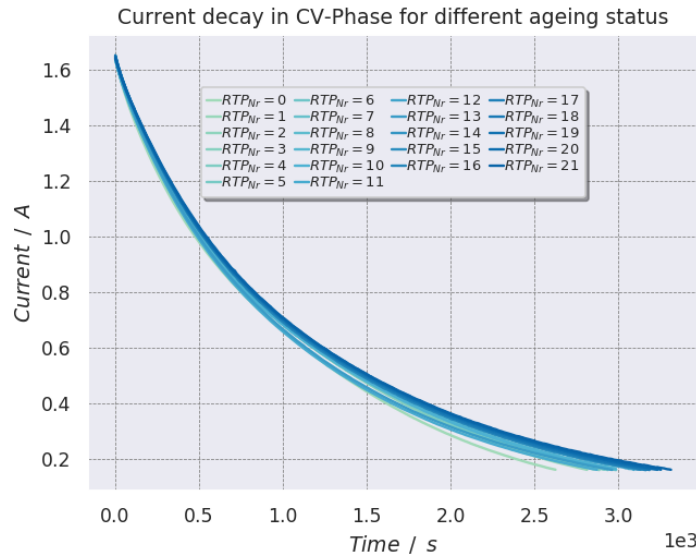


Figure 3.20: $I(t)$ during CV charging extracted from an ageing-dataset. Brighter curves represent less aged cell status.

3.4.2 Characterisation via Exponential Decay Function

In order to describe the dynamic behaviour of the charging current shown in Figure 3.20 the exponential decaying function,

$$I(t) = A \cdot \exp\left(-\frac{t}{\tau}\right), \quad (3.12)$$

is used. Here the parameter A is fixed and corresponds to the initial value of the charge current, which is given by its value during CC charging. The strength of the decay is described by the time constant τ . This function is fitted to the values of the data-points from the extracted charge current time series. For the non-linear least squares fitting, the python function `optimize.curve_fit` from the `scipy` module was used. An example for a result of this procedure can be seen in Figure 3.21. For better visibility only the data from the first and last RTP is shown.

3.4.3 Linear Regression of SoH versus Decay Constant

After extraction of the decay constants, a relationship between them and SoH of the cell should be found. With this, SoH can be easily estimated whenever a decay constant has been extracted. Figure 3.22 shows a scatter plot of the decay constant τ with respect to present SoH being calculated according to Equation 2.1. The present total

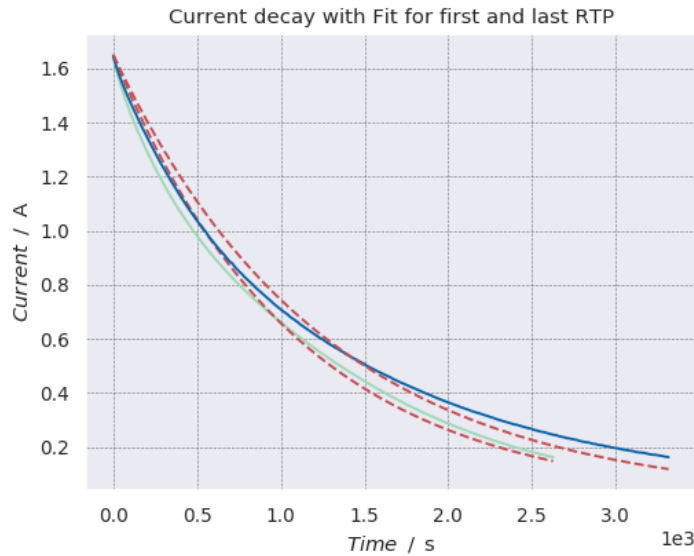


Figure 3.21: Fit of the charge current time series extracted from the first and last RTP of an ageing-dataset with exponential decay function. **bright green:** originates from the unaged cell (first RTP); **dark blue:** originates from the aged cell (last RTP); **red:** data generated by the obtained fit functions.

capacity of the cell was calculated by coulomb counting via current integration over a complete CC-CV charging process (Eq.3.9). For the quantitative description of τ versus SoH a linear least squares regression was performed using the python function `stats.linregress` from the `scipy` module. Here σ is the RMSE of residuals (calculated by Eq.3.10) and R^2 is the corresponding coefficient of determination (calculated by Eq.3.11). The defining parameters of the fit function are also shown in the textbox at the bottom left of the figure. The gradient of the regression line is described by k with its unit being ($\frac{\%}{s}$). The intercept with SoH-axis is given by the parameter d with its unit being (%). With the obtained function, the cell's SoH can be easily estimated after every CV charging process.

3.5 CV-Analysis: Implementation and Results

To test the CV-Analysis and gather information about its range of application, the method was applied to a variety of ageing-datasets. As for the ICA, these include datasets originating from calendric ageing tests, drive cycle ageing tests and cyclic ageing tests. The ageing-datasets were chosen according to their corresponding LP's defining parameters. The aim of this selection is to cover a wide range of possible ageing scenarios. For each chosen LP there are three cells which were aged under these

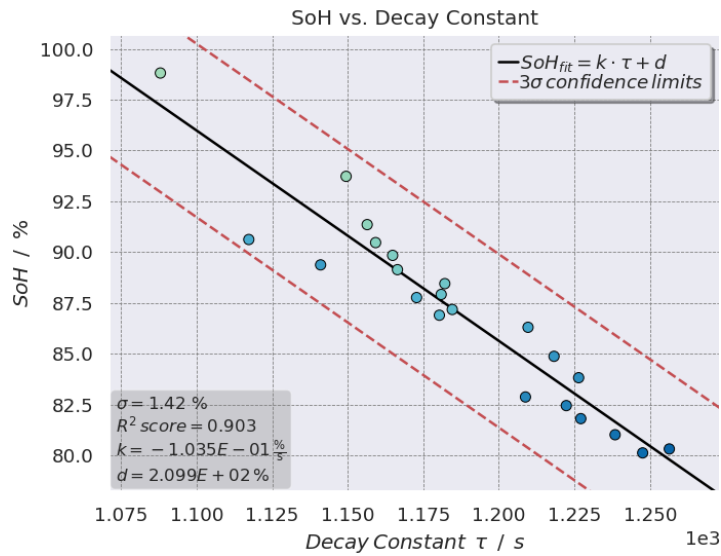


Figure 3.22: Example scatter plot of the decay constant τ versus SoH. Brighter dots refer to less aged cell status.

conditions. The selection of LPs as well as their defining parameters can be found in Section 3.3 (Tables 3.1 and Table 3.2). The corresponding results are described in the following subsections. An overview of the obtained results can be looked up in Table 3.3.

3.5.1 Drive Cycle Ageing

The scenario of drive cycle ageing gives insight on how applicable the used CV-Analysis is for estimating the SoH under real conditions. For the investigation of drive cycle ageing the cells were aged with a LP specified by an automotive partner of the Virtual Vehicle Research GmbH. Its duration is about one week and it aims to approximate the driving behaviour of a full-time employee with daily car use for job arrival and weekend use for outdoor pursuits. Due to legal reasons, we are not allowed to present any further information regarding this LP. Nevertheless, the gained results from investigating the CV charging processes from the drive cycle ageing tests are shown in Figure 3.23.

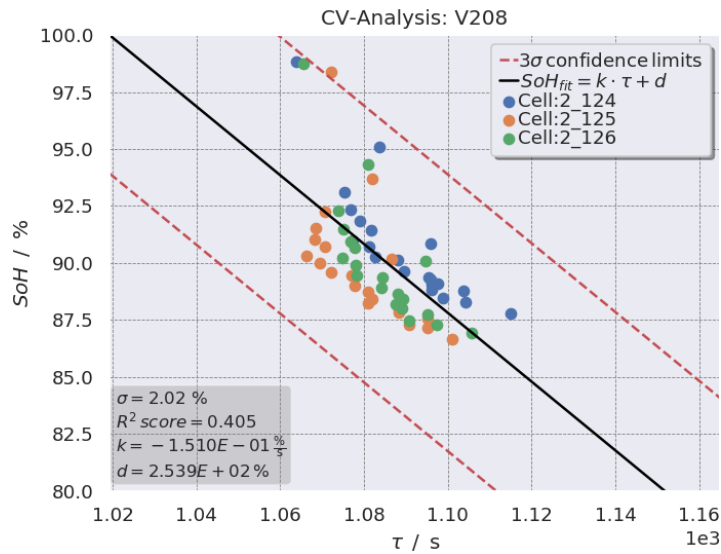


Figure 3.23: Scatter plot and linear regression of the decay constant τ versus SoH for cells being aged by the drive cycle V208.

3.5.2 Calendric Ageing

For the investigation of calendric ageing, six LPs were chosen to display the effects of:

- Different SoC during storage
- Different temperature during storage

The chosen LPs for calendric aged cells and their defining parameters can be found in Table 3.1 within Section 3.3.2.

Variation of SoC: The figures 3.24a and 3.24b display the effect of different SoC-level during calendric ageing under a temperature of $T = 45^\circ\text{C}$. In the case of L202 the cells were stored with $SoC = 15 \%$, whereas L206 corresponds to a SoC-level of $SoC = 95 \%$. As expected, the cells stored with a high SoC-level experienced more capacity fade. The values for σ show that the linear description of a cell's SoH versus decay constant τ is more accurate for the gentle ageing by L202. However, the data-points are more non-linearly spread out in the case of L202 leading to a lower R^2 score of 0.657. For the ageing by L206, the R^2 score of the linear regression reaches a value

3.5 CV-Analysis: Implementation and Results

of 0.952 which validates it as a descriptive model function.

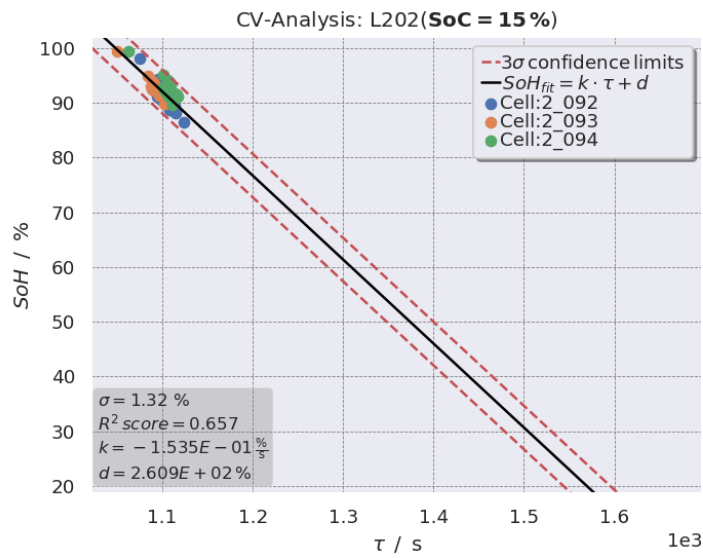


Figure 3.24a: Scatter plot of the decay constant τ versus SoH for cells being aged calendric by L202: $T = 45^\circ\text{C}$, SoC = 15 %

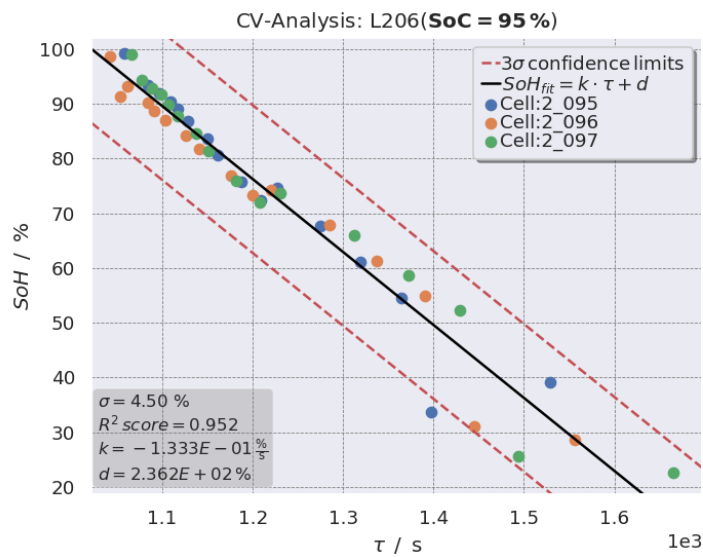


Figure 3.24b: Scatter plot of the decay constant τ versus SoH for cells being aged calendric by L206: $T = 45^\circ\text{C}$, SoC = 95 %

3 Ageing Data Analysis

The two figures 3.25a and 3.25b display the effect of different SoC-levels during calendric ageing under a temperature of $T = 0^\circ\text{C}$. In the case of L201 the cells were stored with $SoC = 15\%$, whereas L203 corresponds to $SoC = 55\%$.

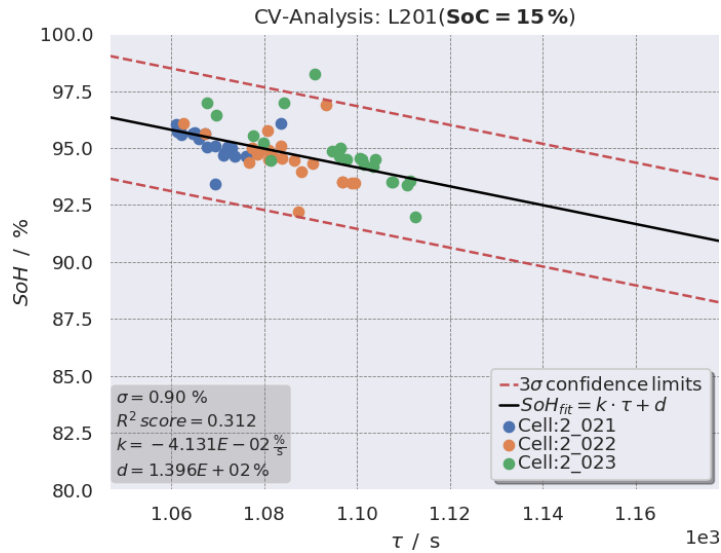


Figure 3.25a: Scatter plot of the decay constant τ versus SoH for cells being aged calendric by L201: $T = 0^\circ\text{C}$, $SoC = 15\%$

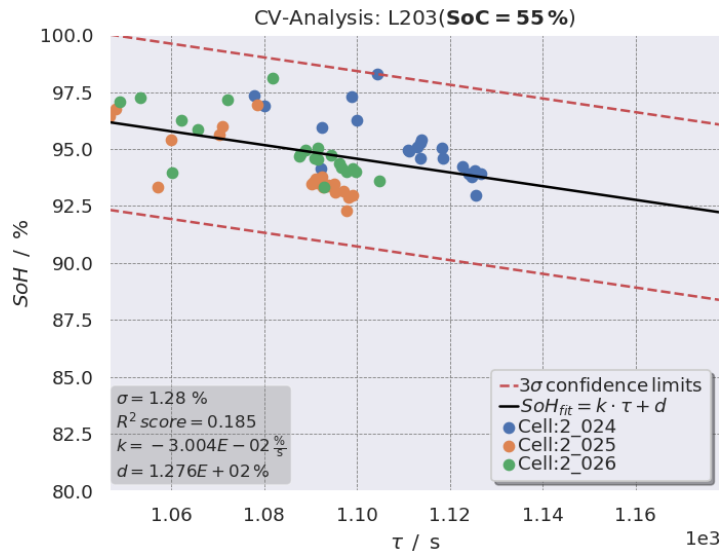


Figure 3.25b: Scatter plot of the decay constant τ versus SoH for cells being aged calendric by L203: $T = 0^\circ\text{C}$, $SoC = 55\%$

In both cases the cells experienced a decrease in SoH of less than 10%. In the case of L201 the linear regressions accuracy is quite high described by $\sigma = 0.90\%$. In the case

3.5 CV-Analysis: Implementation and Results

of a higher SoC-level during storage (L203) the scatters are more spread out leading to a lower accuracy of $\sigma = 1.28\%$ and a lower R^2 score.

Variation of Temperature: The hereafter figures 3.26a and 3.26b show the effect of different temperature during calendric ageing with $SoC = 15\%$. In the case of L201 the cells were stored with $T = 0^\circ\text{C}$, whereas L202 corresponds to a temperature of $T = 45^\circ\text{C}$.

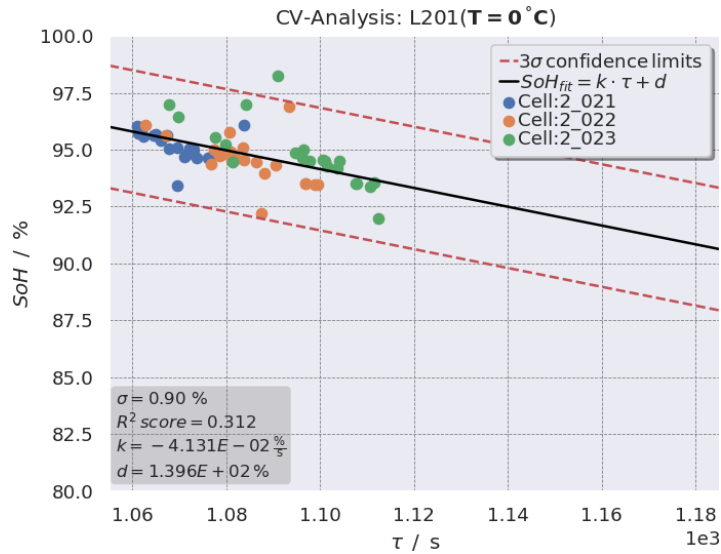


Figure 3.26a: Scatter plot of the decay constant τ versus SoH for cells being aged calendric by L201: $SoC = 15\%$, $T = 0^\circ\text{C}$

3 Ageing Data Analysis

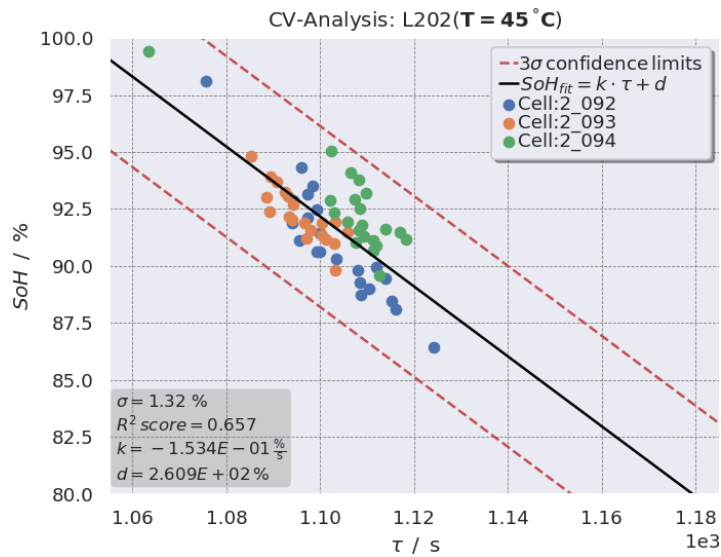


Figure 3.26b: Scatter plot of the decay constant τ versus SoH for cells being aged calendric by L202: SoC = 15 %, $T = 45 \text{ }^\circ\text{C}$

It can be seen that a higher storage temperature leads to more capacity fade and lower accuracy. A steeper slope of the linear regression can be seen for the higher temperature ageing by L202.

The figures 3.27a and 3.27b display the effect of different temperature during calendric ageing with SoC = 55 %. In the case of L203 the cells were stored with $T = 0 \text{ }^\circ\text{C}$, whereas L204 corresponds to a temperature of $T = 30 \text{ }^\circ\text{C}$.

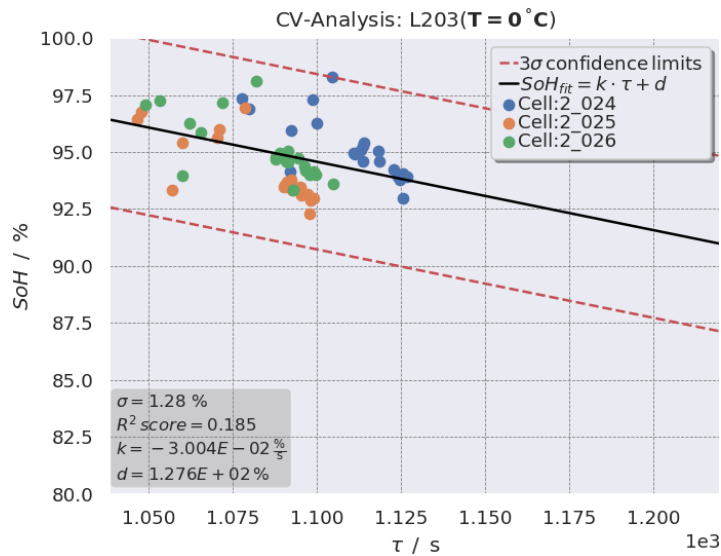


Figure 3.27a: Scatter plot of the decay constant τ versus SoH for cells being aged calendric by L203: SoC = 55 %, $T = 0 \text{ }^\circ\text{C}$

3.5 CV-Analysis: Implementation and Results

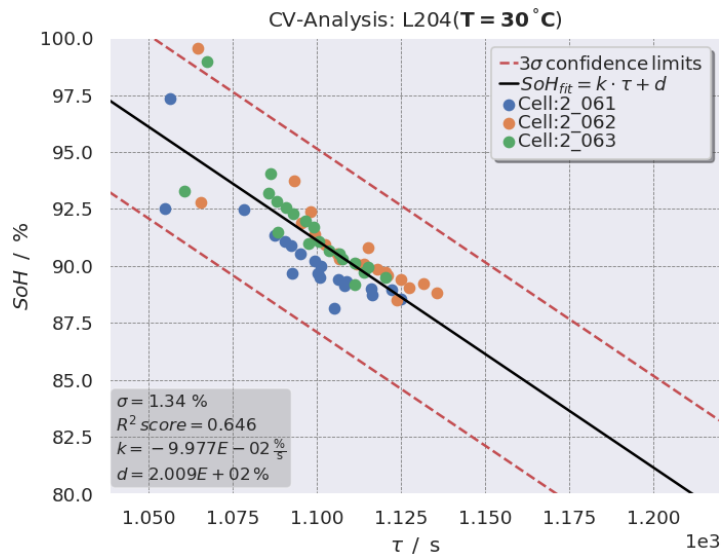


Figure 3.27b: Scatter plot of the decay constant τ versus SoH for cells being aged calendric by L204: SoC = 55 %, $T = 30^\circ C$

The scatter plots 3.28a and 3.28b illustrate the effect of different temperature during calendric ageing with SoC = 95 %. In the case of L205 the cells were stored with $T = 20^\circ C$, whereas L206 corresponds to a temperature of $T = 45^\circ C$. It can be seen that different storage temperature has a big influence on calendric cell ageing at a high SoC-level. As in the comparisons before, the linear regression shows higher σ and a steeper slope for the cells stored under higher temperature.

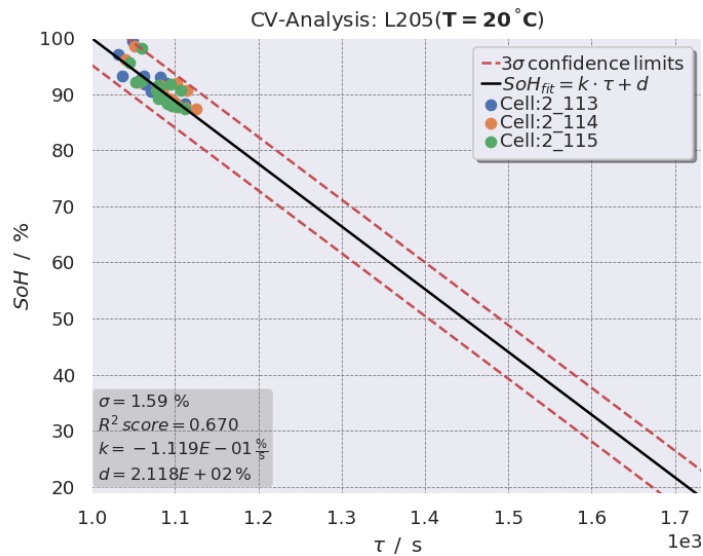


Figure 3.28a: Scatter plot of the decay constant τ versus SoH for cells being aged calendric by L205: SoC = 95 %, $T = 20^\circ C$

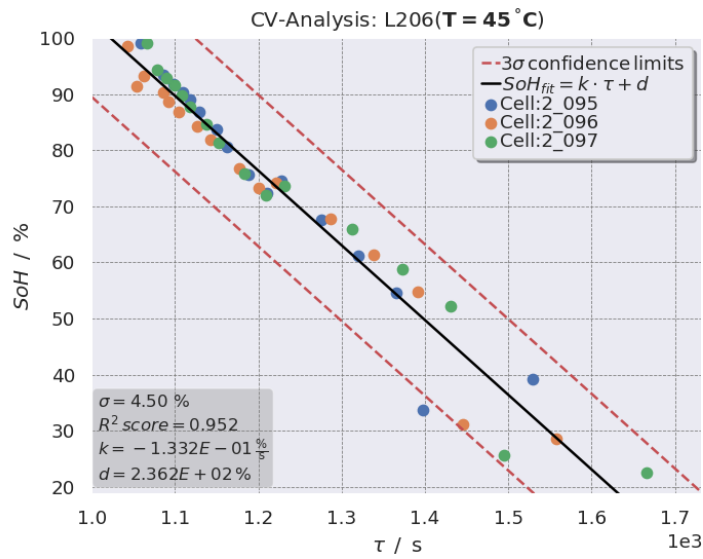


Figure 3.28b: Scatter plot of the decay constant τ versus SoH for cells being aged calendric by L206: SoC = 95 %, $T = 45 \text{ }^\circ\text{C}$

3.5.3 Cycle Ageing

For the CV-investigation of cycle ageing, four LPs were chosen to display the effects of:

- Different temperature during cycling
- Different dSoC during cycling

Table 3.2 in section 3.3.3 lists the chosen LPs for cyclic aged cells and their defining parameters:

Variation of Temperature: The two figures 3.29a and 3.29b display the effect of different temperature during cyclic ageing with $dSoC = 2.5 \%$. In the case of L208 the cells were cycled under a temperature of $T = 0 \text{ }^\circ\text{C}$, whereas L209 corresponds to $T = 45 \text{ }^\circ\text{C}$. As for calendric ageing, cells aged under a higher temperature show more

3.5 CV-Analysis: Implementation and Results

capacity fade, lower accuracy and a steeper slope.

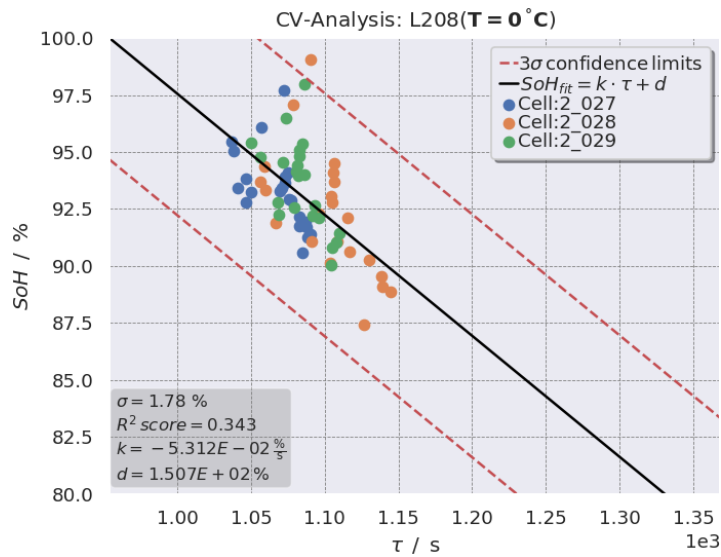


Figure 3.29a: Scatter plot of the decay constant τ versus SoH for cells being aged cyclically by L208: $dSoC = 2.5 \%$, $T = 0 \text{ }^\circ\text{C}$

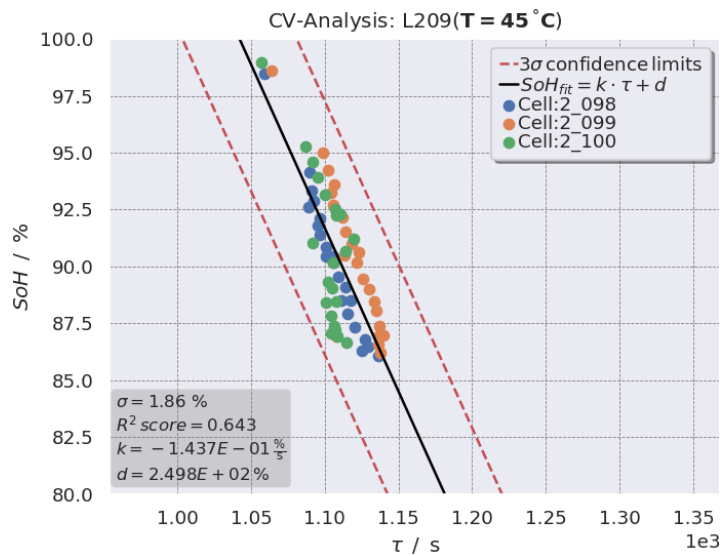


Figure 3.29b: Scatter plot of the decay constant τ versus SoH for cells being aged cyclically by L209: $dSoC = 2.5 \%$, $T = 45 \text{ }^\circ\text{C}$

The figures 3.30a and 3.30b display the effect of different temperature during cyclic ageing with $dSoC = 80 \%$. In the case of L215 the cells were cycled under a temperature of $T = 0 \text{ }^\circ\text{C}$, whereas L216 corresponds to $T = 45 \text{ }^\circ\text{C}$. Both regressions show high R^2 scores > 0.91 . It can be seen that different temperature has a big influence on cyclic

3 Ageing Data Analysis

cell ageing with high $dSoC$. Furthermore, higher temperature during cycling leads to lower accuracy (higher σ) and a steeper slope.

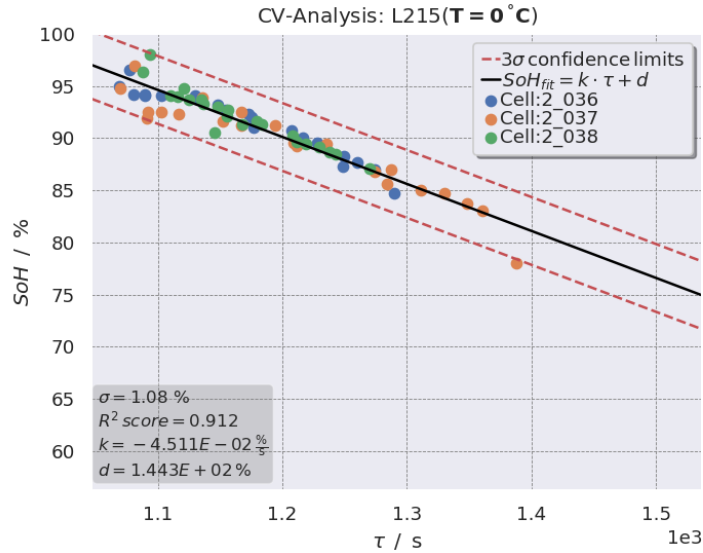


Figure 3.30a: Scatter plot of the decay constant τ versus SoH for cells being aged cyclic by L215: $dSoC = 80\%$, $T = 0^\circ\text{C}$

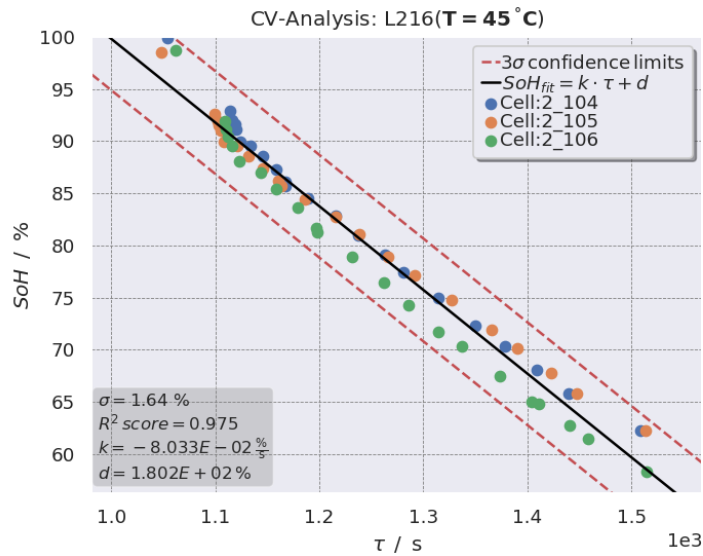


Figure 3.30b: Scatter plot of the decay constant τ versus SoH for cells being aged cyclic by L216: $dSoC = 80\%$, $T = 45^\circ\text{C}$

Variation of $dSoC$: The following figures 3.31a and 3.31b illustrate the effect of different $dSoC$ during cyclic ageing under a temperature of $T = 45^\circ\text{C}$. In the case of L209 the cells were cycled with $dSoC = 2.5\%$, whereas L216 corresponds to

3.5 CV-Analysis: Implementation and Results

$dSoC = 80\%$. As expected, the cells which were cycled with high $dSoC$ experienced more capacity fade. Nevertheless, the accuracy of both regressions is very similar.

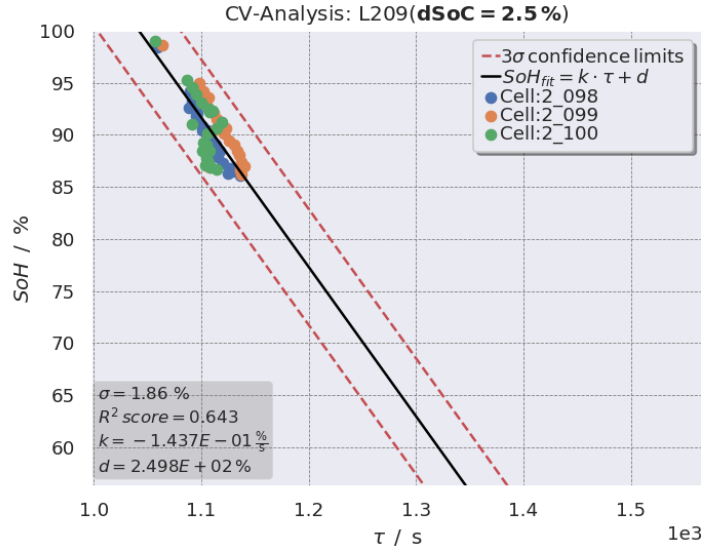


Figure 3.31a: Scatter plot of the decay constant τ versus SoH for cells being aged cyclic by L209: $T = 45^\circ C$, $dSoC = 2.5\%$

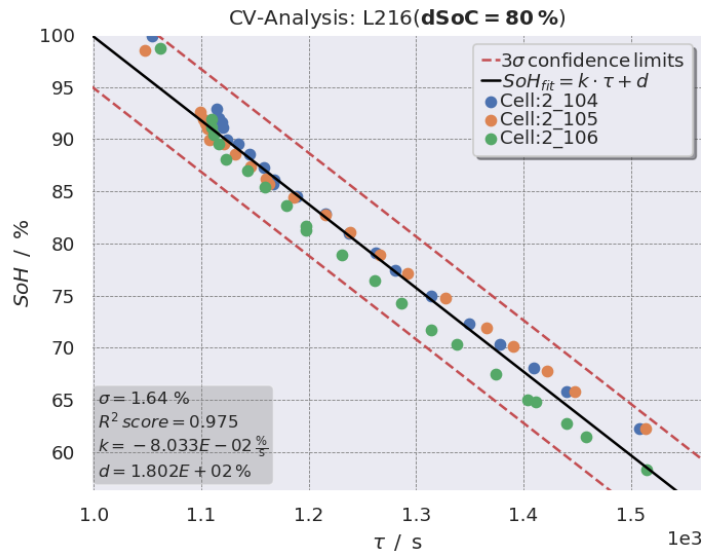


Figure 3.31b: Scatter plot of the decay constant τ versus SoH for cells being aged cyclic by L216: $T = 45^\circ C$, $dSoC = 80\%$

3 Ageing Data Analysis

The following table comprehensively lists the results obtained by ICA and CV-Analysis. Here k_{ICA} and k_{CV} describe the slope of the linear regressions obtained through ICA and CV-Analysis. The quantities d_{ICA} and d_{CV} describe the intercept of the corresponding regression lines with the SoH-axis.

Table 3.3: Results of Ageing Data Analysis

Ageing Type	Constant	Variable	σ_{ICA} [%]	σ_{CV} [%]	R_{ICA}^2	R_{CV}^2	$k_{ICA} [\frac{\%}{\%}]$	$k_{CV} [\frac{\%}{\%}]$	d_{ICA} [%]	d_{CV} [%]
Drive Cycle	-	-	1.01	2.02	0.837	0.405	-5.07e2	-1.51e-1	1.99e3	2.54e2
Calendaric	$T = 45^\circ\text{C}$	$SoC = 15\%$	0.76	1.32	0.881	0.657	-1.47e2	-1.54e-1	6.49e2	2.61e2
		$SoC = 95\%$	3.02	4.50	0.943	0.952	-3.92e2	-1.33e-1	1.56e3	2.36e2
	$T = 0^\circ\text{C}$	$SoC = 15\%$	0.76	0.90	0.481	0.312	-1.23e2	-4.13e-2	5.58e2	1.40e2
		$SoC = 55\%$	1.18	1.28	0.306	0.185	-1.18e2	-3.00e-2	5.39e3	1.28e2
	$SoC = 15\%$	$T = 0^\circ\text{C}$	0.76	0.90	0.481	0.312	-1.23e2	-4.13e-2	5.58e2	1.40e2
		$T = 45^\circ\text{C}$	0.76	1.32	0.881	0.657	-1.47e2	-1.53e-1	6.49e2	2.61e2
	$SoC = 55\%$	$T = 0^\circ\text{C}$	1.18	1.28	0.306	0.185	-1.18e2	-3.00e-2	5.39e2	1.28e2
		$T = 30^\circ\text{C}$	1.16	1.34	0.719	0.646	-1.55e2	-9.98e-2	6.76e2	2.01e2
$SoC = 95\%$	$T = 20^\circ\text{C}$	1.04	1.59	0.856	0.670	-4.39e2	-1.12e-1	1.74e3	2.12e2	
	$T = 45^\circ\text{C}$	3.02	4.50	0.943	0.952	-3.92e2	-1.33e-1	1.56e3	2.36e2	
Cyclic	$dSoC = 2.5\%$	$T = 0^\circ\text{C}$	1.84	1.78	0.000	0.343	-4.16e1	-5.31e-2	2.49e2	1.51e2
		$T = 45^\circ\text{C}$	0.73	1.86	0.930	0.643	-1.71e2	-1.44e-1	7.38e2	2.50e2
	$dSoC = 80\%$	$T = 0^\circ\text{C}$	1.32	1.08	0.869	0.912	-1.29e2	-4.51e-2	5.79e2	1.44e2
		$T = 45^\circ\text{C}$	1.67	1.64	0.942	0.975	-1.89e2	-8.03e-2	8.05e2	1.80e2
	$T = 45^\circ\text{C}$	$dSoC = 2.5\%$	0.76	1.86	0.923	0.643	-1.65e2	-1.44e-1	7.14e2	2.50e2
		$dSoC = 80\%$	1.67	1.64	0.942	0.975	-1.89e2	-8.03e-2	8.05e2	1.80e2

3.6 Discussion on Ageing Data Analysis

In this section, the results obtained by the applied methods for Ageing Data Analysis are summarized and discussed.

Drive Cycle Ageing: The from ICA derived linear regression shown in Figure 3.9 has a coefficient of determination of $R^2 = 0.837$ and is able to describe the cells SoH with an accuracy of $\sigma = 1.01\%$. In contrast, the regression derived from analysing the CV charging process (Figure 3.23) has a coefficient of determination of $R^2 = 0.405$ and is able to describe the cells SoH only with an accuracy of $\sigma = 2.02\%$. As a result, for the investigated drive cycle ageing a higher performance of the ICA-method is clearly noticeable. With three-sigma bounds of about $\pm 3.0\%$ the ICA would be quite useable as a tool for estimating a Li-ion cell's SoH. Nevertheless, a dependence of the derived linear regressions defining parameters on the drive cycle conditions is expected.

Calendric Ageing: As for drive cycle ageing, the ICA-method shows superior performance accounted for by lower σ -values and equal or higher values for the coefficients of determination R^2 .

For both methods a high SoC-level during storage leads to lower accuracy or higher σ -values respectively. This effect is more dominant for higher storage temperature and is shown by the figures 3.10a & 3.10b or 3.24a & 3.24b.

The variation of temperature for several SoC-levels shows that ICA is more robust against varying temperature. This is manifested by the results at $SoC = 15\%$ and $SoC = 55\%$ (figures 3.12a & 3.12b) which show independence of the accuracy σ on different storage temperatures. In contrast, the relative CV-results (figures 3.26a & 3.26b) show that higher storage temperature leads to less accurate results. At the highest investigated SoC-level of $SoC = 95\%$, increasing temperature leads to lower accuracy for both the ICA and CV-Analysis.

For the results gained through CV-Analysis, a further temperature dependence is noticeable. The slope of the linear regressions gets steeper as the temperature rises. This effect can be seen in the figure pairs 3.26a & 3.26b, 3.27a & 3.27b and 3.28a & 3.28b. Because of the limited amount of ageing-datasets it is hard to derive quantified generally valid statements regarding the effects of varying temperature or SoC-levels respectively.

Cycle Ageing: In the case of cycle ageing the ICA-method shows a slightly better performance accounted for by lower average σ -value and similar or higher values for the coefficients of determination R^2 .

3 Ageing Data Analysis

However, at a low $dSoC = 2.5\%$ combined with a low temperature $T = 0^\circ\text{C}$ the ICA-method gets unstable. This can be explained by Figure 3.32 which displays the smoothed IC-curves corresponding to Figure 3.15a. It is noticeable that due to ageing at the aforementioned conditions, the second local maxima from the right side, which lies in a voltage range of $(3.7 - 3.8)\text{V}$, tends to vanish while the third local maxima from the right side tends to grow and gets more dominant.

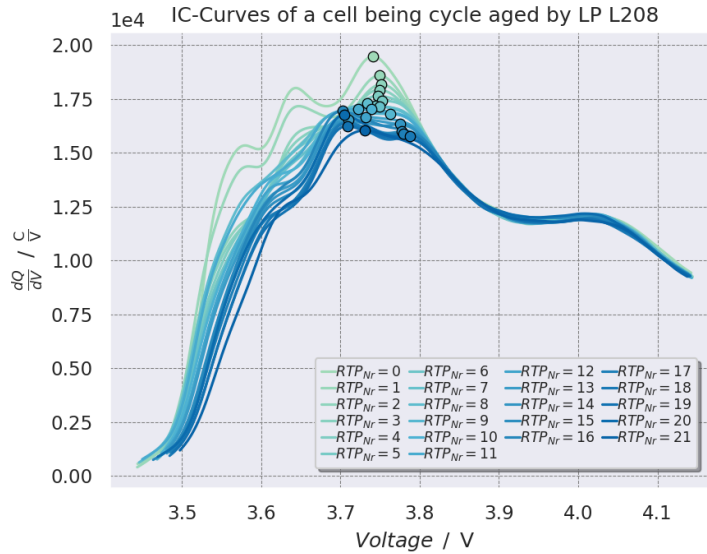


Figure 3.32: Smoothed IC-curves corresponding to Figure 3.15a. The figure shows the vanishing of the second local maxima from the right side which lies in a voltage range of $(3.7 - 3.8)\text{V}$, while the third local maxima from the right side tends to get more prominent with increased ageing.

For the results gained through CV-Analysis the slope of the linear regressions gets steeper with increasing temperature. This effect is displayed by the figure pairs 3.29a & 3.29b and 3.30a & 3.30b. As in the case of calendric ageing, due to the limited amount of ageing-datasets it is not possible to derive a quantified description of this effect.

To conclude, ICA is overall more accurate in describing a cell's SoH. In order to apply the method, data of the CC charging process is needed. For the investigated cell-type, the extracted FPs are located within a voltage range of $(3.7 - 3.8)\text{V}$, which corresponds to a SoC of around $(40 - 60)\%$. Therefore, the cell needs not to perform a full charge/discharge cycle in order to extract the wanted FP and its location. An advantage of the CV-method is that it can be applied to every full CV charging process. Therefore, it is independent of initial SoC as long as CV charging is executed. As a result CV-Analysis is less invasive in estimating a cell's SoH.

From these results it can be deduced that the performance of both methods decreases

3.6 Discussion on Ageing Data Analysis

with increasingly radical ageing. Since the applied methods seem highly dependent on the cell's operation conditions, they are only applicable for scenarios where these are known exactly beforehand and ageing tests have been carried out to extract the corresponding linear regression. This discards them as on-board capacity estimation methods for EVs and HEVs as these have to operate under a wide range of conditions specified by varying temperatures, current rates and SoC-levels.

4

Total Capacity Estimation via Approximate Total Least Squares

In this chapter an optimization method for on-board capacity estimation is investigated. After a detailed description of the method it is applied to measurement data to validate its performance. The method being used is based on the work of Plett (2011). Because of the definition of SoH via capacity fade, the importance of accurate estimates for a cell's actual total capacity Q_{tot} is obvious. A majority of capacity estimation methods is based on the following equation which directly follows from the definition of SoC and coulomb counting.

$$\underbrace{\int_{t_1}^{t_2} \frac{\eta I(t)}{3600} dt}_y = Q_{tot} \underbrace{(SoC(t_2) - SoC(t_1))}_x. \quad (4.1)$$

Here, $SoC(t)$ is the cell's SoC at time t . Q_{tot} is the actual total capacity in (Ah), $I(t)$ is the electric current in (Ah) and η is the coulombic current efficiency, a unitless efficiency factor which describes the magnitude of lost charge by side reactions occurring during charge or discharge. For the purpose of this investigation we assume a constant $\eta \approx 1$. The time t is measured in seconds. To convert the summed current to the right unit, it is multiplied by the factor $1/3600$. Within the framework of this investigation, current is considered to have a positive sign while charging and to have a negative sign while discharging. As a further assumption, the total cell capacity Q_{tot} is considered to be independent of temperature and C-rate. The estimates for the cell's SoC are needed as inputs and can originate from any SoC estimation method with the constraint that it must not depend on the cell's total capacity to prevent circularity of dependencies. In this work two SoC estimation methods will be used to generate the x values. Firstly, a

4 Total Capacity Estimation via Approximate Total Least Squares

simple voltage-based estimation will be made via the OCV-SoC estimation method as described in 2.3.2. Secondly, a more sophisticated SoC estimation will be made with an Extended Kalman Filter (EKF) which brings several advantages we will discuss later. For the generation of the y input coulomb counting via numerical current integration will be used.

By looking at the horizontal braces of Equation 4.1, which are labelled as " y " and " x ", the linear structure of the capacity estimation problem $y = Q_{tot} \cdot x$ is brought to mind. The standard approach for solving optimization problems of this kind is to use standard least square linear regression techniques. These methods consider the optimization problem in finding a solution to an equation of the form $(y \pm \Delta y) = Q_{tot} \cdot x$ which assumes that there is no measurement noise on the variable x . Since the variable x relates to a change in SoC, it should also be considered to have some kind of error as the values for $SoC(t_1)$ and $SoC(t_2)$ are estimates. As a result, our optimization problem is defined by an equation of the form:

$$(y \pm \Delta y) = Q_{tot} \cdot (x \pm \Delta x) \quad (4.2)$$

The standard approach to circumvent this issue is to minimize the error of x as much as possible and then apply standard least square linear regression. One way of achieving this could be putting constraints on how the values for the cell's SoC are estimated. A possibility would be to force the charge/discharge current to be zero until the cell is near equilibrium and therefore terminal voltage has relaxed close to its OCV-value. Then the SoC could be directly extracted from the OCV-SoC lookup table. Nevertheless, this approach ignores the residual error in x . Furthermore, it is highly invasive as it imposes strict constraints on the cell current during estimation. Therefore, other optimization methods which are non-invasive and consider the noise in both the x and y variables may be used.

The most rigorous approach for solving a linear regression problem like this would be to consider it in terms of Bayesian probability theory. Under the assumption of normal Gaussian errors and an assumed specific prior distribution of the parameter, Bayesian Straight Line Regression (SLR) yields an exact solution of the posterior probability for the parameter Q_{tot} . With this information the parameter as well as its uncertainty can be estimated by the mean posterior probability and its corresponding variance, respectively. Hereinafter, the method is briefly introduced. A detailed description of linear regression based on Bayesian probability theory is presented by Von der Linden

et al. (2014).

Given the data pairs (x_i, y_i) with errors in both variables $(\sigma_{x,i}, \sigma_{y,i})$, the posterior probability for the parameter a of a straight line

$$y = ax \quad (4.3)$$

is given by ¹

$$p(a|\{x_i\}, \{y_i\}, \{\sigma_{x,i}\}, \{\sigma_{y,i}\}) = \frac{\rho(a|\{x_i\}, \{y_i\}, \{\sigma_{x,i}\}, \{\sigma_{y,i}\})}{Z} \quad (4.4)$$

$$\rho(a|\{x_i\}, \{y_i\}, \{\sigma_{x,i}\}, \{\sigma_{y,i}\}) = \frac{1}{(1+a^2)^{3/2}} \exp\left(-\frac{1}{2} \sum_i \frac{(y_i - ax_i)^2}{\sigma_{y,i}^2 + a^2 \sigma_{x,i}^2}\right), \quad (4.5)$$

Where Z is the normalization that needs to be determined numerically by

$$Z = \int_{-\infty}^{\infty} \rho(a|\{x_i\}, \{y_i\}, \sigma_{x,i}, \sigma_{y,i}) da. \quad (4.6)$$

The parameter a can be estimated by the mean posterior probability

$$\langle a \rangle = \int a p(a|\{x_i\}, \{y_i\}, \sigma_{x,i}, \sigma_{y,i}) da \quad (4.7)$$

and the uncertainty from the corresponding variance

$$\langle (\Delta a)^2 \rangle = \int (\Delta a)^2 p(a|\{x_i\}, \{y_i\}, \sigma_{x,i}, \sigma_{y,i}) da. \quad (4.8)$$

Both expressions need to be computed numerically.

Iterative update: To avoid the storage of all data values, the computation can be done iteratively. To this end and also for numerical stability, it is expedient to use the logarithmic representation of the posterior probability density function (PDF). We define

$$L_N(a) = \ln(\rho(a|\{x_i\}, \{y_i\}, \{\sigma_{x,i}\}, \{\sigma_{y,i}\})) \quad (4.9)$$

$$= -\frac{3}{2} \ln(1+a^2) - \frac{1}{2} \sum_{i=1}^N \frac{(y_i - ax_i)^2}{\sigma_{y,i}^2 + a^2 \sigma_{x,i}^2}. \quad (4.10)$$

¹Bayesian Probability Theory: Applications in the Physical Sciences, W. von der Linden, V. Dose, U. von Toussaint, Cambridge University Press, 2014

4 Total Capacity Estimation via Approximate Total Least Squares

Every time a new data point (x_{N+1}, y_{N+1}) is added, we obtain

$$L_{N+1}(a) = L_N - \frac{1}{2} \frac{(y_{N+1} - ax_{N+1})^2}{\sigma_{y,N+1}^2 + a^2 \sigma_{x,N+1}^2}.$$

Hence, L_N can be computed iteratively for a set of parameter values $\{a_i\}$. From those values the normalization, mean and variance can be numerically evaluated. Because the idea to consider Bayesian SLR in the context of on-board capacity estimation arose towards the end of this work, it is not investigated in detail within this thesis. Nevertheless, it was tested for one dataset to compare it with the investigated methods. The result of this test can be seen in Figure 4.11.

In contrast to Bayesian SLR, the methods investigated in this thesis are based on linear least squares optimization. In order to find the solution to the problem described via Equation 4.2, a sophisticated variation of Total Least Squares (TLS) regression will be used in this chapter. Firstly the Weighted Least Squares (WLS) and Weighted Total Least Squares (WTLS) solutions will be derived. Afterwards the computationally more efficient Approximate Weighted Total Least Squares (AWTLS) regression technique for the on-board use is presented. Finally, the AWTLS algorithm is applied to real measurement data for validation.

4.1 From Weighted Least Squares to Weighted Total Least Squares

4.1.1 Weighted Least Squares

The aim of both the Least Squares (LS) and TLS methods is to find a constant \hat{Q} which describes $\vec{y} \approx \hat{Q} \cdot \vec{x}$ most accurately. The N-dimensional vector \vec{y} contains the summed current and \vec{x} holds the cell's SoC-change during each time interval. So the i-th component of these input vectors correspond to:

$$x_i = SoC(t_{i_2}) - SoC(t_{i_1}), \quad (4.11)$$

$$y_i = \int_{t_{i_1}}^{t_{i_2}} \frac{\eta(t) I(t)}{3600} dt, \quad (4.12)$$

where the vectors \vec{x} and \vec{y} must be at least one samples long ($N \geq 1$). As mentioned before, the WLS does not consider noisy values for x_i and therefore models the

4.1 From Weighted Least Squares to Weighted Total Least Squares

optimization problem as $\vec{y} - \vec{\Delta y} = Q \cdot \vec{x}$. The vector $\vec{\Delta y}$ is assumed to be of zero-mean Gaussian random nature. Its elements are considered as cumulated noise errors of the used current sensor. In practice $\vec{\Delta y}$ may additionally include gain errors, bias errors and non-linear errors which would bias all least squares based methods. According to Plett (2011), it can be assumed that gain errors and non-linear errors are negligible if the same current sensor is used for total capacity estimation and pack operation monitoring. Bias errors of the current sensor could be remedied by matching the discharged ampere hours with the charged ampere hours.

The aim of WLS is to find the best estimate \hat{Q} which minimizes the sum of squared errors. In order to achieve that, the WLS cost function 4.13 has to be minimized:

$$\chi_{WLS}^2 = \sum_{i=1}^N \frac{(y_i - Y_i)^2}{\sigma_{y_i}^2} = \sum_{i=1}^N \frac{(y_i - \hat{Q}x_i)^2}{\sigma_{y_i}^2}. \quad (4.13)$$

where Y_i means a point on the line $Y_i = \hat{Q} \cdot x_i$. In order to find the minimum of Equation 4.13, we set the partial derivative with respect to \hat{Q} to zero and solve for \hat{Q} .

$$\begin{aligned} \frac{\partial \chi_{WLS}^2}{\partial \hat{Q}} &= -2 \sum_{i=1}^N \frac{x_i (y_i - \hat{Q}x_i)^2}{\sigma_{y_i}^2} \stackrel{!}{=} 0 \\ \hat{Q} \sum_{i=1}^N \frac{x_i^2}{\sigma_{y_i}^2} &= \sum_{i=1}^N \frac{x_i y_i}{\sigma_{y_i}^2} \\ \hat{Q} &= \frac{\sum_{i=1}^N x_i y_i / \sigma_{y_i}^2}{\sum_{i=1}^N x_i^2 / \sigma_{y_i}^2}. \end{aligned} \quad (4.14)$$

As one can imagine, in real applications the length of the input vectors \vec{x} and \vec{y} increases every sample-timestep when a new measurement for the charge current and a new estimator for the cell's SoC is available. Therefore, we introduce the index n which describes the present length of the input vectors. With the definition of the two quantities,

$$c_{1,n} = \sum_{i=1}^n \frac{x_i^2}{\sigma_{y_i}^2} \quad \text{and} \quad c_{2,n} = \sum_{i=1}^n \frac{x_i y_i}{\sigma_{y_i}^2}, \quad (4.15)$$

we can express the present estimate for the total capacity as $\hat{Q}_n = c_{2,n}/c_{1,n}$. In order to achieve recursive calculation of the estimate \hat{Q} , we write $c_{1,n}$ and $c_{2,n}$ as recursively computing sums:

$$\begin{aligned} c_{1,n} &= c_{1,n-1} + \frac{x_n^2}{\sigma_{y_n}^2} \\ c_{2,n} &= c_{2,n-1} + \frac{x_n y_n}{\sigma_{y_n}^2} \end{aligned}$$

4 Total Capacity Estimation via Approximate Total Least Squares

To be able to calculate \hat{Q} recursively, initial values $c_{1,n=0}$ and $c_{2,n=0}$ are needed. For this purpose we pretend an artificial initial measurement where we set $x_0 = 1$ and $y_0 = Q_{nom}$. For the variance $\sigma_{y_0}^2$ the variance of the nominal capacity given by the cell manufacturer is used. The following variances $\sigma_{y_i}^2$ are considered as accumulated measurement noise from the used current sensor.

As the cell's total capacity fades with ongoing lifetime, the algorithm has to adapt to this true change in Q_{tot} . Therefore, fading memory of past measurements via a forgetting factor γ is easily implemented to obtain the Fading Memory Weighted Least Squares (FMWLS) cost function as described by Equation 4.16. The forgetting factor γ modifies the cost function in a way that puts more emphasis on recently gathered data. This can be seen as an alteration of the variances $\sigma_{y_i}^2$ which still allows for the use statistical hypothesis testing subsequently.

$$\chi_{FMWLS}^2 = \sum_{i=1}^N \gamma^{N-i} \frac{(y_i - \hat{Q}x_i)^2}{\sigma_{y_i}^2}, \quad 0 \ll \gamma \leq 1 \quad (4.16)$$

The introduction of the forgetting factor also leads to slightly changed sums $\tilde{c}_{1,n}$ and $\tilde{c}_{2,n}$:

$$\tilde{c}_{1,n} = \sum_{i=1}^n \gamma^{n-i} \frac{x_i^2}{\sigma_{y_i}^2}, \quad \text{and} \quad \tilde{c}_{2,n} = \sum_{i=1}^n \gamma^{n-i} \frac{x_i y_i}{\sigma_{y_i}^2}, \quad (4.17)$$

and therefore:

$$\begin{aligned} \tilde{c}_{1,n} &= \gamma \tilde{c}_{1,n-1} + \frac{x_n^2}{\sigma_{y_n}^2} \\ \tilde{c}_{2,n} &= \gamma \tilde{c}_{2,n-1} + \frac{x_n y_n}{\sigma_{y_n}^2}. \end{aligned}$$

Finally, the Fading Memory Least Squares (FMLS) solution for \hat{Q} can be calculated recursively according to:

$$\hat{Q}_n = \frac{\tilde{c}_{2,n}}{\tilde{c}_{1,n}} \quad (4.18)$$

With WLS and FMWLS we have two regression methods which have some nice properties. Firstly they give a closed-form solution for the estimate \hat{Q} . No more sophisticated methods are needed which leads to computational high efficiency. Furthermore, it is easily possible to calculate \hat{Q} recursively and to implement fading memory of past measurements, which additionally makes it lean in performance requirements and therefore suitable for embedded applications. Nevertheless, the ignoring of the errors in \vec{x} leads us to the derivation of the WTLS method.

4.1.2 Derivation of Weighted Total Least Squares

The WTLS-method models the optimization problem as $(\vec{y} \pm \Delta\vec{y}) = Q_{tot} \cdot (\vec{x} \pm \Delta\vec{x})$. Here, the components of $\Delta\vec{y}$ are assumed to be of zero-mean Gaussian random nature with the related standard deviations of $\vec{\sigma}_y$. Likewise, the components of $\Delta\vec{x}$ are assumed to be zero-mean Gaussian random with the standard deviations $\vec{\sigma}_x$. As previously mentioned, the approach of WTLS is to find the best value for the estimate \hat{Q} which minimizes the weighted sum of both, squared errors in x and y , by minimizing the corresponding WTLS cost function:

$$\chi_{WTLS}^2 = \sum_{i=1}^N \frac{(x_i - X_i)^2}{\sigma_{x_i}^2} + \frac{(y_i - Y_i)^2}{\sigma_{y_i}^2}, \quad (4.19)$$

where X_i and Y_i are the true coordinates of the i -th datapoint laying on the line $Y_i = \hat{Q} \cdot X_i$. These correspond to the noisy measurement data tuple (x_i, y_i) . To find the minimum of Equation 4.19, a different approach than in case of the WLS cost function has to be used. Since this is an optimization problem in two variables we use the method of Lagrange-multipliers. Hence, we augment the cost function with the constraint $Y_i - \hat{Q} \cdot X_i \stackrel{!}{=} 0$ to convert it. Then we can apply the derivative test like for an unconstrained problem. The augmented WTLS cost function is given by:

$$\chi_{WTLSaug}^2 = \sum_{i=1}^N \frac{(x_i - X_i)^2}{\sigma_{x_i}^2} + \frac{(y_i - Y_i)^2}{\sigma_{y_i}^2} - \lambda_i \cdot (Y_i - \hat{Q}X_i). \quad (4.20)$$

To find the local minima of the cost function, the partial derivatives $\partial\chi_{WTLSaug}^2/\partial X_i = \partial\chi_{WTLSaug}^2/\partial Y_i = \partial\chi_{WTLSaug}^2/\partial\lambda_i \stackrel{!}{=} 0$ are set zero which leads us to the following expressions for X_i and Y_i :

$$X_i = \frac{x_i\sigma_{y_i}^2 + \hat{Q}y_i\sigma_{x_i}^2}{\sigma_{y_i}^2 + \hat{Q}^2\sigma_{x_i}^2} \quad \text{and} \quad Y_i = \hat{Q}X_i. \quad (4.21)$$

By setting in these expressions, the cost function can be rewritten in terms of known quantities:

$$\chi_{WTLS}^2 = \sum_{i=1}^N \frac{(y_i - \hat{Q}X_i)^2}{\hat{Q}^2\sigma_{x_i}^2 + \sigma_{y_i}^2}. \quad (4.22)$$

To put more emphasis on recently gathered data, we introduce the forgetting memory factor γ which leads us to:

4 Total Capacity Estimation via Approximate Total Least Squares

$$\chi_{WTLS}^2 = \sum_{i=1}^N \gamma^{N-i} \frac{(y_i - \hat{Q}X_i)^2}{\hat{Q}^2\sigma_{x_i}^2 + \sigma_{y_i}^2}, \quad 0 \ll \gamma \leq 1 \quad (4.23)$$

Now having the cost function in a suitable form we find the minimum by setting its partial derivative with respect to the estimator \hat{Q} to zero:

$$\frac{\partial \chi_{WTLS}^2}{\partial \hat{Q}} = 2 \sum_{i=1}^N \gamma^{N-i} \frac{(\hat{Q}x_i - y_i)(\hat{Q}y_i\sigma_{x_i}^2 + x_i\sigma_{y_i}^2)}{\hat{Q}^2\sigma_{x_i}^2 + \sigma_{y_i}^2} \stackrel{!}{=} 0. \quad (4.24)$$

Unfortunately, the WTLS-solution for \hat{Q} has some disadvantages: First of all, Equation 4.24 cannot be resolved explicitly to \hat{Q} . Therefore, a root finding algorithm like the Newton-Raphson search is necessary to find a value for the estimator. This leads to higher computational effort since the root finding algorithm works in an iterative manner and has to be performed after every update of the data vectors \vec{x} and \vec{y} .

Another drawback of WTLS is the lack of recursive computation which leads to storage difficulties because the entire data vectors have to be stored. As the number of measurements N increases, so does the number of computations which additionally makes WTLS unsuitable for on-board applications because of limited processing power. Motivated by these restrictions an elaborate algorithm which gives a closed-form solution for \hat{Q} and features a recursive computation manner will be presented in Section 4.4.

4.2 Confidence Intervals

As for any estimation method, it is important to be able to make a statement regarding its precision. Therefore, we need a method to specify the uncertainty of the estimator \hat{Q} . One way to describe the dispersion of a variable from its mean value is by its variance $\sigma_{\hat{Q}}^2$ through which confidence intervals can be specified.

To obtain a value for the variance $\sigma_{\hat{Q}}^2$, we consider the problem as a maximum-likelihood (ML) optimization problem. With the assumption that all the measurement errors held in $\vec{\Delta x}$ and $\vec{\Delta y}$ are uncorrelated and Gaussian, the likelihood function is given by the multivariate Gaussian distribution function:

$$\begin{aligned} L_{WTLS} &= \frac{1}{(2\pi)^N |\Sigma_{\mathbf{d}}|^{1/2}} \exp\left(-\frac{1}{2} \chi_{WTLS}^2\right) \\ &= \frac{1}{(2\pi)^N |\Sigma_{\mathbf{d}}|^{1/2}} \exp\left(-\frac{1}{2} (\vec{d} - \vec{d}')^T \sum_{\mathbf{d}}^{-1} (\vec{d} - \vec{d}')\right), \end{aligned} \quad (4.25)$$

where \vec{d} is a joint vector built from the input vectors \vec{y} and \vec{x} . The vector \vec{d}' is a joint vector built from the corresponding optimized mapping vectors \vec{Y} and \vec{X} . The diagonal matrix $\Sigma_{\mathbf{d}}$ holds the variances $\sigma_{y_i}^2$ followed by $\sigma_{x_i}^2$. In this picture, minimizing the cost function 4.23 is equivalent to maximizing the likelihood function 4.25. Because of the ML-formulation we are able to calculate confidence intervals for \hat{Q} using the Cramer-Rao theorem:

At first we built the log-likelihood function to get rid of the exponential term:

$$\ln(L_{WTLS}) = -\ln\left((2\pi)^N |\Sigma_{\mathbf{d}}|^{1/2}\right) - \frac{1}{2} \chi_{WTLS}^2(\hat{Q}). \quad (4.26)$$

Next, we build the second derivative of 4.26 with respect to \hat{Q}^2 : According to Cramer-Rao's theorem, the lower bound for the variance of the estimator \hat{Q} is given by the negative inverse of the second derivative of the log-likelihood function with respect to \hat{Q}^2 :

$$\frac{\partial^2 \ln(L_{WTLS})}{\partial \hat{Q}^2} = -\frac{1}{2} \frac{\partial^2 \chi_{WTLS}^2}{\partial \hat{Q}^2} \leq -\frac{1}{\sigma_{\hat{Q}}^2}. \quad (4.27)$$

Thus, the lower bound for $\sigma_{\hat{Q}}$ is given by:

$$\sigma_{\hat{Q}}^2 \geq 2 \left(\frac{\partial^2 \chi_{WTLS}^2}{\partial \hat{Q}^2} \right)^{-1}. \quad (4.28)$$

Therefore, we need the Hessian of the cost function in order to calculate a lower bound for $\sigma_{\hat{Q}}^2$. In the case of WTLS approximation the Hessian of the cost function is:

$$\begin{aligned} & \frac{\partial^2 \chi_{WTLS}^2}{\partial \hat{Q}^2} \\ &= 2 \sum_{i=1}^N \gamma^{N-i} \left[\frac{\sigma_{y_i}^4 x_i^2 + \sigma_{x_i}^4 (3\hat{Q}^2 y_i^2 - 2\hat{Q}^3 x_i y_i) - \sigma_{x_i}^2 \sigma_{y_i}^2 (3\hat{Q}^2 x_i^2 - 6\hat{Q} x_i y_i + y_i^2)}{(\hat{Q}^2 \sigma_{x_i}^2 + \sigma_{y_i}^2)^3} \right]. \end{aligned} \quad (4.29)$$

4.3 Goodness of Model Fit

In this section we want to verify whether the regression resulting from one of the Least Square methods is a good approximation for describing the relationship of the input variables x and y . Under the already made assumption that all measurement errors are uncorrelated and Gaussian, the cost functions χ_{WLS}^2 and χ_{WTLS}^2 are distributed

according to the chi-squared distribution. To be more precise in the case of WLS optimization χ_{WLS}^2 is a chi-squared random variable with $k = N - 1$ degrees of freedom. These originate from N input data points (y_1, y_2, \dots, y_N) . One degree of freedom gets lost due to the fitting of \hat{Q} . In the case of WTLS optimization, χ_{WTLS}^2 is a chi-squared random variable with $k = 2N - 1$ degrees of freedom. These originate from N y -input data points (y_1, y_2, \dots, y_N) and N x -input data points (x_1, x_2, \dots, x_N) . Again, one degree of freedom gets lost due to the fitting of \hat{Q} .

To check whether the obtained model reasonably fits the input data, or in other words if we found a good estimate for \hat{Q} , we perform an upper-tailed p-test. In our context we define the hypothesis H_0 as follows: The resulting fit should be a good approximation for describing the relationship of the input variables x and y .

To calculate the upper-tailed p-value for the values of the chi-squared variable $\chi^2 = \chi_{WLS}^2$ and $\chi^2 = \chi_{WTLS}^2$, respectively, we use the Complementary Cumulative Distribution Function (CCDF) of the chi-squared distribution function of the random variable χ . The CCDF gives the probability that χ^2 will take a value greater than χ_{WLS}^2 bzw. χ_{WTLS}^2 .

$$p(\chi^2|N) = 1 - \frac{1}{\Gamma(N/2)} \int_0^{\chi^2} e^{-t} t^{(N/2-1)} dt \quad (4.30)$$

For our purpose we want the p-value to be as high as possible. A value $p \approx 1$ would verify that the hypothesized model and the estimate \hat{Q} are close to the true model and therefore close to the true total cell capacity Q_{tot} . On the other hand, a small value $p \ll 1$ indicates a wrong model or poorly known and maybe non-Gaussian variances $\sigma_{x_i}^2$ and $\sigma_{y_i}^2$.

4.4 Derivation of Recursive Approximate Weighted Total Least Squares

As mentioned before, we need a method which allows arbitrary weighting of squared errors via independent variances $\sigma_{x_i}^2$ and $\sigma_{y_i}^2$ and yields a recursive solution to be suitable for on-board applications. Figure 4.1 shows the geometrical mapping of data points (x_i, y_i) and their corresponding optimized coordinate values (X_i, Y_i) which lie on the line $Y_i = \hat{Q}X_i$. As for the standard non-weighted TLS-method, we claim the line between (x_i, y_i) and (X_i, Y_i) to be perpendicular to the regression line $Y_i = \hat{Q}X_i$. With this constraint we may be able to recursively solve for the estimate. Nevertheless,

4.4 Derivation of Recursive Approximate Weighted Total Least Squares

we weight the distances $\delta x_i = |\overline{x_i X_i}|$ and $\delta y_i = |\overline{y_i Y_i}|$ individually which improves the estimation in contrast to standard non-weighted TLS. As a result, the AWTLS cost function is described via:

$$\chi_{AWTLS}^2 = \sum_{i=1}^N \frac{\delta x_i^2}{\sigma_{x_i}^2} + \frac{\delta y_i^2}{\sigma_{y_i}^2}. \quad (4.31)$$

As shown in Figure 4.1, the distance between the y -coordinate of the i -th data point and the regression line we call $\Delta y_i = y_i - \hat{Q}x_i$. With the slope of the regression line, $\Delta y_i / \Delta x_i = \hat{Q} = \tan(\theta)$ and the trigonometric identity, $\cos\theta = 1/\sqrt{1 + \tan^2\theta}$, we are able to find an expression for R_i , the shortest distance between the i -th datapoint (x_i, y_i) and its optimized mapping (X_i, Y_i) :

$$\begin{aligned} R_i &= \Delta y_i \cdot \cos\theta \\ &= (y_i - \hat{Q}x_i) \cdot \cos\theta \\ &= (y_i - \hat{Q}x_i) \cdot \frac{1}{\sqrt{1 + \tan^2\theta}} \\ &= (y_i - \hat{Q}x_i) \cdot \frac{1}{\sqrt{1 + \hat{Q}^2}} \end{aligned} \quad (4.32)$$

To make it suitable for the estimation of \hat{Q} we rewrite the AWTLS cost function:

$$\begin{aligned} \chi_{AWTLS}^2 &= \sum_{i=1}^N \frac{\delta x_i^2}{\sigma_{x_i}^2} + \frac{\delta y_i^2}{\sigma_{y_i}^2} \\ &= \sum_{i=1}^N \frac{R_i^2 \sin^2\theta}{\sigma_{x_i}^2} + \frac{R_i^2 \cos^2\theta}{\sigma_{y_i}^2}. \end{aligned} \quad (4.33)$$

With the expression 4.32 for R_i we get:

$$\chi_{AWTLS}^2 = \sum_{i=1}^N \frac{(y_i - \hat{Q}x_i)^2}{1 + \hat{Q}^2} \cdot \left(\frac{\sin^2\theta}{\sigma_{x_i}^2} + \frac{\cos^2\theta}{\sigma_{y_i}^2} \right). \quad (4.34)$$

Using $\sin^2\theta = 1 - \cos^2\theta$ and $\cos^2\theta = \frac{1}{1 + \hat{Q}^2}$ finally leads to:

$$\begin{aligned} \chi_{AWTLS}^2 &= \sum_{i=1}^N \frac{(y_i - \hat{Q}x_i)^2}{1 + \hat{Q}^2} \cdot \left(\frac{\hat{Q}^2}{1 + \hat{Q}^2} \frac{1}{\sigma_{x_i}^2} + \frac{1}{1 + \hat{Q}^2} \frac{1}{\sigma_{y_i}^2} \right) \\ &= \sum_{i=1}^N \frac{(y_i - \hat{Q}x_i)^2}{(1 + \hat{Q}^2)^2} \cdot \left(\frac{\hat{Q}^2}{\sigma_{x_i}^2} + \frac{1}{\sigma_{y_i}^2} \right). \end{aligned} \quad (4.35)$$

At this point it should be emphasized that AWTLS is an approximation to WTLS. Both cost functions, χ_{WTLS}^2 and χ_{AWTLS}^2 , are identical in the case of identical variances

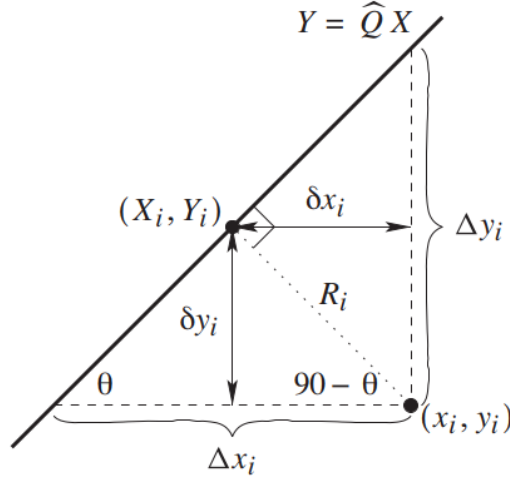


Figure 4.1: Geometrical mapping of data points (x_i, y_i) and corresponding (X_i, Y_i) for the Approximate Total Least Square method (Plett, 2011)

in x and y ($\sigma_{x_i}^2 = \sigma_{y_i}^2$). For arbitrary variances in x and y they are slightly different. Nevertheless, both methods yield very akin results which will be shown later.

Again by introducing a fading memory factor γ , we slightly alter the cost function to put more emphasis on recently gathered input data leading to:

$$\chi_{AWTLS}^2 = \sum_{i=1}^N \gamma^{N-i} \frac{(y_i - \hat{Q}x_i)^2}{(1 + \hat{Q}^2)^2} \cdot \left(\frac{\hat{Q}^2}{\sigma_{x_i}^2} + \frac{1}{\sigma_{y_i}^2} \right). \quad (4.36)$$

To find the local minimum of this function we need its derivative which is:

$$\begin{aligned} \frac{\partial \chi_{AWTLS}^2}{\partial \hat{Q}} = & \frac{2}{(\hat{Q}^2 + 1)^3} \sum_{i=1}^N \gamma^{N-i} \left[\left(\frac{x_i y_i}{\sigma_{x_i}^2} \right) \cdot \hat{Q}^4 + \left(\frac{2x_i^2}{\sigma_{x_i}^2} - \frac{x_i^2}{\sigma_{y_i}^2} - \frac{y_i^2}{\sigma_{x_i}^2} \right) \cdot \hat{Q}^3 \right. \\ & \left. + \left(\frac{3x_i y_i}{\sigma_{y_i}^2} - \frac{3x_i y_i}{\sigma_{x_i}^2} \right) \cdot \hat{Q}^2 + \left(\frac{x_i^2 - 2y_i^2}{\sigma_{y_i}^2} + \frac{y_i^2}{\sigma_{x_i}^2} \right) \cdot \hat{Q} + \left(\frac{-x_i y_i}{\sigma_{y_i}^2} \right) \right]. \end{aligned} \quad (4.37)$$

As stated before, the estimate \hat{Q} gets calculated every time new input data is gathered. To make the algorithm computationally more suitable for embedded systems, we strive for a recursive formulation. For this purpose we define the recursively computing sums:

4.4 Derivation of Recursive Approximate Weighted Total Least Squares

$$\begin{aligned}
c_{1,n} &= \frac{\gamma c_{1,n-1} + x_n^2}{\sigma_{y_n}^2} \\
c_{2,n} &= \frac{\gamma c_{2,n-1} + x_n y_n}{\sigma_{y_n}^2} \\
c_{3,n} &= \frac{\gamma c_{3,n-1} + y_n^2}{\sigma_{y_n}^2} \\
c_{4,n} &= \frac{\gamma c_{4,n-1} + x_n^2}{\sigma_{x_n}^2} \\
c_{5,n} &= \frac{\gamma c_{5,n-1} + x_n y_n}{\sigma_{x_n}^2} \\
c_{6,n} &= \frac{\gamma c_{6,n-1} + y_n^2}{\sigma_{x_n}^2},
\end{aligned}$$

where n is the present index of the last gathered input data pair (x_i, y_i) and therefore the actual length of the input vectors \vec{x} and \vec{y} . For the recursive calculation of these sums we need to define initial values. We pretend an artificial initial measurement where we set $x_0 = 1$ and $y_0 = Q_{nom}$. For $\sigma_{y_0}^2$ the variance of the nominal capacity given by the cell manufacturer is used. $\sigma_{x_0}^2$ is set to a reasonable value depending on the used SoC estimation method. These assumptions lead to the following initial values for the sums:

$$c_{1,0} = \frac{1}{\sigma_{y_0}^2}; \quad c_{2,0} = \frac{Q_{nom}}{\sigma_{y_0}^2}; \quad c_{3,0} = \frac{Q_{nom}^2}{\sigma_{y_0}^2}; \quad c_{4,0} = \frac{1}{\sigma_{x_0}^2}; \quad c_{5,0} = \frac{Q_{nom}}{\sigma_{x_0}^2}; \quad c_{6,0} = \frac{Q_{nom}^2}{\sigma_{x_0}^2}.$$

We can re-write the derivative in terms of these recursive sums as:

$$\begin{aligned}
\frac{\partial \chi_{AWTLS}^2}{\partial \hat{Q}} &= \frac{2}{(\hat{Q}^2 + 1)^3} \left[c_{5,N} \cdot \hat{Q}^4 + (-c_{1,N} + 2c_{4,N} - c_{6,N}) \cdot \hat{Q}^3 \right. \\
&\quad \left. + (3c_{2,N} - 3c_{5,N}) \cdot \hat{Q}^2 + (c_{1,N} - 2c_{3,N} + c_{6,N}) \cdot \hat{Q} - c_{2,N} \right]. \tag{4.38}
\end{aligned}$$

To find the best value for \hat{Q} , we set the derivative to zero which yields a quartic equation for which the roots have to be found. These roots are candidate solutions for the estimate \hat{Q} . Because a quartic equation has four roots we have to choose the right one to be \hat{Q} . To do so we firstly can ignore complex or negative roots as the cell's capacity can't be a negative or complex number. The next step is to evaluate the cost function for all positive real roots. The root candidate which yields the lowest value for the cost function represents the best value \hat{Q} for the estimate of the actual total cell capacity Q_{tot} .

4 Total Capacity Estimation via Approximate Total Least Squares

To evaluate the cost function, it also can be expressed in terms of the recursive sums:

$$\chi_{AWTLS}^2 = \frac{1}{(\hat{Q}^2 + 1)^2} \left[c_{4,N} \cdot \hat{Q}^4 + 2c_{5,N} \cdot \hat{Q}^3 + (c_{1,N} + c_{6,N}) \cdot \hat{Q}^2 - 2c_{2,N} \cdot \hat{Q} + c_{3,N} \right] \quad (4.39)$$

For the calculation of confidence intervals as described in Section 4.2, we need the Hessian of the cost function which is given by:

$$\begin{aligned} \frac{\partial^2 \chi_{AWTLS}^2}{\partial \hat{Q}^2} = \frac{2}{(\hat{Q}^2 + 1)^4} & \left[-2c_{5,N} \cdot \hat{Q}^5 + (3c_{1,N} - 6c_{4,N} + 3c_{6,N}) \cdot \hat{Q}^4 \right. \\ & + (-12c_{2,N} + 16c_{5,N}) \cdot \hat{Q}^3 + (-8c_{1,N} + 10c_{3,N} + 6c_{4,N} - 8c_{6,N}) \cdot \hat{Q}^2 \\ & \left. + (12c_{2,N} - 6c_{5,N}) \cdot \hat{Q} + (c_{1,N} - 2c_{3,N} + c_{6,N}) \right] \end{aligned} \quad (4.40)$$

With the approach of AWTLS we derived a regression method which has nice properties for on-board use. Firstly, it gives a closed-form solution for the estimate \hat{Q} . No more sophisticated methods are needed which leads to high computational efficiency. Furthermore, it features fading memory of past measurements via the forgetting factor γ and recursive calculation of \hat{Q} , which additionally makes it lean in performance requirements and therefore suitable for embedded applications.

4.5 Algorithm Testing and Results

For validation of the described AWTLS algorithm, it is applied to real measurement data. To test whether the estimation method is suitable for the on-board use in electric vehicles, the chosen data originates from the drive cycle ageing test of one of the three tested cells as described in section 3.3.1. All of the computing was achieved with MATLAB ©2016b.

4.5.1 Input Data Generation

The backbone of the investigated onboard-capacity estimation problem is represented by the Equation 4.1. In order to test the method, input data vectors \vec{x} and \vec{y} as well as the corresponding variances σ_x^2 and σ_y^2 are needed.

In order to generate the components of \vec{y} , numerical current integration via the MATLAB intern function *cumtrapz* was used. The coulombic efficiency factor η was set to one. For the acquisition of measurement data the channels with a measurement range of $I_{max} = \pm 5$ A were used on the Arbin BT-2000 Battery Test System. In this

measurement range the higher bound for the relative error of the measured values is $\Delta I_t = 0.02 \cdot I_t$. As a result of the current integration the corresponding errors also sum over time. Therefore, unnecessary long sampling intervals lead to higher accumulated errors σ_y and should be avoided.

For the generation of the x -input two approaches were used. Firstly, a simple voltage-based SoC estimation was made via the OCV-SoC method as described in Section 2.3.2.2. The used OCV-SoC lookup table can be seen in Figure 4.2 and was gained through measurements performed at the Virtual Vehicle Research GmbH. Since the OCV-SoC relationship varies with temperature and ageing status of the cell, a detailed declaration of the errors occurring through this method is hardly possible. Therefore, a generous accuracy of $\sigma_{SoC} = 0.05$ was assumed.

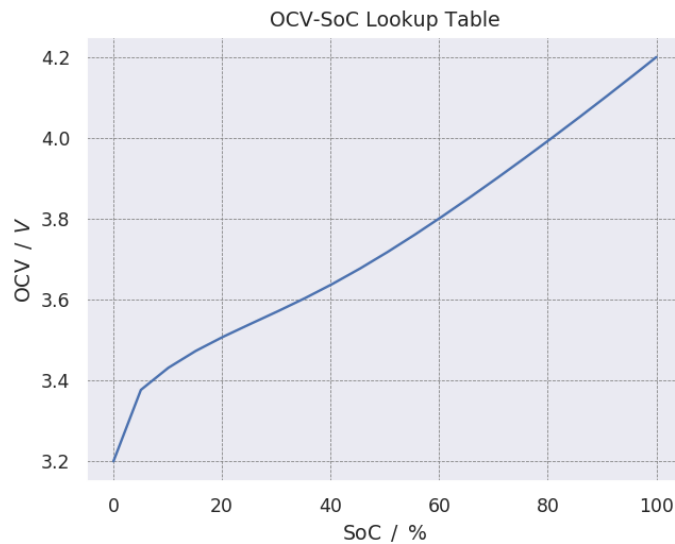


Figure 4.2: Lookup Table showing the OCV-SoC relationship

As mentioned before, the OCV-SoC method only delivers reliable SoC estimates if the cell is near electrochemical equilibrium. In other words, the cells terminal voltage should have relaxed close to the OCV. Therefore, the charge/discharge current has to be zero for a certain amount of time.

The other method used for SoC estimation is a more sophisticated model-based one. It combines a second order RC-model with EKF algorithm. A detailed description of this method would go beyond the scope of this work, but it can be found in the work of Hrvanovic (2018). Based on literature (Plett (2015b); Hrvanovic (2018)), for the SoC estimates made by this method the accuracy was set to $\sigma_{SoC} = 0.02$.

Sampling Methods: In order to generate the input data-points as stated in the equations 4.11 and 4.12 a strategy to choose the supporting points (t_{i_1}, t_{i_2}) of each sampling interval is needed. For the purpose of algorithm testing two sampling approaches were applied:

1. Firstly, a sampling method suitable for the OCV-SoC estimation method was implemented. This method we call *zero-current* sampling. When sampling occurs in *zero-current* mode, we put constraints on the charge/discharge current. We force the algorithm to only search for supporting points (t_{i_1}, t_{i_2}) where the current was zero before for a certain *zero-current duration* T_{zero} . With this claim we can be certain that the measured terminal voltage is at least near the OCV.
2. Secondly, a rough sampling to which we refer to as *fixed-sampling* was realized where the time interval per data-point is set to a constant value T_{fixed} . For our purpose the *fixed-sampling duration* was set to $T_{fixed} = 3600s$. This method is expected to show the advantages of EKF based SoC estimation since this method does not rely on a relaxed terminal voltage. Therefore, it is able to estimate the SoC dynamically and non-invasively.

For sampling intervals chosen by each of these methods, an additional constraint was made. To be considered in the optimization process we forced the change in SoC within an interval to be at least 5%.

4.5.2 Results and Discussion

In this section the results from testing the AWTLS algorithm are presented and discussed afterwards. For all tests the nominal capacity for AWTLS initialization was set to the rated capacity value delivered by the manufacturing company $Q_{nom} = 3.2 \text{ Ah}$.

Zero-Current Sampling: Figure 4.3 shows the results of estimating the total cell capacity Q_{tot} with *zero-current* sampling. The *zero-current duration* was set to $T_{zero} = 20 \text{ min}$ and SoC estimation was executed with the OCV-SoC lookup table. The forgetting factor was set to $\gamma = 0.985$. The corresponding Goodness of Fit is shown in the subsequent Figure 4.4.

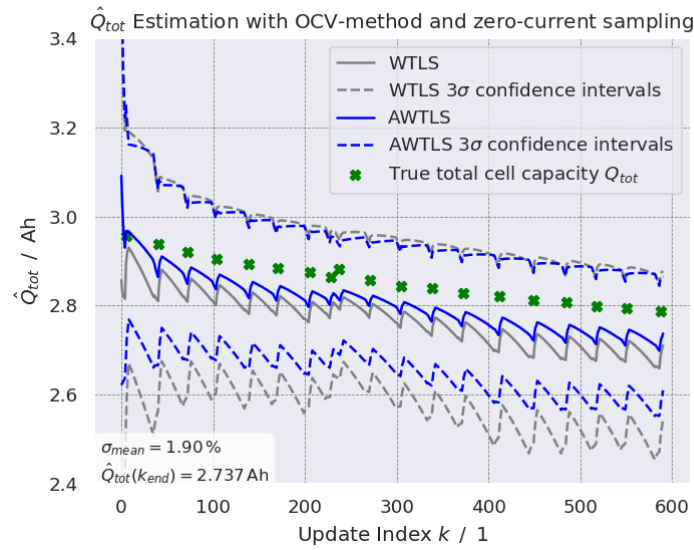


Figure 4.3: Estimation of Q_{tot} with zero-current sampling with $T_{zero} = 20$ min and SoC estimation via OCV-SoC lookup table. The forgetting factor was set to $\gamma = 0.985$. **grey:** WTLS estimate; **blue:** AWTLS estimate; The **dashed lines** illustrate the corresponding 3σ confidence intervals.

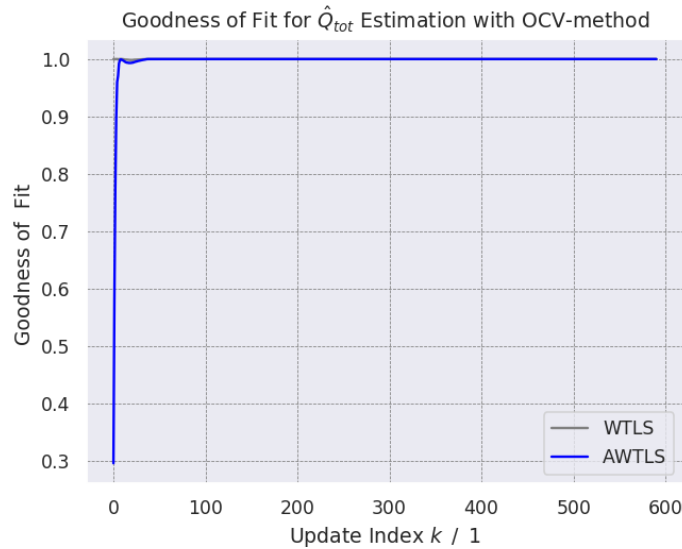


Figure 4.4: Goodness of Model Fit for the Estimation of Q_{tot} with zero-current sampling with $T_{zero} = 20$ min and SoC estimation via OCV-method. The forgetting factor was set to $\gamma = 0.985$. **grey:** WTLS; **blue:** AWTLS.

Both WTLS and AWTLS give slightly biased estimates \hat{Q} . This effect originates most likely from the error of the applied OCV-SoC method used for SoC estimation, since it is dependent on temperature as well as C-rate and current sign before relaxation of the terminal voltage. It is also assumed to cause the fringes which can be seen in the

4 Total Capacity Estimation via Approximate Total Least Squares

estimate and its boundaries because of different operation conditions during RTPs and LPs. AWTLS gives better results because its estimate is closer to the true values for Q_{tot} and has narrower error bounds. The error bounds on both WTLS and AWTLS are reasonably wide which leads to a high Goodness of Fit. The mean value of the estimated standard deviation \hat{Q} is quite high with $\sigma = 1.90\%$ of Q_{tot} .

Figure 4.5 shows the results of estimating the total cell capacity Q_{tot} with *zero-current* sampling. The *zero-current duration* was set to $T_{zero} = 20$ min and this time SoC estimation was executed with the more sophisticated EKF. The forgetting factor was set to $\gamma = 0.985$. The corresponding Goodness of Fit is shown in the subsequent Figure 4.6.

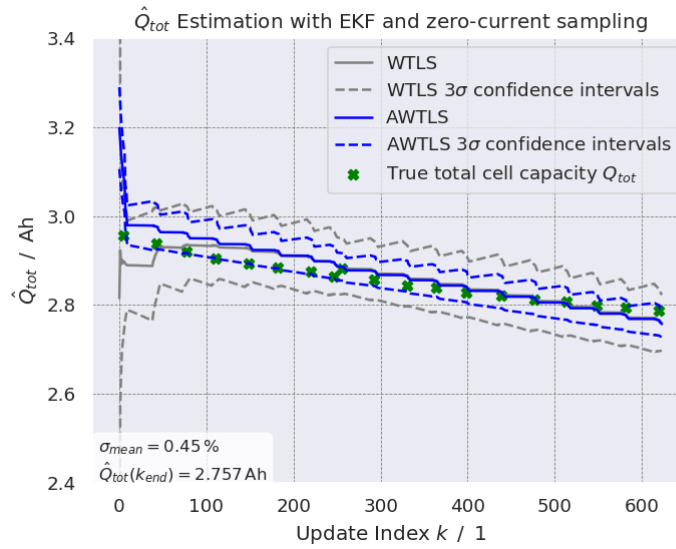


Figure 4.5: Estimation of Q_{tot} with zero-current sampling with $T_{zero} = 20$ min and SoC estimation via EKF. The forgetting factor was set to $\gamma = 0.985$. **grey:** WTLS estimate; **blue:** AWTLS estimate; The **dashed lines** illustrate the corresponding 3 σ confidence intervals.

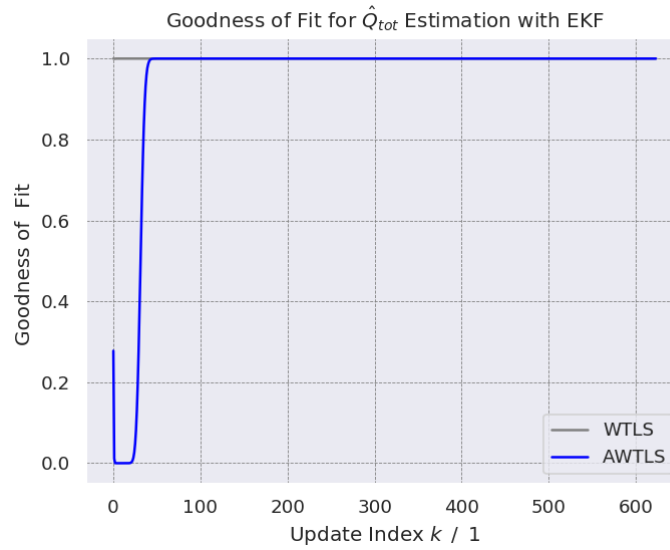


Figure 4.6: Goodness of Model Fit for the Estimation of Q_{tot} with zero-current sampling with $T_{zero} = 20$ min and SoC estimation via EKF. The forgetting factor was set to $\gamma = 0.985$. **grey:** WTLS; **blue:** AWTLS.

Like shown in Figure 4.5, both WTLS and AWTLS track the true capacity Q_{tot} very well. Until $k = 100$, AWTLS gives more realistic values for Q_{tot} because of the ability to initialize the estimate. Furthermore, due to this feature AWTLS gives lower error bounds. The error bounds on both WTLS and AWTLS are reasonably wide which leads to a high Goodness of Fit. The mean value of the estimate's \hat{Q} standard deviation is quite low with $\sigma = 0.35\%$ of Q_{tot} . This leads to an accurate capacity estimation with three-sigma error bounds of about $\pm 1.1\%$.

Fixed Sampling: Figure 4.7 shows the results of estimating the total cell capacity Q_{tot} with *fixed-interval* sampling. The *fixed-interval duration* was set to $T_{fixed} = 3600$ s and SoC estimation was executed with the OCV-SoC method. The forgetting factor was set to $\gamma = 0.99$. The corresponding Goodness of Fit is shown in the subsequent Figure 4.8.

Both WTLS and AWTLS give very noisy estimates \hat{Q} which are practically unusable. This shows the limitations of the used OCV-SoC relationship for SoC estimation. In *fixed sampling* mode, there are no further constraints regarding sampling which leads to non-relaxed terminal voltage values very distant from the actual OCV. This results in highly erroneous SoC estimates. WTLS and AWTLS give the same results with a very high value of σ which leads to three-sigma error bounds of about $\pm 10\%$. Nevertheless,

4 Total Capacity Estimation via Approximate Total Least Squares

both WTLS and AWTLS show high values for the goodness of fit.

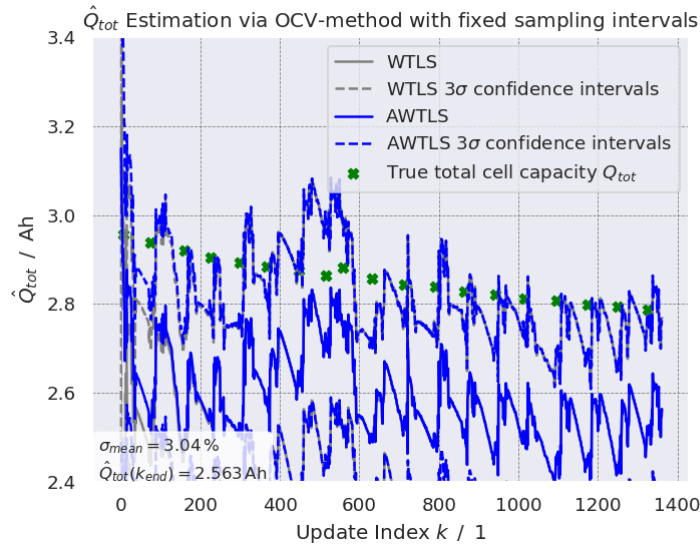


Figure 4.7: Estimation of Q_{tot} with fixed-interval sampling with $T_{fixed} = 3600$ s and SoC estimation via OCV-method. The forgetting factor was set to $\gamma = 0.99$. **grey:** WTLS estimate; **blue:** AWTLS estimate; The **dashed lines** illustrate the corresponding 3σ confidence intervals.

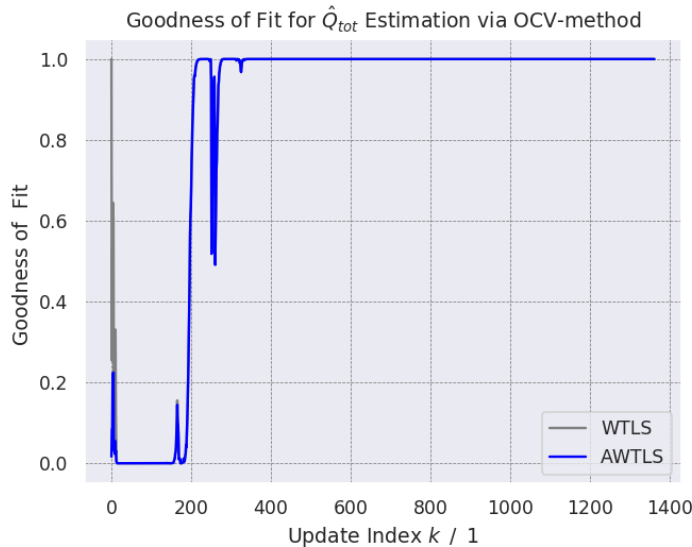


Figure 4.8: Goodness of Model Fit for the Estimation of Q_{tot} with fixed-interval sampling with $T_{fixed} = 3600$ s and SoC estimation via OCV-method. The forgetting factor was set to $\gamma = 0.99$. **grey:** WTLS; **blue:** AWTLS.

Figure 4.9 shows the results of estimating the total cell capacity Q_{tot} with *fixed-interval* sampling. The *fixed-interval duration* was set to $T_{fixed} = 3600$ s and SoC estima-

tion was executed with the more sophisticated EKF. The forgetting factor was set to $\gamma = 0.99$. The corresponding Goodness of Fit is shown in the subsequent Figure 4.10.

Both WTLS and AWTLS track the true capacity Q_{tot} very well, even though we used *fixed sampling*. Until $k = 200$, AWTLS gives more realistic values for Q_{tot} because of the ability to initialize the estimate. Besides this, WTLS and AWTLS give the same results. The error bounds on both, WTLS and AWTLS, are reasonable wide which leads to a high Goodness of Fit. The mean value of the standard deviation of \hat{Q} is higher than in the case where *zero-current* sampling was used (Figure 4.5), but it is still low with $\sigma = 0.56\%$. This leads to an accurate capacity estimation with three-sigma error bounds of $\pm 1.8\%$. Furthermore, the method is highly non-invasive due to no needed constraints for input data generation.

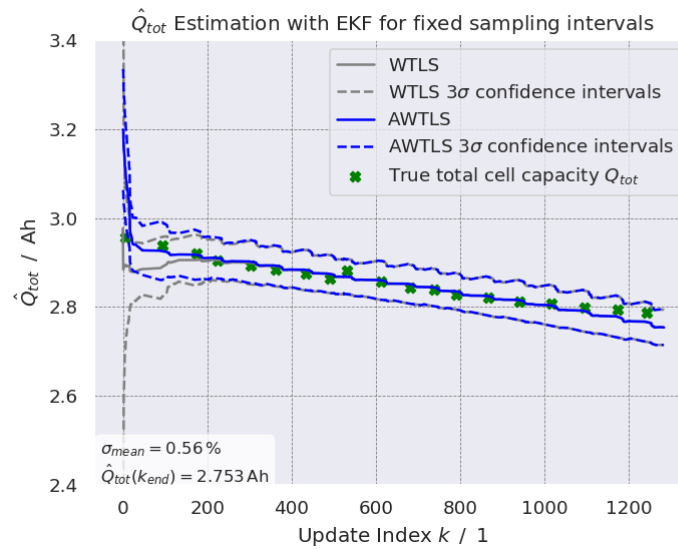


Figure 4.9: Estimation of Q_{tot} with fixed-interval sampling with $T_{fixed} = 3600$ s and SoC estimation via EKF-method. The forgetting factor was set to $\gamma = 0.99$. **grey:** WTLS estimate; **blue:** AWTLS estimate; The **dashed lines** illustrate the corresponding 3σ confidence intervals.

4 Total Capacity Estimation via Approximate Total Least Squares

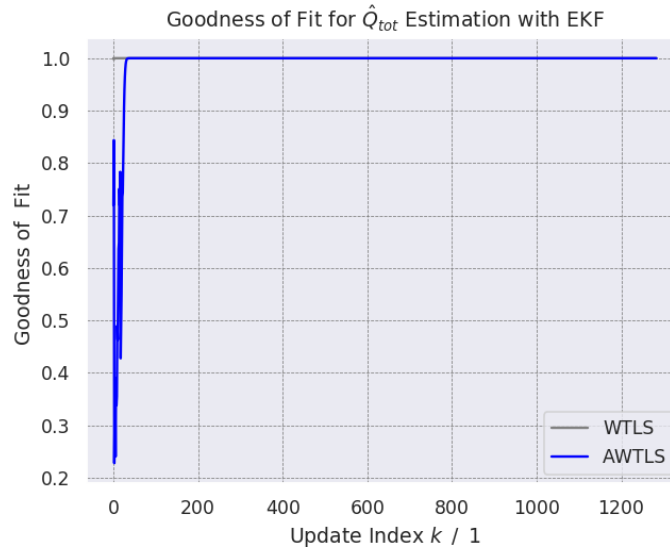


Figure 4.10: Goodness of Model Fit for the Estimation of Q_{tot} with fixed-interval sampling with $T_{fixed} = 3600$ s and SoC estimation via EKF-method. The forgetting factor was set to $\gamma = 0.99$. **grey:** WTLS; **blue:** AWTLS.

To conclude, AWTLS seems to be a suitable choice for on-board capacity estimation in automotive applications. With its ability to consider errors on both, the coulomb counting and SoC estimation, it is more favorable than standard least square methods. In contrast to WTLS, AWTLS features recursive formulation and the ability to initialize the estimate with an arbitrary value which leads to faster convergence. Recursive formulation and forgetting memory factor make AWTLS well suited especially for embedded systems implementation.

The results show that AWTLS performs particularly well in conjunction with the more sophisticated EKF-method for SoC estimation, validated by narrow error bounds even for simple *fixed-sampling*. However, EKF is computationally expensive.

As mentioned previously, Bayesian SLR was tested for one dataset to compare it with the investigated methods. The result of this test can be seen in Figure 4.11. Here, one can see that Bayesian SLR yields identical results as the WTLS method. Furthermore, it also features forgetting memory of past measurements and recursive computation of the estimate. According to this test, the measured runtime of Bayesian SLR was very similar to the one of AWTLS. Therefore, Bayesian SLR could be another suitable choice for on-board capacity estimation which has to be further investigated.

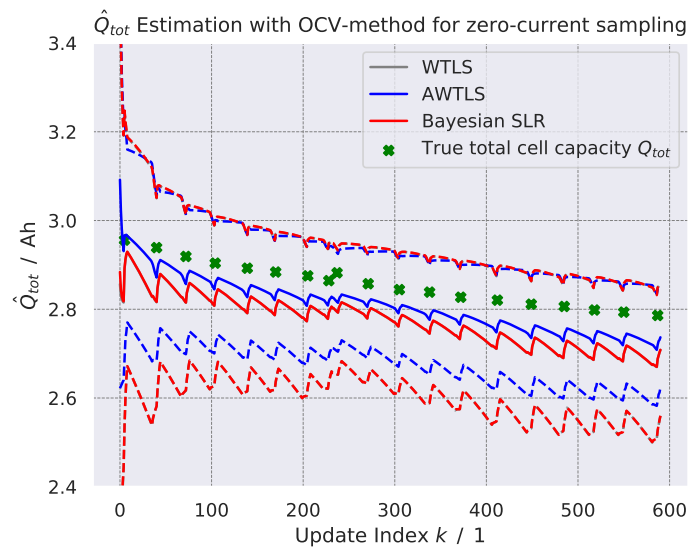


Figure 4.11: Estimation of Q_{tot} with zero-current sampling with $T_{zero} = 20$ min and SoC estimation via OCV-SoC lookup table. The forgetting factor was set to $\gamma = 0.985$. **grey:** WTLS estimate; **blue:** AWTLS estimate; **red:** Bayesian SLR estimate; The **dashed lines** illustrate the corresponding 3σ confidence intervals.

5

Conclusion

This work deals with the investigation of methods for SoH estimation of Li-ion cells for automotive applications. Firstly, a brief introduction to Li-ion cells and their working principle was given. Afterwards, for a better understanding their ageing behaviour and main mechanisms of degradation were described.

To verify the performance of the investigated methods they were applied to measurement data originating from extensive ageing tests taken with commercial Panasonic NCR18650B cells at the Virtual Vehicle Research GmbH. Within these tests the cells were loaded by drive cycles as well as calendric and cyclic LPs over a timespan of about two years to simulate the ageing process within a cell's lifespan.

The first method applied to the measurement data is an ICA-method which is closely related to the approach described in the work of Li et al. (2018) and analyses the charge characteristics during the CC charging process. It considers the position of a local peak in the IC-curve to relate to the cell's SoH. After the extraction of the IC-curves from data, collected during the RTPs, they were smoothed via discrete convolution with a Gaussian filter. Afterwards, the relation between the locations of IC-peaks from each RTP and the corresponding SoH was approximated by linear regression.

Secondly, a method based on analysing the dynamic behaviour of the cell's charge current during CV charging process was applied to the ageing-datasets. In order to describe the dynamic behaviour of the charge current an exponential decaying function was used. Following this, the relation between strength of the current decay, described by the characteristic time constant τ , and the cell's SoH was investigated by linear regression analysis.

5 Conclusion

In contrast to previous publications regarding SoH estimation by methods based on the analysis of charging characteristics, we applied these to a more complex set of load conditions to investigate its effect on the method's performance. These variations of the load conditions include different temperatures, SoC-levels during storage as well as varying SoC-deflections during cyclic ageing.

According to the results presented in Section 3.3, ICA was able to describe a cell's degradation in SoH evoked by drive cycle ageing with an absolute error (2-sigma bounds) of $\pm 2.1\%$ and by calendric ageing with an maximum absolute error of $\pm 6.1\%$. Although, such a high error only occurs at radical ageing evoked through a combination of high SoC-level and temperature ($SoC = 95\%$ and $T = 45^\circ\text{C}$). For all other calendric ageing scenarios the method was able to describe the cell's SoH within a maximum absolute error of less than $\pm 2.4\%$. In the case of cyclic ageing, ICA was capable of describing the capacity fade within a maximum absolute error of $\pm 3.7\%$. But it has to be mentioned that the method showed instability at cyclic ageing by low temperature and SoC-deflection ($T = 0^\circ\text{C}$ and $dSoC = 2.5\%$) due to alteration of the IC-curves (shown in figure 3.32).

In contrast, CV-Analysis showed an overall weaker performance. In the case of drive cycle ageing, it described SoH within an absolute error of about $\pm 4.1\%$ and for calendric ageing within a maximum absolute error of about $\pm 9.0\%$. As for ICA, such high error only occurs at radical ageing caused by high SoC-level paired with elevated temperature ($SoC = 95\%$ and $T = 45^\circ\text{C}$). For all other calendric ageing scenarios the method was able to describe the cell's SoH within a maximum absolute error of less than $\pm 3.2\%$. In the case of cyclic ageing, CV-Analysis was capable of describing the capacity fade within a maximum absolute error of $\pm 3.8\%$. An advantage of the CV-method is that it can be applied for every full CV charging process. Therefore, it is independent of initial SoC as long as CV charging is fully executed.

As the results show, both investigated methods are highly dependent on the cell's operation conditions during ageing. Therefore, none of the methods were able to find a single linear function which describes the deterioration of SoH with a passable accuracy. From this perspective these methods can only be applied when the operation conditions are well known and repetitive over the cell's whole lifespan. This discards them as techniques for on-board SoH estimation.

The third objective of this work was to investigate the performance of AWTLS, an

optimization method for on-board capacity estimation. The optimization problem is given by the linear relationship between accumulated charge/discharge current and change in the cell's SoC (Equation 4.1). Unlike the regularly used Least Square methods this method considers both the error originating by current integration as well as the error due to SoC estimation. Generally, AWTLS is based on WTLS optimization but features some nice properties which makes it more suitable for embedded hardware application. These include recursive formulation and forgetting memory which makes it lean in required storage amount and processing power.

To examine the methods performance under realistic usage conditions, this method was applied to measurement data originating from a drive cycle ageing-test. For the generation of input data two sampling methods were implemented. With *zero-current sampling* we forced the charge/discharge current to be zero at least for $T_{zero} = 20$ min to guarantee a quasi-relaxed terminal voltage. Secondly, with *fixed sampling* the input data intervals were set to a mandatory duration of $T_{fixed} = 3600$ s.

The AWTLS algorithm was tested in combination with two SoC estimation methods. Firstly, the simple OCV-SoC relationship was used to estimate the cell's SoC. For this case with *zero-current sampling*, AWTLS gave better results than the WTLS algorithm as its estimate \hat{Q} is closer to the values of true total capacity Q_{tot} . Here AWTLS was able to estimate the cell's total capacity with a mean absolute error of $\sigma = 1.90\%$. The results obtained with *fixed sampling* display the weakness of the OCV-SoC method. This rough sampling led to non-relaxed terminal voltage values very distant from the actual OCV which resulted in highly erroneous and practically unusable SoC estimates for both WTLS and AWTLS. Secondly, AWTLS was used in combination with a more complex model based SoC estimation method which combines a second order RC-model with EKF. In combination with this method, AWTLS was able to estimate the cell's total capacity with a mean absolute error of less than $\sigma = 0.6\%$ independent on the used sampling method.

To conclude, through AWTLS an accurate capacity estimation with 3-sigma error bounds of about $\pm 1.8\%$ was accomplished. In combination with EKF, this method is highly non-invasive because no constraints for input data generation are needed. Furthermore, due to the method's features of recursive computation and forgetting memory implementation it seems to be a suitable choice for on-board SoH estimation. Further research work could be the hardware implementation of AWTLS for real testing.

List of Abbreviations

AWTLS	Approximate Weighted Total Least Squares
BMS	Battery Management System
CC	Constant-Current
CCDF	Complementary Cumulative Distribution Function
CV	Constant-Voltage
EKF	Extended Kalman Filter
EoL	End of Life
ESS	Energy Storage System
EV	electric vehicle
FMLS	Fading Memory Least Squares
FMWLS	Fading Memory Weighted Least Squares
FP	Feature Point
GHG	greenhouse gas
GS	Gaussian Smoothing
HEV	hybrid electric vehicle
IC	Incremental Capacity
ICA	Incremental Capacity Analysis
Li-ion	lithium-ion
LIB	lithium-ion Battery
LP	Load Profile
LS	Least Squares
ML	maximum-likelihood

List of Abbreviations

NMC	lithium nickel manganese cobalt oxide
OCV	Open-Circuit-Voltage
PDF	probability density function
PHEV	Plugin HEV
RMSE	Root Mean Square Error
RTP	Reference Test Procedure
SEI	Solid Electrolyte Interface
SLR	Straight Line Regression
SoC	State of Charge
SoH	State of Health
SVR	Support Vector Regression
TLS	Total Least Squares
WLS	Weighted Least Squares
WTLS	Weighted Total Least Squares

List of Figures

1.1	volumetric energy density (Wh/l) and gravimetric energy density(Wh/kg) for the major small-sealed recharge- able battery technologies (Beggi et al., 2018)	2
2.1	Basic working principle of a electrochemical cell (Plett, 2015a)	8
2.2	Open-Circuit-Potential of Graphite vs. another negative electrode material candidate (LTO) (Plett, 2015b)	10
2.3	Overview of predominant ageing mechanisms in the negative electrode of Li-ion cells (Barré et al., 2013)	12
2.4	Overview of predominant ageing mechanisms in the positive electrode of Li-ion cells and inactive materials (Vetter et al., 2005)	14
2.5	layout of composite electrode structure (Plett, 2015b)	14
2.6	Example for OCV curve of a LiPB cell (Xiong et al., 2017)	19
2.7	Basic structure of model-based SoC estimation methods (Plett, 2015b)	20
3.1	Example for a cell’s SoH progression during a performance of an ageing test. The scatters refer to total cell capacities being measured during the corresponding RTP’s at $T = 25\text{ }^{\circ}\text{C}$	22
3.2	RTP example measurement. The upper graph (blue) displays measured current (in A) over time. The lower graph (green) shows an estimate for the SoC (in %) over time. The dashed lines (orange) and the bottom-most labels depict the individual phases of the RTP.	24
3.3	Shows partly data collected during execution of a RTP, blue: Terminal Voltage V , red: Current I , green: Stepindex n ; The vertical lines in violet mark the scope for the extraction of the data during the CC charging process.	27
3.4	Example of a set of loading curves extracted from an ageing-dataset. Brighter curves represent less aged cell status.	28
3.5	Example of a set of noisy IC-curves extracted from an ageing-dataset. Brighter curves represent less aged cell status.	29
3.6	Example of a set of smoothed IC-curves extracted from an ageing-dataset. Brighter curves represent less aged cell status.	31

List of Figures

3.7	Example of a set of smoothed IC-curves with FPs from a ageing-dataset. The extracted FPs correspond to the second local maxima from the right side. Brighter curves represent less aged cell status.	32
3.8	Example scatter plot of the FP-location versus SoH for a single cell. Brighter dots refer to less aged cell status.	33
3.9	Linear fit of the FP-location versus SoH for three cells. Each of the cells was aged with the same drive cycle LP.	34
3.10a	Scatter plot of the FP-location versus SoH for cells being aged calendric by L202: $T = 45\text{ }^{\circ}\text{C}$, $\text{SoC} = 15\%$	35
3.10b	Scatter plot of the FP-location versus SoH for cells being aged calendric by L206: $T = 45\text{ }^{\circ}\text{C}$, $\text{SoC} = 95\%$	36
3.11a	Scatter plot of the FP-location versus SoH for cells being aged calendric by L201: $T = 0\text{ }^{\circ}\text{C}$, $\text{SoC} = 15\%$	36
3.11b	Scatter plot of the FP-location versus SoH for cells being aged calendric by L203: $T = 0\text{ }^{\circ}\text{C}$, $\text{SoC} = 55\%$	37
3.12a	Scatter plot of the FP-location versus SoH for cells being aged calendric by L201: $\text{SoC} = 15\%$, $T = 0\text{ }^{\circ}\text{C}$	38
3.12b	Scatter plot of the FP-location versus SoH for cells being aged calendric by L202: $\text{SoC} = 15\%$, $T = 45\text{ }^{\circ}\text{C}$	38
3.13a	Scatter plot of the FP-location versus SoH for cells being aged calendric by L203: $\text{SoC} = 55\%$, $T = 0\text{ }^{\circ}\text{C}$	39
3.13b	Scatter plot of the FP-location versus SoH for cells being aged calendric by L204: $\text{SoC} = 55\%$, $T = 30\text{ }^{\circ}\text{C}$	39
3.14a	Scatter plot of the FP-location versus SoH for cells being aged calendric by L205: $\text{SoC} = 95\%$, $T = 20\text{ }^{\circ}\text{C}$	40
3.14b	Scatter plot of the FP-location versus SoH for cells being aged calendric by L206: $\text{SoC} = 95\%$, $T = 45\text{ }^{\circ}\text{C}$	41
3.15a	Scatter plot of the FP-location versus SoH for cells being aged cyclic by L208: $\text{dSoC} = 2.5\%$, $T = 0\text{ }^{\circ}\text{C}$	42
3.15b	Scatter plot of the FP-location versus SoH for cells being aged cyclic by L209: $\text{dSoC} = 2.5\%$, $T = 45\text{ }^{\circ}\text{C}$	42
3.16a	Scatter plot of the FP-location versus SoH for cells being aged cyclic by L215: $\text{dSoC} = 80\%$, $T = 0\text{ }^{\circ}\text{C}$	43
3.16b	Scatter plot of the FP-location versus SoH for cells being aged cyclic by L216: $\text{dSoC} = 80\%$, $T = 45\text{ }^{\circ}\text{C}$	43

3.17a Scatter plot of the FP-location versus SoH for cells being aged cyclic by L209: $T = 45\text{ }^{\circ}\text{C}$, $\text{dSoC} = 2.5\%$ 44

3.17b Scatter plot of the FP-location versus SoH for cells being aged cyclic by L216: $T = 45\text{ }^{\circ}\text{C}$, $\text{dSoC} = 80\%$ 44

3.18 Typical CC-CV charging process of a lithium-ion cell (Z. Wang et al., 2019) 45

3.19 Shows partly data collected during execution of a RTP, **blue**: Terminal Voltage V , **red**: Current I , **green**: Stepindex n ; The vertical lines in **violet** mark the scope for the extraction of the data during the CV charging process. 46

3.20 $I(t)$ during CV charging extracted from an ageing-dataset. Brighter curves represent less aged cell status. 47

3.21 Fit of the charge current time series extracted from the first and last RTP of an ageing-dataset with exponential decay function. **bright green**: originates from the unaged cell (first RTP); **dark blue**: originates from the aged cell (last RTP); **red**: data generated by the obtained fit functions. 48

3.22 Example scatter plot of the decay constant τ versus SoH. Brighter dots refer to less aged cell status. 49

3.23 Scatter plot and linear regression of the decay constant τ versus SoH for cells being aged by the drive cycle V208. 50

3.24a Scatter plot of the decay constant τ versus SoH for cells being aged calendric by L202: $T = 45\text{ }^{\circ}\text{C}$, $\text{SoC} = 15\%$ 51

3.24b Scatter plot of the decay constant τ versus SoH for cells being aged calendric by L206: $T = 45\text{ }^{\circ}\text{C}$, $\text{SoC} = 95\%$ 51

3.25a Scatter plot of the decay constant τ versus SoH for cells being aged calendric by L201: $T = 0\text{ }^{\circ}\text{C}$, $\text{SoC} = 15\%$ 52

3.25b Scatter plot of the decay constant τ versus SoH for cells being aged calendric by L203: $T = 0\text{ }^{\circ}\text{C}$, $\text{SoC} = 55\%$ 52

3.26a Scatter plot of the decay constant τ versus SoH for cells being aged calendric by L201: $\text{SoC} = 15\%$, $T = 0\text{ }^{\circ}\text{C}$ 53

3.26b Scatter plot of the decay constant τ versus SoH for cells being aged calendric by L202: $\text{SoC} = 15\%$, $T = 45\text{ }^{\circ}\text{C}$ 54

3.27a Scatter plot of the decay constant τ versus SoH for cells being aged calendric by L203: $\text{SoC} = 55\%$, $T = 0\text{ }^{\circ}\text{C}$ 54

3.27b Scatter plot of the decay constant τ versus SoH for cells being aged calendric by L204: $\text{SoC} = 55\%$, $T = 30\text{ }^{\circ}\text{C}$ 55

List of Figures

3.28a	Scatter plot of the decay constant τ versus SoH for cells being aged calendric by L205: SoC = 95 % , T = 20 °C	55
3.28b	Scatter plot of the decay constant τ versus SoH for cells being aged calendric by L206: SoC = 95 % , T = 45 °C	56
3.29a	Scatter plot of the decay constant τ versus SoH for cells being aged cyclic by L208: dSoC = 2.5 % , T = 0 °C	57
3.29b	Scatter plot of the decay constant τ versus SoH for cells being aged cyclic by L209: dSoC = 2.5 % , T = 45 °C	57
3.30a	Scatter plot of the decay constant τ versus SoH for cells being aged cyclic by L215: dSoC = 80 % , T = 0 °C	58
3.30b	Scatter plot of the decay constant τ versus SoH for cells being aged cyclic by L216: dSoC = 80 % , T = 45 °C	58
3.31a	Scatter plot of the decay constant τ versus SoH for cells being aged cyclic by L209: T = 45 °C, dSoC = 2.5 %	59
3.31b	Scatter plot of the decay constant τ versus SoH for cells being aged cyclic by L216: T = 45 °C, dSoC = 80 %	59
3.32	Smoothed IC-curves corresponding to Figure 3.15a. The figure shows the vanishing of the second local maxima from the right side which lies in a voltage range of (3.7 – 3.8)V, while the third local maxima from the right side tends to get more prominent with increased ageing. . . .	62
4.1	Geometrical mapping of data points (x_i, y_i) and corresponding (X_i, Y_i) for the Approximate Total Least Square method (Plett, 2011)	76
4.2	Lookup Table showing the OCV-SoC relationship	79
4.3	Estimation of Q_{tot} with <i>zero-current</i> sampling with $T_{zero} = 20$ min and SoC estimation via OCV-SoC lookup table. The forgetting factor was set to $\gamma = 0.985$. grey: WTLS estimate; blue: AWTLS estimate; The dashed lines illustrate the corresponding 3σ confidence intervals. . . .	81
4.4	Goodness of Model Fit for the Estimation of Q_{tot} with <i>zero-current</i> sampling with $T_{zero} = 20$ min and SoC estimation via OCV-method. The forgetting factor was set to $\gamma = 0.985$. grey: WTLS; blue: AWTLS. . . .	81
4.5	Estimation of Q_{tot} with <i>zero-current</i> sampling with $T_{zero} = 20$ min and SoC estimation via EKF. The forgetting factor was set to $\gamma = 0.985$. grey: WTLS estimate; blue: AWTLS estimate; The dashed lines illustrate the corresponding 3σ confidence intervals.	82

4.6	Goodness of Model Fit for the Estimation of Q_{tot} with <i>zero-current</i> sampling with $T_{zero} = 20$ min and SoC estimation via EKF. The forgetting factor was set to $\gamma = 0.985$. grey: WTLS; blue: AWTLS.	83
4.7	Estimation of Q_{tot} with <i>fixed-interval</i> sampling with $T_{fixed} = 3600$ s and SoC estimation via OCV-method. The forgetting factor was set to $\gamma = 0.99$. grey: WTLS estimate; blue: AWTLS estimate; The dashed lines illustrate the corresponding 3σ confidence intervals.	84
4.8	Goodness of Model Fit for the Estimation of Q_{tot} with <i>fixed-interval</i> sampling with $T_{fixed} = 3600$ s and SoC estimation via OCV-method. The forgetting factor was set to $\gamma = 0.99$. grey: WTLS; blue: AWTLS.	84
4.9	Estimation of Q_{tot} with <i>fixed-interval</i> sampling with $T_{fixed} = 3600$ s and SoC estimation via EKF-method. The forgetting factor was set to $\gamma = 0.99$. grey: WTLS estimate; blue: AWTLS estimate; The dashed lines illustrate the corresponding 3σ confidence intervals.	85
4.10	Goodness of Model Fit for the Estimation of Q_{tot} with <i>fixed-interval</i> sampling with $T_{fixed} = 3600$ s and SoC estimation via EKF-method. The forgetting factor was set to $\gamma = 0.99$. grey: WTLS; blue: AWTLS.	86
4.11	Estimation of Q_{tot} with <i>zero-current</i> sampling with $T_{zero} = 20$ min and SoC estimation via OCV-SoC lookup table. The forgetting factor was set to $\gamma = 0.985$. grey: WTLS estimate; blue: AWTLS estimate; red: Bayesian SLR estimate; The dashed lines illustrate the corresponding 3σ confidence intervals.	87

References

- Agubra, V., & Fergus, J. (2013). Lithium ion battery anode aging mechanisms. *Materials*, *6*(4), 1310–1325.
(cited on pages 1 and 11.)
- Barré, A., Deguilhem, B., Grolleau, S., Gérard, M., Suard, F., & Riu, D. (2013). A review on lithium-ion battery ageing mechanisms and estimations for automotive applications. *Journal of Power Sources*, *241*, 680–689.
(cited on pages 9, 10, 11, 12, and 95.)
- Beggi, V., Loisel, L., & Nguyen, X.-T. (2018). *Microgrid in usth campus : Architecture and power management strategies* (Doctoral dissertation). doi: 10.13140/RG.2.2.25145.42085
(cited on pages 1, 2, and 95.)
- Berecibar, M., Gandiaga, I., Villarreal, I., Omar, N., Van Mierlo, J., & Van den Bossche, P. (2016). Critical review of state of health estimation methods of li-ion batteries for real applications. *Renewable and Sustainable Energy Reviews*, *56*, 572–587.
(cited on pages 1, 4, and 26.)
- Dubarry, M., Liaw, B. Y., Chen, M.-S., Chyan, S.-S., Han, K.-C., Sie, W.-T., & Wu, S.-H. (2011). Identifying battery aging mechanisms in large format li ion cells. *Journal of Power Sources*, *196*(7), 3420–3425.
(cited on page 26.)
- Ecker, M., Gerschler, J. B., Vogel, J., Käbitz, S., Hust, F., Dechent, P., & Sauer, D. U. (2012). Development of a lifetime prediction model for lithium-ion batteries based on extended accelerated aging test data. *Journal of Power Sources*, *215*, 248–257.
(cited on page 15.)
- Eddahech, A., Briat, O., & Vinassa, J.-M. (2014). Determination of lithium-ion battery state-of-health based on constant-voltage charge phase. *Journal of Power Sources*, *258*, 218–227.
(cited on page 45.)

References

- Farmann, A., Waag, W., Marongiu, A., & Sauer, D. U. (2015). Critical review of on-board capacity estimation techniques for lithium-ion batteries in electric and hybrid electric vehicles. *Journal of Power Sources*, *281*, 114–130.
(cited on pages 9 and 16.)
- Fischer, H.-M. (2013, Dec). *Voltage classes for electric mobility* (Technology and Standardisation review). Frankfurt am Main, Germany: ZVEI - German Electrical and Electronic Manufacturers' Association, Centre of Excellence Electric Mobility.
(cited on page 9.)
- How, D. N., Hannan, M., Lipu, M. H., & Ker, P. J. (2019). State of charge estimation for lithium-ion batteries using model-based and data-driven methods: A review. *IEEE Access*, *7*, 136116–136136.
(cited on page 20.)
- Hrvanovic, D. I.-D. (2018). *Aging and state filtering for lithium-ion cells* (Unpublished master's thesis). Technische Universitaet Graz.
(cited on page 79.)
- Huang, S.-C., Tseng, K.-H., Liang, J.-W., Chang, C.-L., & Pecht, M. G. (2017). An online soc and soh estimation model for lithium-ion batteries. *Energies*, *10*(4), 512.
(cited on page 9.)
- Korthauer, R. (2013). *Handbuch lithium-ionen-batterien*. Springer.
(cited on page 1.)
- Li, Y., Abdel-Monem, M., Gopalakrishnan, R., Berecibar, M., Nanini-Maury, E., Omar, N., ... Van Mierlo, J. (2018). A quick on-line state of health estimation method for li-ion battery with incremental capacity curves processed by gaussian filter. *Journal of Power Sources*, *373*, 40–53.
(cited on pages 1, 26, 29, 31, and 89.)
- Meng, J., Ricco, M., Luo, G., Swierczynski, M., Stroe, D.-I., Stroe, A.-I., & Teodorescu, R. (2017). An overview and comparison of online implementable soc estimation methods for lithium-ion battery. *IEEE Transactions on Industry Applications*, *54*(2), 1583–1591.
(cited on pages 18, 19, and 20.)
- Nuhic, A., Terzimehic, T., Soczka-Guth, T., Buchholz, M., & Dietmayer, K. (2013). Health diagnosis and remaining useful life prognostics of lithium-ion batteries using data-driven methods. *Journal of power sources*, *239*, 680–688.

- (cited on page 15.)
- Pistoia, G., & Liaw, B. (2018). *Behaviour of lithium-ion batteries in electric vehicles: Battery health, performance, safety, and cost*. Springer.
(cited on pages 4, 10, 15, and 19.)
- Plett, G. L. (2011). Recursive approximate weighted total least squares estimation of battery cell total capacity. *Journal of Power Sources*, 196(4), 2319–2331.
(cited on pages 65, 69, and 76.)
- Plett, G. L. (2015a). *Battery management systems, volume i: Battery modeling* (Vol. 1). Artech House.
(cited on pages 7, 8, 9, and 95.)
- Plett, G. L. (2015b). *Battery management systems, volume ii: Equivalent-circuit methods* (Vol. 2). Artech House.
(cited on pages 10, 11, 12, 13, 14, 20, 79, and 95.)
- Tang, X., Zou, C., Yao, K., Chen, G., Liu, B., He, Z., & Gao, F. (2018). A fast estimation algorithm for lithium-ion battery state of health. *Journal of Power Sources*, 396, 453–458.
(cited on page 29.)
- Vetter, J., Novák, P., Wagner, M. R., Veit, C., Möller, K.-C., Besenhard, J., ... Hammouche, A. (2005). Ageing mechanisms in lithium-ion batteries. *Journal of power sources*, 147(1-2), 269–281.
(cited on pages 11, 12, 13, 14, and 95.)
- Von der Linden, W., Dose, V., & Von Toussaint, U. (2014). *Bayesian probability theory: applications in the physical sciences*. Cambridge University Press.
(cited on page 66.)
- Wang, L., Pan, C., Liu, L., Cheng, Y., & Zhao, X. (2016). On-board state of health estimation of lifepo4 battery pack through differential voltage analysis. *Applied energy*, 168, 465–472.
(cited on page 29.)
- Wang, Z., Zeng, S., Guo, J., & Qin, T. (2018). Remaining capacity estimation of lithium-ion batteries based on the constant voltage charging profile. *PloS one*, 13(7), e0200169.
(cited on page 45.)

References

- Wang, Z., Zeng, S., Guo, J., & Qin, T. (2019). State of health estimation of lithium-ion batteries based on the constant voltage charging curve. *Energy*, *167*, 661–669.
(cited on pages 45 and 97.)
- Weng, C., Cui, Y., Sun, J., & Peng, H. (2013). On-board state of health monitoring of lithium-ion batteries using incremental capacity analysis with support vector regression. *Journal of Power Sources*, *235*, 36–44.
(cited on page 26.)
- Xiong, R., Cao, J., Yu, Q., He, H., & Sun, F. (2017). Critical review on the battery state of charge estimation methods for electric vehicles. *Ieee Access*, *6*, 1832–1843.
(cited on pages 17, 18, 19, and 95.)
- Yang, J., Xia, B., Huang, W., Fu, Y., & Mi, C. (2018). Online state-of-health estimation for lithium-ion batteries using constant-voltage charging current analysis. *Applied energy*, *212*, 1589–1600.
(cited on page 45.)
- Yoshio, M., Brodd, R. J., & Kozawa, A. (2009). *Lithium-ion batteries* (Vol. 1). Springer.
(cited on page 1.)
- Zhang, J., & Lee, J. (2011). A review on prognostics and health monitoring of li-ion battery. *Journal of power sources*, *196*(15), 6007–6014.
(cited on page 16.)
- Zheng, Y., Ouyang, M., Han, X., Lu, L., & Li, J. (2018). Investigating the error sources of the online state of charge estimation methods for lithium-ion batteries in electric vehicles. *Journal of Power Sources*, *377*, 161–188.
(cited on page 20.)